Title

Characterization of Single Phase and Two Phase Heat and Momentum Transport in a Spiraling Radial Inflow Microchannel Heat Sink

Author

Ruiz, Maritza

Publication Date

2015

Characterization of Single Phase and Two Phase Heat and Momentum Transport in a Spiraling Radial Inflow Microchannel Heat Sink

by

Maritza Ruiz

A dissertation submitted in partial satisfaction of the
requirements for the degree of
Doctor of Philosophy

in

Engineering – Mechanical Engineering

and the Designated Emphasis

in

Energy Science and Technology

in the

Graduate Division

of the

University of California, Berkeley

Committee in charge:

Professor Van P. Carey, Chair
Professor Per Peterson
Adjunct Professor Samuel Mao

Spring 2015

Characterization of Single Phase and Two Phase Heat and Momentum Transport in a Spiraling Radial Inflow Microchannel Heat Sink

Abstract

Characterization of Single Phase and Two Phase Heat and Momentum Transport in a Spiraling Radial Inflow Microchannel Heat Sink

by

Maritza Ruiz

Doctor of Philosophy in Engineering – Mechanical Engineering

and the Designated Emphasis

in

Energy Science and Technology

University of California, Berkeley

Professor Van P. Carey, Chair

Thermal management of systems under high heat fluxes on the order of hundreds of W/cm^2 is important for the safety, performance and lifetime of devices, with innovative cooling technologies leading to improved performance of electronics or concentrating solar photovoltaics. A novel, spiraling radial inflow microchannel heat sink for high flux cooling applications, using a single phase or vaporizing coolant, has demonstrated enhanced heat transfer capabilities. The design of the heat sink provides an inward swirl flow between parallel, coaxial disks that form a microchannel of 1 cm radius and 300 μm channel height with a single inlet and a single outlet. The channel is heated on one side through a conducting copper surface, and is essentially adiabatic on the opposite side to simulate a heat sink scenario for electronics or concentrated photovoltaics cooling. Experimental results on the heat transfer and pressure drop characteristics in the heat sink, using single phase water as a working fluid, revealed heat transfer enhancements due to flow acceleration and induced secondary flows when compared to unidirectional laminar fully developed flow between parallel plates. Additionally, thermal gradients on the surface are small relative to the bulk fluid temperature gain, a beneficial feature for high heat flux cooling applications. Heat flux levels of 113 W/cm^2 at a surface temperature of 77°C were reached with a ratio of pumping power to heat rate of 0.03%. Analytical models on single phase flow are used to explore the parametric trends of the flow rate and passage geometry on the streamlines and pressure drop through the device.

Flow boiling heat transfer and pressure drop characteristics were obtained for this heat sink using water at near atmospheric pressure as the working fluid for inlet subcooling levels ranging from 20 to 80°C and mean mass flux levels ranging from 184-716 kg/m^{2}s. Flow

enhancements similar to single phase flow were expected, as well as enhancements due to increased buoyant forces on vapor bubbles resulting from centripetal acceleration in the flow which will tend to draw the vapor towards the outlet. This can also aid in the reduction of vapor obstruction of the flow. The flow was identified as transitioning through three regimes as the heat rate was increased: partial subcooled flow boiling, oscillating boiling and fully developed flow boiling. During partial subcooled flow boiling, both forced convective and nucleate boiling effects are important. During oscillating boiling, the system fluctuated between partial subcooled flow boiling and fully developed nucleate boiling. Temperature and pressure oscillations were significant in this regime and are likely due to bubble constriction of flow in the microchannel. This regime of boiling is generally undesirable due to the large oscillations in temperatures and pressure and design constraints should be established to avoid large oscillations from occurring. During fully developed flow boiling, water vapor rapidly leaves the surface and the flow does not sustain large oscillations. Reducing inlet subcooling levels was found to reduce the magnitude of oscillations in the oscillating boiling regime. Additionally, reduced inlet subcooling levels reduced the average surface temperature at the highest heat flux levels tested when heat transfer was dominated by nucleate boiling, yet increased the average surface temperatures at low heat flux levels when heat transfer was dominated by forced convection. Experiments demonstrated heat fluxes up to 301 W/cm^2 at an average surface temperature of 134°C under partial subcooled flow boiling conditions. At this peak heat flux, the system required a pumping power to heat rate ratio of 0.01%. This heat flux is 2.4 times the typical values for critical heat flux in pool boiling under similar conditions.

Contents

List of Figures

List of Tables

Acknowledgments

I'd like to thank Professor Van P. Carey for his support as an advisor, mentor and teacher throughout my time at UC Berkeley. I'd also like to thank my dissertation committee, Professor Per Peterson and Dr. Samuel Mao, for their feedback and support. Thanks to the staff of the machine shop: Gordon, Jesse, Dennis and Mick for their indispensable advice and skill in completing the design and fabrication of my experiments. Thanks to the mechanical engineering staff: Donna Craig, Shareena Samson, and Yawo Akpawu for their support and knowledge on navigating grad school. A great big thanks to all my friends at Berkeley that have made my time in graduate school that much more awesome! Thanks to all of my family for supporting my goals throughout my entire education and thanks to my three lovely sisters for being role models for my success. Thanks to the ladies of GWE for encouraging and supporting all female engineers, for the painting parties, gym encouragement and much much more. I should probably also thank the staff at Brewed Awakening for providing me with a constant source of cappuccinos, and maybe even Kip's, Pappy's, and Raleigh's (RIP) for providing me escapes on Friday nights with all my favorite mechanical and geotechnical engineers, especially my most favorite, Sam Nolan. But most importantly, I'd like to thank all the past and current members of the EITlab who have provided me with and continue to provide mentorship, research assistance, knowledge, friendship, endless discussions, book clubs and headaches. Finishing my dissertation wouldn't have been possible with out your advice and support. Special thanks to the greatest labmates: Sara Beaini, Jorge Padilla, Kenneth Armijo, Hector Mendoza, Ruth Herrera,Vince Romanin, and Dave Lettieri .

Financial support for this research was made possible through UC Berkeley Chancellors Fellowship, National Science Foundation Graduate Research Fellowship, Alfred P. Sloan Foundation, and UC Center for Information Technology Research in the Interest of Society and is gratefully acknowledged.

Chapter 1

Introduction

The focus of my dissertation was to explore the frontiers of high heat flux cooling systems through the development and characterization of an innovative “spiraling radial inflow” heat sink design. Using techniques in both single phase and flow boiling heat transfer, my goal was to provide new approaches to solving fundamental issues in thermal management of compact, high-flux cooling systems. Though motivated by present-day issues in the computer and energy industries, I hope the thorough analysis and design of the heat sink can lead to further innovations in the future of thermal engineering.

1.1 Motivation

Thermal management of systems under high heat fluxes is important for the safety, performance and lifetime of devices. A large range of engineering systems are subject to ever-increasing heat fluxes on the order of 100 to 1000 of W/cm^2 and require innovative technologies for improved cooling capability. Two notable applications which require high heat dissipation cooling include:

a) the integration of cooling on high powered electronic chips or processors

b) the cooling of concentrated solar photovoltaic systems to allow for increased cell operating efficiencies

Beyond these two applications, critical reviews on high heat flux cooling technologies list a variety of other applications for these technologies, such as: gas turbine blade cooling, laser diode cooling, microchemical reactors, biotechnologies, air conditioning, refrigeration, hybrid vehicle power electronics, hydrogen storage, rocket engines, avionics, defense electronics, thermal control in microgravity, and modern nuclear fusion and fission reactors [1]–[4].

Electronics Cooling

Current electronics innovation is limited in part by the need to provide effective cooling. Agostini et al. [2] listed a cooling benchmark for modern microelectronics and power electronics of heat fluxes beyond 300 W/cm^2 at chip temperatures of 85°C. The development of new solutions in cooling tech will be required if higher power density is to be pursued. The design objectives for an electronic heat sink or "cold plate design" are, thus, to:

- Achieve high heat dissipation rates at high conductance levels
- Maintain uniform and controlled wall temperatures
- Minimize the pumping power of the system
- Use a simple to manufacture, reliable, and robust design

The potential for integrating cooling systems into a 3D chip architecture also provides an attractive solution to meet processor cooling needs and is an active area of research [5], [6]

Concentrated Photovoltaics

Finding solutions for cost-effective renewable energy technologies is a pressing issue in our society, due to the need to reduce dependency on greenhouse gas emitting fossil fuel technology. Concentrated photovoltaic (CPV) systems are an attractive area of renewable energy research for their potential to reduce the cost of solar energy in regions with high incident solar flux. CPV systems work by using a concentrator system to focus solar flux onto a small photovoltaic cell. Concentration on the order of 10's to 1000's of suns allows for the use of reduced cell size, which is replaced by lower cost lenses or reflectors. These concentration systems typically consist of parabolic mirrors, or Fresnel lenses on a single or dual axis tracking system that follows incident sunlight throughout the day. The use of smaller cell area also allows for more expensive multijunction cells with high efficiencies, up to 44.7% using 4-junction cells [7]. A 2012 NREL technical report lists high concentration photovoltaics, defined as systems using concentration levels beyond 400×, as being poised for a growth of hundreds of MW per year [8].

A cross-sectional view of an idealized cell is shown in Fig. 1.1. This shows the excess energy incident on the photovoltaic cell that is not converted to electricity is absorbed in the cell as thermal energy. The top cover glass is attached with an adhesive to the top of the cell, which is used to protect the solar cell while providing minimal reflection. The solder attaches the substrate to the cell. The substrate and solder are, ideally, designed to have high thermal conductivities that can provide reduced thermal resistance to the cooling mechanism. The bottom layer of the substrate is typically connected to a cooling device. Thermal management through the cooling device is important because high temperatures, large temperature gradients, and large amounts of thermal cycling all can have negative effects on the system. Cell efficiencies decrease with increased temperature at a rate of about 0.5%/°C for silicon cells and around 0.06%/°C for multijunction cells [9]. All of these factors also tend to reduce the life expectancy of the system resulting from connection or cell failures. The necessary heat dissipation rates for a cell subject to 1000 W/m^2 solar flux for a range of concentration factors (CF) and cell efficiency values are shown in Figure 1.2. This figure shows that heat dissipation rates can easily reach 100 W/cm^2.

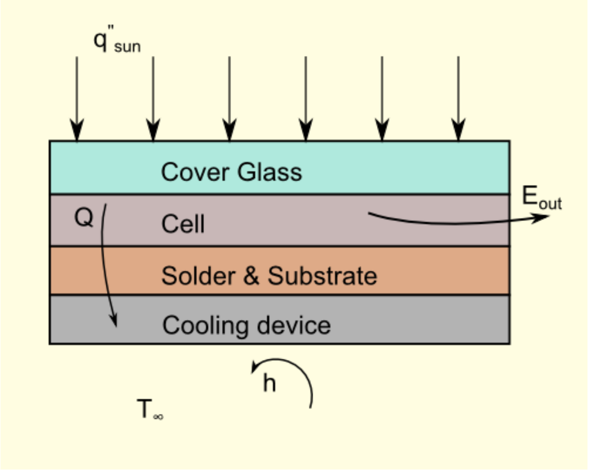

Figure 1.1: Schematic of the components of a CPV cell showing relevant flow of energy

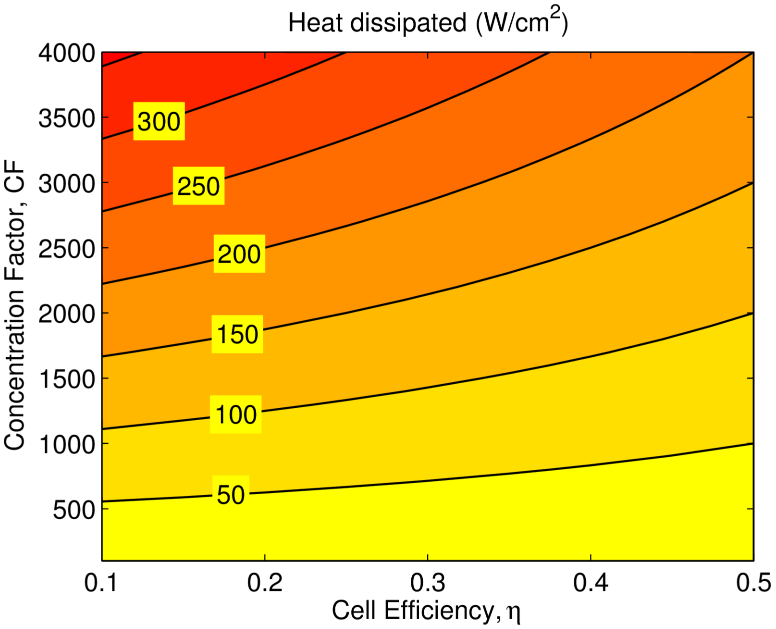

Figure 1.2: Cooling requirements for CPV system based on concentration factor and cell efficiency

Innovation in the realm of cooling designs for concentrated photovoltaics can lead to increased cell efficiencies and net power output of the entire CPV system. Royne et al. [10] reviewed methods for cooling CPV cells and concluded densely packed cells with concentrations over 150 suns required active cooling technologies. They also established design critieria for cooling of concentrated photovoltaics which include very similar design objectives for electronics cooling listed above, with the addition of having the potential to use waste thermal energy. A wide range of active research in waste heat usage for combined solar photovoltaic/thermal (PV/T) technology is discussed in Tyagi et al. [11] including desalination, heating and cooling.

1.2 Overview of Current Technologies and Innovations

Compact, high heat flux cooling technologies use flow in small channels or designs that leverage the latent heat of a working fluid to achieve high heat dissipation rates at low surface temperatures. State-of-the-art systems are reviewed in Agostini et al. and Ebadian and Lin [2], [3]. They include: single- and two-phase flow in microchannels, single- and two-phase flow in porous media, jet impingement, sprays and heat pipes. An overview of each of these technologies is discussed below, with an emphasis on microchannel cooling. Additionally, technologies that use radial or curved channel flows is discussed, as these systems pertain to the motivation for the design of a novel heat sink discussed in Chapter 2.

Microchannels

Microchannnels provide enhanced heat transfer due to the increased heat transfer coefficients in small channels. Their ability to provide high heat flux cooling at a compact scale makes them an attractive technology for integration with electronics or CPV cooling. The main driver of research in this field is to achieve high thermal performance at low pumping costs.

Single Phase Microchannels

The use of small channels for their ability to provide high heat transfer coefficients has been studied for use with electronics since a 1981 study by Tuckerman and Pease [12]. This system dissipated a heat flux of 790 W/cm^2 using a water cooled system with a hydraulic diameter, $d_h = 86\mu$m. A large spectrum of single phase microchannels have been developed since the creation of this system. Agostini et al. and Ndao et al. [2], [13] both provide reviews of current single phase technologies for high heat flux applications which reveal microstructured devices with pin fin or offset strip fin channels having hydraulic diameters of 50-1000 μm as promising technologies. Kandlikar and Bapat [14] also provide a review of methods for current single phase liquid cooled designs. Their study indicated that single-phase rectangular or finned microchannels are the most viable current option when compared to jet impingement and spray cooling because of the large pressure penalties associated with the two latter options. Still, the main disadvantages with single phase microchannel systems are high pumping power required to achieve high heat flux levels and the potential for thermal gradients across the device as the working fluid heats up. In 2005, Kandlikar [4] discussed the need for new microchannel configurations to provide high performance at low pressure penalties, and in 2013, Kandlikar et al. [5] reiterated the need for single phase flow designs which can achieve high heat transfer coefficients with low pressure drops, and also emphasized the issue of having a small available area for manifolding. In 2014, Wu and Sunden [15] reviewed recent enhancements in single phase microchannels with an emphasis on new and promising techniques for enhancement. Interrupted microfins, which are typical in macroscale channels but optimized for small channels, showed promise. Additionally, engineered fluids with additives such as nanofluids or micro/nano-encapsulated phase change materials can allow for enhanced heat transfer coefficients as well as more uniform fluid and surface temperatures.

Two Phase Microchannels

Two phase microchannels exploit the large latent heat of a working fluid during boiling to achieve high heat dissipation rates. These systems have the ability to achieve desired cooling rates at lower pumping costs and more uniform surface temperatures when compared to single phase microchannels. Major drawbacks to boiling in microchannels, however, include compressibility, flashing, choking, instabilities and oscillations in the flow that may lead to early onset of CHF and unpredictability of flow properties [16]. Additionally, despite the enhanced heat transfer performance, surface temperatures are dependent on the saturation temperature of the working fluid. Fluids which have been studied for electronics and CPV cooling include water, ammonia, refrigerants and dielectric liquids [1], [17], [18]. Two phase flow in microchannels have been studied as early as the late 1970's for use in liquid cooled turbine blades [19], and a much larger range of applications of two phase microchannels have recently been reviewed by Mudawar [1]. Research on two phase microchannel heat sinks is a very active area of research, with a large number of recent reviews and analyses being published since 2010 [1], [3], [5], [15], [16], [20]–[23].

In 2005, Kandlikar [4] expressed the need for more research on the fundamentals of boiling in microchannels as well as on effective techniques in the stabilization of boiling flow, and discussed current methods of enhancement including the use of artificial nucleation sites and entrance pressure drop elements to mitigate instabilities. In 2014, Wu and Sunden [15] reiterated the need for more information on bubble dynamics in microchannels as well as the need for research on fouling and durability tests for surface enhancements. They also discussed currently researched enhancements in two phase microchannels to mitigate flow instability and increase both heat transfer coefficients and critical heat flux levels. Inlet restriction, vapor venting, tapered manifolds and expanding channels are all design considerations that can help prevent flow instabilities. Additionally, surface modifications such as re-entrant cavities, porous surfaces and micro/nanoscale surface coatings can effect flow patterns based on the changes in surface wettability and development of nucleation sites. Increased wettability may lead to increased critical heat flux levels but may also result in delay of onset of nucleate boiling. Tibirca and Ribatski [21], Kandlikar [22], and Ebadian and Lin [3] all discuss the need for studies of wettability effects on boiling heat transfer, two phase flow patterns and dryout. In a 2011 overview of two phase microchannel heat sinks, Mudawar [1] discusses recent attempts on enhancement in two phase microchannels using nanofluids, carbon nanotube coated surfaces and jet-impingement hybrid devices. It was recommended that using nanofluids as a working fluid be avoided in two phase flow because of clustering that can lead to blockage in the channel. The carbon nanotube coated surfaces had morphology issues at high velocities. Hybrid devices for jet impingement proved promising with heat fluxes exceeding 1000 W/cm^2 using HFE-7100 as a working fluid. In 2014, Kim and Mudawar [16] provided a systematic assessment of predictive methods and proposed a universal correlation for evaluating the boiling heat transfer properties in circular and rectangular microchannels. This correlation was valid for both nucleate and convective boiling dominated regimes with a mean absolute error of about 20%. This method used only important nondimensional flow parameters, but wettability effects were not considered. Kandlikar et al. [5] suggest future work to realize the benefits of microchannel boiling include similar goals as discussed above: enhancing fundamentals, providing accurate mapping of flow regimes, using nanoscale surface features for heat transfer enhancement, and developing robust, inexpensive suppression techniques for mitigating flow boiling instabilities. Ebadian and Lin [3] also stress the need for increasing reliability and reducing cost by using innovative designs and optimizing geometries.

Other High Flux Cooling Technologies

Jet Impingement and Sprays

Jet impingement technology provides high velocity fluid impinging on the surface which can then form a thin film and evaporate. Similarly, spray cooling provides a fine spread of droplets onto a surface which then evaporate off the surface. Yeom and Shannon [24] discuss an overview of these technologies which are used in applications with ultra-high heat fluxes up to 10000 W/cm^2 such as quenching and laser cooling. They are some of the most effective technologies for high heat flux cooling, but typically require very high pumping penalties. Compact jet impingement technologies can provide up to 400 W/cm^2 at about 30-40°C wall superheat. However, these systems can be damaging to sensitive surfaces and provide nonuniform heat transfer coefficients over the surface. Spray cooling may provide less abrasive and more uniform cooling, but is also subject to high pressure drops and repeatability issues. One innovative solution is to produce vibrating device which atomize droplets of water and can achieve heat rates of 420 W/cm^2 at reduced pumping cost [25].

Passive Cooling Technologies

Passive cooling technologies require no external pumping mechanisms and use heat spreading and natural convection to cool. Typically these systems have larger thermal resistances when compared to active cooling mechanisms. Two types of passive cooling devices often used for electronics or CPV cooling include finned heat sinks and heat pipes. Finned surfaces use increased surface area subject to natural convection from the environment to cool the cell. They also act as heat spreaders which conduct heat away from the surface laterally towards the fins. Compact finned surfaces are typically used for single cell CPV applications and low power processor cooling.

Heat pipes work as a heat spreader by vaporizing a fluid at the heated site, and condensing the fluid using natural convection at a cooler site, usually attached to a finned surface. The fluid then returns to the heated surface through capillary action using a wick structure. The use of heat pipes for CPV cooling has been experimentally studied by [26]–[28]. Micro heat pipes and loop heat pipes show potential for electronics cooling and CPV with the ability to passively cool over 100 W/cm^2 [24], [29], [30]. Recent studies have suggested using nanofluids in heat pipes to increase the effective thermal conductivity of the system. Sureshkumara et al. [31] reviewed the use of a variety of nanofluids studied including Cu, CuO, Al_2O_3, ZnO, TiO_2, SiO_2, gold, and silver nanoparticles.

Radial Flow Devices

Radial flow geometries have been studied for a variety of situations. In 1955, McGinn [32] conducted studies on radial flows and found secondary flows in only diverging outflows but not converging inflows. Boyd and Rice [33] provided a numerical solution to laminar radial inflow in rotating disks, and Singh et al. [34] suggested turbulent to laminar transitions in purely radial inflows due to acceleration of the flow. Petitot et al. [35] experimentally showed the presence of secondary flows in a laminar vortex inflow. Most research on heat exchangers in radial systems has involved radial outflow between concentric disks or within rotating disks. Mochizuki and Yang and Mochizuki et al. [36], [37] studied the flow regimes of radial outflow and heat transfer in one and multiple disk assemblies. They found heat transfer characteristics varied over regimes identified as steady laminar, periodic laminar, and turbulent. Suryanarayana et al. [38] performed experiments in purely radial turbulent outflow as well as outflow in co-rotating disks and established correlations for the average Nusselt numbers. The effect of rotation on the heat transfer performance was unclear with slightly decreased heat transfer performance for the highest rotation rate tested. More recently, Roy et al. and Gherasim et al. [39]–[41] have studied enhancements to heat transfer using nanofluids in laminar radial outflows. Heat transfer properties of radial inflows have been studied by Djaoui et al. [42] in a turbulent rotor-stator system. Djaoui found that inflow strongly effects the flow behavior near the axis. Devienne et al. [43] performed experiments on spiral radial inflow in a cylindrical cavity and discussed the heat transfer in channels from 10-25 mm with Newtonian and non-Newtonian fluids in both laminar and turbulent regimes. Their results showed the dependence of the Nusselt number on the heat rate in laminar flows.

Fluidic Diodes

Fluidic diodes are devices which act as reliable, one way check valves without the use of moving parts and, thus, not requiring maintenance. The pressure drop in these devices is much higher in the "reverse" direction than in the "forward direction", so the flow is not completely shut off in the reverse direction. A review of these typed of devices are discussed in Forsberg et al. [44], including vortex diodes, scroll diodes, and flow-rectifier diodes. These devices are designed for use in light water reactors to passively reduce leakage and prevent drainage during accident scenarios. Vortex diodes achieve the diode effect with a swirling radial inflow as the high pressure direction and radial outflow as the low pressure direction. The main figure of merit for fluidic diodes is the Diodicity, the ratio of reverse to forward pressure drop. For vortex diodes the value is typically around 50 [44]. Kulkarni et al. have experimentally studied a vortex diode [45], providing a design guide for these types of diodes. They also computationally modeled the same system [46]. They show diodicity increases with Reynolds number, leveling off past a critical value. CFD models also indicate there is induced relaminarization of the flow towards the center of the vortex. Motamed-Amini and Owen [47], found that wet steam in vortex diodes could reduce the performance because of water buildup destroying the vortex in the flow. They also observed reduced performance with increased compressibility as well as due to oscillations induced by wet steam. Priestman [48], [49] has experimentally studied and developed a viscid flow model for vortex throttles with this geometry. Anduze et al. [50] have also developed and tested a microscale vortex diode for microfluidics applications. More recently, Yoder et al. [51] have proposed vortex diodes for use with Fluoride salts for high temperature reactors.

Boiling Heat Transfer in Curved Channels

Flow boiling with streamwise curvature subject to concave heating has been shown to have enhanced critical heat flux when compared to straight channels[52]–[55]. A study by Sturgis and Mudawar [55] has shown that enhancement is due to increased buoyant forces on vapor due to centripetal acceleration of the flow which causes increased amount of vapor to be drawn from the heated surface and transported into the bulk flow. Increased subcooling at the heated surface due to radial pressure gradients also tended to prevent dryout, enhancing critical heat flux. This effect is more significant for low subcooling levels where vapor levels are higher, this enhancement was calculated as up to 50% in flow using FC-72 and subcooling of 5°C in Leland and Chow [52].

Chapter 2

Device Design

Motivated by the need to solve high flux cooling issues discussed in chapter 1, a novel, spiraling radial inflow microchannel heat sink was developed. This system was designed to study the enhancements possible in both single phase flow and two phase flow boiling. For single phase flow, the microchannel design was hypothesized to aid in providing uniform surface temperatures while achieving a high heat dissipation rate and preventing the maldistribution of flow which can be an issue in rectangular microchannel arrays. For two phase flow, enhancements to boiling similar to those seen in curved channels with concave heating were expected. This motivated the design of a radial inflow heat sink for two phase flow that can exploit the buoyant force on vapor bubbles due to centripetal acceleration, helping to draw vapor off the surface towards the outlet and preventing dryout.

2.1 Detailed Description of Device

The heat sink consists of a spiraling inflow of fluid sweeping the surface of two coaxial disks with a constant gap height and exiting through a port in the center. A diagram of the device is shown in Fig. 2.1, with the streamlines of the expected single phase flow shown in Fig. 2.2. A single entrance port on the edge of the device leads into a larger “feeder” channel region to allow for the development of a more axisymmetric flow distribution in the microchannel region. The tangential flow helps to provide a uniform flow distribution over the entire heated surface which aids in temperature uniformity and prevents the development of hot spots. The simple design with a single inlet and outlet allows for ease in manufacturing since it does not involve microstructured surfaces or complex manifolding. The use of microchannels on the order of 100 μm allows for high heat transfer coefficients and a compact footprint. Figure 2.1 also shows a proposed alternative tapered passage design for single phase flow in which the gap height between the walls of the channel is decreased radially along the flow path. This provides an increased heat transfer coefficient towards the center of the device as the fluid is heated, allowing for a more uniform temperature distribution. This is based upon the assumption that the passage would have a near constant Nusselt number, and the heat transfer coefficient would thus scale inversely with $b(r)$, the gap size at a radial location, r. This study entails both an analytical description of this type of heat sink and experimental characterization of single phase and two phase boiling flow in a fabricated device with a constant gap height of 300 μm subject to high heat dissipation rates up to 300 W/cm^2.

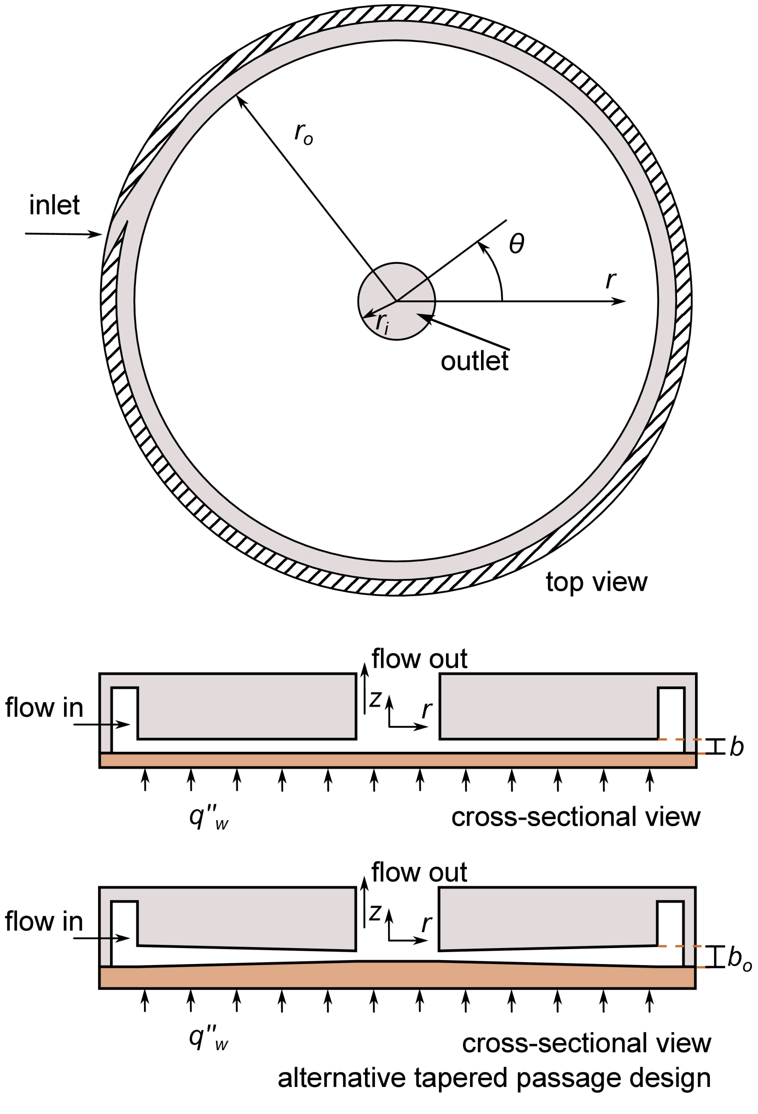

Figure 2.1: Schematic of the heat sink including both the tapered channel and constant channel height designs

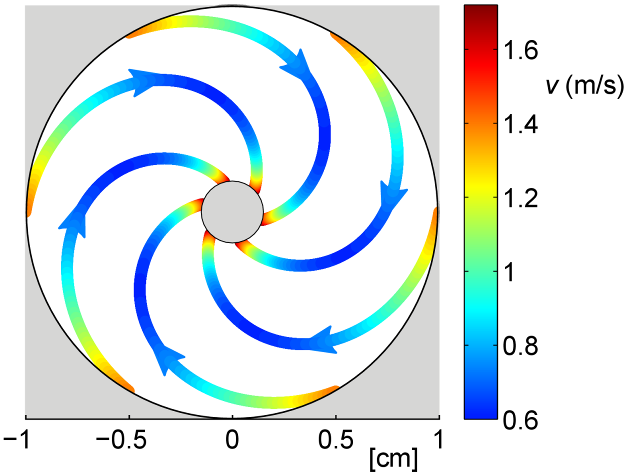

Figure 2.2: Streamlines of theoretical model of single phase flow in the heat sink on a device with dimensions given in Table 4.1, liquid water as a working fluid, and $\mathrm{Re}_o = 830$

Chapter 3

Theory on Heat and Momentum Transport in the Microchannel

3.1 Single Phase Formulations

An analytic solution for the single phase velocity, pressure and temperature distributions in the microchannel are found using integral method solutions to the momentum and energy equations. An abridged derivation is shown in the subsequent sections and a full derivation is shown in Appendix B. These solutions can be used to explore the parametric trends of relevant design parameters, such as flow rate and passage geometry, on the single phase streamlines, pressure drop and temperature distributions through the device.

Pressure and Velocity Distributions

In order to solve for the velocity and pressure distributions in the r, θ,and z directions, the following idealizations are made in solving the continuity and momentum equations:

- The flow is steady and incompressible.
- The flow is laminar. The use of microchannels results in small Reynolds numbers.
- The flow is axisymmetric, therefore, all θ derivatives of flow quantities are zero.
- The flow is fully developed, no entrance or exit effects are considered.
- The outer radius, r_o, is much larger than the initial gap size, b_o, so that $b_o/r_o << 1$
- The gap height b has a linear profile, $b(r)$, or a constant height
- Constant fluid properties are assumed

The following parabolic solutions are postulated for the radial and tangential velocities for a gap of varying size, $b(r)$, as used in [56],

$$v_r = \bar{v}_r(r)\phi(z,b) \tag{3.1}$$

$$v_\theta = \bar{v}_\theta(r)\phi(z,b) \tag{3.2}$$

where

$$\phi(z,b) = \frac{3}{2}\left[1 - \left(\frac{2z}{b}\right)^2\right] \tag{3.3}$$

and $\bar{v}_r$ and $\bar{v}_\theta$ are mean velocities defined as

$$\bar{v}_r(r) = \frac{1}{b}\int_{-b/2}^{b/2} v_r dz \tag{3.4}$$

$$\bar{v}_\theta(r) = \frac{1}{b}\int_{-b/2}^{b/2} v_\theta dz \tag{3.5}$$

Since $b(r)$ is linear, it can be written as

$$b(r) = \frac{b_o - b_i}{r_o - r_i}(r - r_o) + b_o \tag{3.6}$$

The following nondimensional variables are used below to solve for the dimensionless velocities:

$$R = r/r_o \tag{3.7}$$

$$Z = z/b_o \tag{3.8}$$

$$\beta = b/b_o \tag{3.9}$$

$$\varepsilon = b_o/r_o \tag{3.10}$$

Defining the gap slope $\alpha = (1-\beta_i)/(1-R_i)$, β can be written as

$$\beta = \alpha R - \alpha + 1 \tag{3.11}$$

Radial velocity solution

Knowing the mass flux is constant through any cross-section for radius, r

$$\dot{m} = 2\pi r b \bar{v}_r \rho = \text{constant} \tag{3.12}$$

$\bar{v}_r$ can be found with respect to $\bar{v}_{ro} = \bar{v}_r(r = r_o)$. Note the velocity is negative since the flow is inward. $\bar{v}_r$ can be written as

$$\bar{v}_r = \frac{\bar{v}_{ro} r_o b_o}{rb} \tag{3.13}$$

Nondimensionalizing with respect to $-\bar{v}_{ro}$ gives

$$\bar{V}_r(R) = \frac{\bar{v}_r}{-\bar{v}_{ro}} = -\frac{1}{\beta R} \tag{3.14}$$

$$V_r(Z,R) = \frac{v_r}{-\bar{v}_{ro}} = -\frac{\phi}{\beta R} \tag{3.15}$$

If the gap size is constant, $\beta = 1$, and the solution becomes

$$\bar{V}_r(R) = -\frac{1}{R} \tag{3.16}$$

$$V_r(Z,R) = -\frac{\phi}{R} \tag{3.17}$$

Axial velocity solution

The solution to the z-direction velocity, v_z, can be found by solving the continuity equation written in cylindrical coordinates, and using the idealizations from above

$$\frac{1}{r}\frac{\partial r v_r}{\partial r} + \frac{\partial v_z}{\partial z} = 0 \tag{3.18}$$

Using

$$V_z = \frac{v_z}{-\bar{v}_{ro}} \tag{3.19}$$

Eq. (3.18) can be nondimensionalized as

$$\frac{1}{R}\frac{\partial (R V_r)}{\partial R} + \frac{1}{\varepsilon}\frac{\partial V_z}{\partial Z} = 0 \tag{3.20}$$

Integrating to solve for V_z and using the boundary condition of symmetry, $V_z(Z=0) = 0$, gives

$$V_z(Z,R) = -\frac{\alpha \varepsilon Z \phi}{\beta^2 R} \tag{3.21}$$

or in terms of V_r

$$V_z(Z,R) = \frac{\alpha \varepsilon Z V_r}{\beta} \tag{3.22}$$

Note ε is $<< 1$, whereas the other nondimensional parameters are typically of order 1, so this relation shows V_z is much smaller than V_r. If the gap size is constant, the continuity equation has a trivial solution where $V_z = 0$.

θ-dir velocity solution

Using the idealizations above the θ-direction momentum balance can be written as

$$\begin{aligned} v_r \frac{\partial v_\theta}{\partial r} + v_z \frac{\partial v_\theta}{\partial z} + \frac{v_r v_\theta}{r} \\ = \nu \left[\frac{1}{r} \frac{\partial}{\partial r} \left(r \frac{\partial v_\theta}{\partial r} \right) + \frac{\partial^2 v_\theta}{\partial z^2} - \frac{v_\theta}{r^2} \right] \end{aligned} \tag{3.23}$$

Defining

$$V_\theta = \frac{v_\theta}{\bar{v}_{\theta,o}} \tag{3.24}$$

$$W = \frac{\bar{v}_{\theta,o}}{-\bar{v}_{ro}} \tag{3.25}$$

$$\mathrm{Re_{r,o}} = \frac{-\bar{v}_{ro} 2 b_o}{\nu} \tag{3.26}$$

$$\mathrm{Re_m} = \mathrm{Re_{r,o}} \varepsilon \tag{3.27}$$

where $\bar{v}_{\theta,o} = \bar{v}_\theta(r = r_o)$, and because of the symmetry of the device only values in the positive tangential direction need to be considered. Nondimensionalizing Eq. (3.23) and substituting for V_z gives

$$\begin{aligned} V_r \frac{\partial V_\theta}{\partial R} + \frac{\alpha Z}{\beta} V_r \frac{\partial V_\theta}{\partial Z} + \frac{V_r V_\theta}{R} \\ = \frac{2\varepsilon}{\mathrm{Re_{r,o}}} \left[\frac{1}{R} \frac{\partial}{\partial R} \left(R \frac{\partial V_\theta}{\partial R} \right) + \frac{1}{\varepsilon^2} \frac{\partial^2 V_\theta}{\partial Z^2} - \frac{V_\theta}{R^2} \right] \end{aligned} \tag{3.28}$$

For the current design, $\mathrm{Re_{r,o}}$ will likely be on the order of (10-100), and ε will likely fall into the range of (0.01 - 0.1). Thus, the second term on the right hand side of Eq. (3.28) is of order $1/(\varepsilon \mathrm{Re_{r,o}}) = O(1/10 - 10)$, and the first and third terms on the right hand side of Eq. (3.28) are of order $\varepsilon/\mathrm{Re_{r,o}} = O(10^{-4} - 0.1)$. The terms on the left hand side of Eq. (3.28) are all of $O(\alpha)$ or $O(1)$. Thus, keeping all terms on the left hand side, the first and third terms of the right hand side can be neglected and the second term must be kept. This results in

$$V_r \frac{\partial V_\theta}{\partial R} + \frac{\alpha Z}{\beta} V_r \frac{\partial V_\theta}{\partial Z} + \frac{V_r V_\theta}{R} = \frac{2}{\mathrm{Re_m}} \frac{\partial^2 V_\theta}{\partial Z^2} \tag{3.29}$$

Integrating both sides from $-\beta/2$ to $\beta/2$ over dZ and dividing by β gives

$$\frac{6}{5} \left(\bar{V}_r \frac{\partial \bar{V}_\theta}{\partial R} + \frac{\bar{V}_r \bar{V}_\theta}{R} \right) = -\frac{24 \bar{V}_\theta}{\mathrm{Re_m} \beta^2} \tag{3.30}$$

Integrating over R to solve for $\bar{V}_\theta$ and using the boundary condition that $\bar{V}_\theta(R = 1) = 1$ yields

$$\bar{V}_\theta(R) = \frac{1}{R} \exp\left[\frac{20(R-1)}{\mathrm{Re_m} \alpha} \right] \beta^{\frac{20(\alpha-1)}{\mathrm{Re_m} \alpha^2}} \tag{3.31}$$

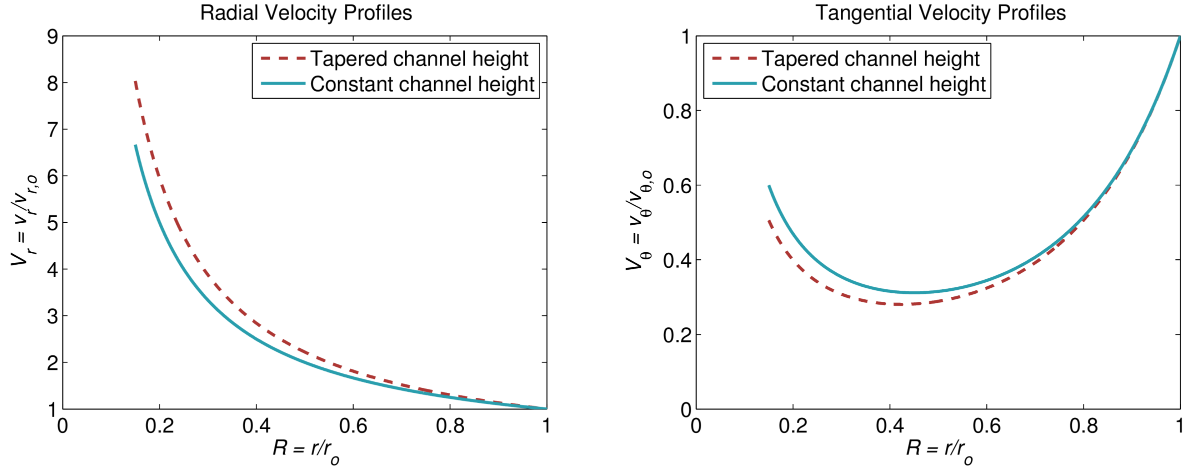

(a) (b)

Figure 3.1: Velocity profiles for the flow for both a constant and tapered channel height, using Re$_m$= 4, α=1/5, and R_i=0.15.

If the gap size is constant, $\beta = 1$, and the solution to Eq. (3.30) becomes

$$\bar{V}_\theta(R) = \frac{1}{R}\exp\left[\frac{10(R^2-1)}{\mathrm{Re_m}}\right] \tag{3.32}$$

Nondimensional velocity distributions for both the constant and variable gap sizes are shown in Fig. 3.1 and using values for an expected experimental system. Figure 3.1a shows the radial velocity increasing inversely proportional to the radius and Fig. 3.1b shows the competing effects of friction decreasing the tangential velocity and conservation of angular momentum acting to increase the velocity. The relative value of v_r to v_θ is based on W the ratio of the velocities at the inlet which can be designed to provide more uniform coverage of the surface depending on the inlet mechanism in the device.

Pressure distribution

Using the idealizations above the r-direction momentum balance can be written as

$$\begin{aligned} v_r\frac{\partial v_r}{\partial r} + v_z\frac{\partial v_r}{\partial z} - \frac{v_\theta^2}{r} \\ = -\frac{1}{\rho}\left(\frac{\partial P}{\partial r}\right) + \nu\left[\frac{1}{r}\frac{\partial}{\partial r}\left(r\frac{\partial v_r}{\partial r}\right) + \frac{\partial^2 v_r}{\partial z^2} - \frac{v_r}{r^2}\right]\end{aligned} \tag{3.33}$$

Nondimensionalizing P using the initial tangential velocity which is the largest initial velocity assuming $W > 1$,

$$P^* = \frac{P}{\rho v_{\theta,o}^2} \tag{3.34}$$

gives

$$\begin{aligned}\frac{V_r}{W^2}\frac{\partial V_r}{\partial R}+\frac{V_z}{\varepsilon W^2}\frac{\partial V_r}{\partial Z}-\frac{V_\theta^2}{R}&=-\frac{\partial P^*}{\partial R}\\&+\frac{2\varepsilon}{W^2\mathrm{Re}_{\mathrm{r,o}}}\left[\frac{1}{R}\frac{\partial}{\partial R}\left(R\frac{\partial V_r}{\partial R}\right)+\frac{1}{\varepsilon^2}\frac{\partial^2 V_r}{\partial Z^2}-\frac{V_r}{R^2}\right]\end{aligned}\tag{3.35}$$

Using similar arguments from the previous section on the orders of Re and ε, the second and fourth terms of the right hand side above can be neglected whereas the first third term must be kept. This results in

$$\frac{V_r}{W^2}\frac{\partial V_r}{\partial R}+\frac{\alpha Z V_r}{\beta W^2}\frac{\partial V_r}{\partial Z}-\frac{V_\theta^2}{R}=-\frac{\partial P^*}{\partial R}+\frac{2}{W^2\mathrm{Re}_{\mathrm{m}}}\frac{\partial^2 V_r}{\partial Z^2}\tag{3.36}$$

Integrating both sides from $-\beta/2$ to $\beta/2$ over dZ and dividing by β yields:

$$\frac{6}{5}\left(\frac{\bar{V}_r}{W^2}\frac{\partial \bar{V}_r}{\partial R}-\frac{\bar{V}_\theta^2}{R}\right)=-\frac{1}{\beta}\int_{-\beta/2}^{\beta/2}\frac{\partial P^*}{\partial R}dZ-\frac{24\bar{V}_r}{W^2\mathrm{Re}_{\mathrm{m}}\beta^2}\tag{3.37}$$

Defining an average dimensionless pressure over the surface

$$\bar{P}^*=\frac{1}{\beta}\int_{-\beta/2}^{\beta/2}P^* dZ\tag{3.38}$$

Using the Leibniz rule and symmetry the first term on the right hand side of Eq. (3.37) becomes

$$-\frac{1}{\beta}\int_{-\beta/2}^{\beta/2}\frac{\partial P^*}{\partial R}dZ=-\frac{1}{\beta}\left[\frac{\partial}{\partial R}(\bar{P}^*\beta)-\alpha P^*(\frac{\beta}{2},R)\right]\tag{3.39}$$

Noting that pressure does not vary much with z location in the heat sink, $\partial P^*/\partial Z\sim \mathrm{O}[\varepsilon]$. Then, the Taylor expansion of P^* shows that

$$P^*(\beta/2,R)\approx\bar{P}^*(R)\tag{3.40}$$

Using this, Eq. (3.37) becomes

$$\frac{6}{5}\left(\frac{\bar{V}_r}{W^2}\frac{\partial \bar{V}_r}{\partial R}-\frac{\bar{V}_\theta^2}{R}\right)=-\frac{\partial \bar{P}^*}{\partial R}-\frac{24\bar{V}_r}{W^2\mathrm{Re}_{\mathrm{m}}\beta^2}\tag{3.41}$$

Integrating over R to solve for $\bar{P}^*(R)$

$$\begin{aligned}&\bar{P}^*(1)-\bar{P}^*(R)\\&\quad=\int_R^1\left[\frac{6}{5}\left(-\frac{\bar{V}_r}{W^2}\frac{\partial \bar{V}_r}{\partial \varsigma}+\frac{\bar{V}_\theta^2}{\varsigma}\right)-\frac{24\bar{V}_r}{W^2\mathrm{Re}_{\mathrm{m}}\beta^2}\right]d\varsigma\end{aligned}\tag{3.42}$$

where ς is an artificial variable of integration. The total pressure drop across the entire channel can be found by integrating from R_i, the inner radius, to 1. So that the final total pressure drop is given by $\Delta\bar{P}^*_{tot} = \bar{P}^*(1) - \bar{P}^*(R_i)$, or

$$\Delta\bar{P}^*_{tot} = \int_{R_i}^{1} \left[\frac{6}{5}\left(-\frac{\bar{V}_r}{W^2}\frac{\partial\bar{V}_r}{\partial R} + \frac{\bar{V}_\theta^2}{R} \right) - \frac{24\bar{V}_r}{W^2\mathrm{Re_m}\beta^2} \right] dR \tag{3.43}$$

If the gap size is constant, $\beta = 1$, and the solution becomes

$$\Delta\bar{P}^*_{tot} = \int_{R_i}^{1} \left[\frac{6}{5}\left(-\frac{\bar{V}_r}{W^2}\frac{\partial\bar{V}_r}{\partial R} + \frac{\bar{V}_\theta^2}{R} \right) + \frac{24}{W^2\mathrm{Re_m}R} \right] dR \tag{3.44}$$

The integral can be numerically solved to find the total pressure drop across the channel.

Fluid and Wall Temperature Distributions

The generalized energy conservation equations can be written as

$$\rho\frac{Di}{Dt} - \nabla\cdot k\nabla T - \mu\Phi - \frac{DP}{Dt} - S = 0 \tag{3.45}$$

To solve for the temperatures through the device, the velocity distributions and idealizations from above are used as well as assuming:

- The fluid has constant thermal conductivity, density and specific heat. Assuming the temperature will not vary drastically through the channel
- One wall is perfectly insulated and the other wall has a constant heat flux, q''_w
- There is negligible viscous dissipation, Φ, and no source contributions, S

the governing equation becomes

$$\rho v_r c_p\frac{\partial T}{\partial r} - \frac{k}{r}\frac{\partial}{\partial r}\left(r\frac{\partial T}{\partial r} \right) - k\frac{\partial^2 T}{\partial z^2} = 0 \tag{3.46}$$

Using the following nondimensional parameters:

$$\Theta = \frac{T - T_o}{T_{b,i} - T_o} \tag{3.47}$$

$$\mathrm{Pr} = \frac{\mu c_p}{k} \tag{3.48}$$

$$\mathrm{Pe_m} = \mathrm{Re_m}\mathrm{Pr} \tag{3.49}$$

where Pr is the Prandtl number, Pe_m is a modified Peclet number, and T_b is the bulk fluid temperature defined by

$$T_b = \frac{1}{b\bar{v}_r} \int_{-b/2}^{b/2} v_r T dz \tag{3.50}$$

Eq. (3.46) can be written as

$$\frac{\partial \Theta}{\partial R} - \frac{2\varepsilon^2}{\text{Pe}_\text{m} V_r R} \frac{\partial}{\partial R} \left(R \frac{\partial \Theta}{\partial R} \right) - \frac{2}{\text{Pe}_\text{m} V_r} \frac{\partial^2 \Theta}{\partial Z^2} = 0 \tag{3.51}$$

The second term above, representing the radial conduction, is of order $\varepsilon^2/\text{Pe}_\text{m} << 1$. This term can be neglected when compared to the first and last terms, the radial advection and the axial conduction, respectively. The wall boundary conditions can be written as

$$\left. \frac{\partial \Theta}{\partial Z} \right|_{\beta/2} = 0 \tag{3.52}$$

$$\left. \frac{\partial \Theta}{\partial Z} \right|_{-\beta/2} = - \frac{q''_w b_o}{k(T_{b,i} - T_o)} \tag{3.53}$$

By using conservation of energy over the entire surface the last boundary condition can be written as

$$\frac{q''_w b_o}{k(T_{b,i} - T_o)} = \frac{\text{Pe}_\text{m}}{1 - R_i^2} \tag{3.54}$$

Thus, integrating Eq. (3.51) over $-\beta/2$ to $\beta/2$ and dividing by β

$$\frac{\bar{V}_r}{\beta} \int_{-\beta/2}^{\beta/2} \phi \frac{\partial \Theta}{\partial R} dZ - \frac{2}{\beta(1 - R_i^2)} = 0 \tag{3.55}$$

Using the fact that

$$\Theta_b = \frac{1}{\beta} \int_{-\beta/2}^{\beta/2} \phi \Theta dZ \tag{3.56}$$

and assuming the device is designed with a small gap slope, $\alpha << 1$ so that the terms of $O[\alpha]$ can be neglected, results in

$$\frac{\partial \Theta_b}{\partial R} = - \frac{2R}{(1 - R_i^2)} \tag{3.57}$$

Solving for Θ_b and using the boundary condition that $\Theta_b(R = 1) = 0$, results in

$$\Theta_b(R) = \frac{1 - R^2}{1 - R_i^2} \tag{3.58}$$

Streamlines for an example flow in the device are shown in Fig. 3.2 with the shade of the streamline representing the temperature of the flow through the channel. The fluid heats up as it flows through the channel entering at $R = 1$ and exiting at $R = 0.1$ with $\Theta_b = 0$ to 1. To solve for the wall temperatures, it is assumed that the Nusselt number, Nu, for the flow is constant. Where

$$\mathrm{Nu} = \frac{h(2b)}{k} \tag{3.59}$$

and the temperature can be found from the constant wall heat flux

$$q''_w = h(T_w - T_b) \tag{3.60}$$

Defining a dimensionless wall temperature based on the heat flux, q''_w,

$$\Theta_w = \frac{h(T_w - T_o)}{q''_w} \tag{3.61}$$

allows computation of T_w in dimensionless form as

$$\Theta_w(R) = \frac{(1 - R^2)\mathrm{Nu}}{2\mathrm{Pe_m}\beta} + 1 \tag{3.62}$$

If the gap size is constant, $\beta = 1$, and the solution becomes

$$\Theta_w(R) = \frac{(1 - R^2)\mathrm{Nu}}{2\mathrm{Pe_m}} + 1 \tag{3.63}$$

A solution for fluid temperature and heat flux distributions is also found based on a constant wall temperature condition. By replacing the boundary condition in Eq. (3.53) by

$$-k\frac{\partial T}{\partial z}\bigg|_{-\beta/2} = h(T_w - T_b) \tag{3.64}$$

the energy equation can be solved using a normalized bulk temperature,

$$\Theta_{b,T} = \frac{T_b - T_w}{T_o - T_w} \tag{3.65}$$

Solving this using the same methods as above gives,

$$\Theta_{b,T}(R) = \beta^{\frac{(\alpha-1)\mathrm{Nu}}{\alpha^2\mathrm{Pe_m}}} \exp\left[\frac{\mathrm{Nu}}{\mathrm{Pe_m}\alpha}(R - 1)\right] \tag{3.66}$$

If the gap size is constant the solution is

$$\Theta_{b,T}(R) = \exp\left[\frac{\mathrm{Nu}}{2\mathrm{Pe_m}}(R^2 - 1)\right] \tag{3.67}$$

The total heat flux along the wall can be found by solving for

$$q''_w(R) = h(T_w - T_{b,T}) \tag{3.68}$$

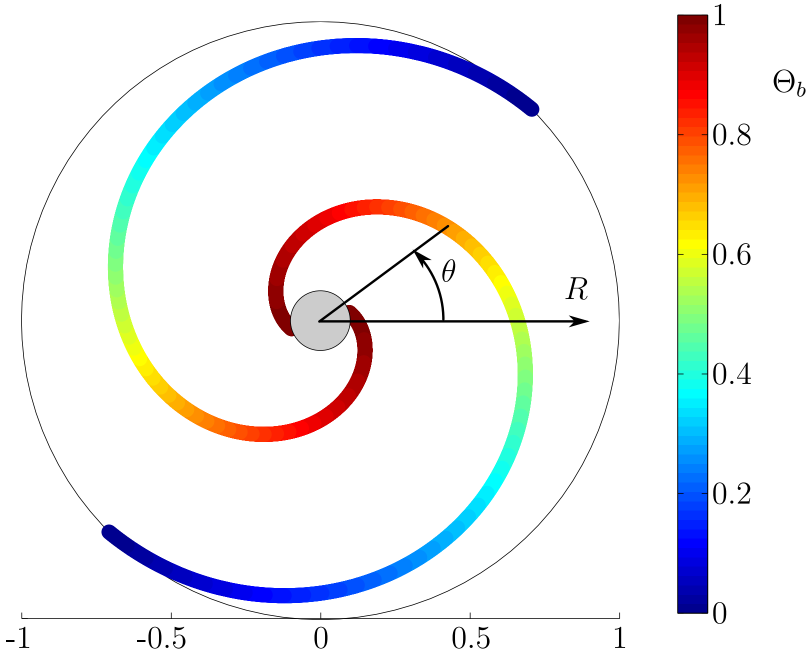

Figure 3.2: Streamlines of the flow showing the normalized fluid temperature through the flow path, using W=10, Re$_m$= 5, α=1/5, and R_i=0.1.

or

$$q''_w(R) = h\Theta_{b,T}(T_w - T_o) \tag{3.69}$$

The experiments which are discussed in this study use value ranges in which the flow are expected to have enhanced heat transfer coefficients and are also expected to be largely thermally developing and partially hydrodynamically developing. Thus, the constant Nusselt number assumption breaks down, and it is recommended to use experimental values for $\mathrm{Nu_m}$ based on the specific device. These values are given in Sec. 5.3.

Parametric Analysis

The nondimensional formulations of temperature and pressure can allow for parametric optimization of a system which can be used to aid in designing a device. Desirable ranges of the important dimensionless parameters can be found through analysis of the closed form solutions to the pressure and temperature distributions in the flow for the constant wall heat flux case. The dimensionless term, $\Delta\bar{P}^*_{tot}$, represents the bulk pressure head across the channel normalized by a characteristic inertial force in the flow, $\rho v^2_{\theta,o}$. From Eq. (3.43), the total normalized pressure drop, $\Delta\bar{P}^*_{tot}$, for a varying gap height can be seen to be a function

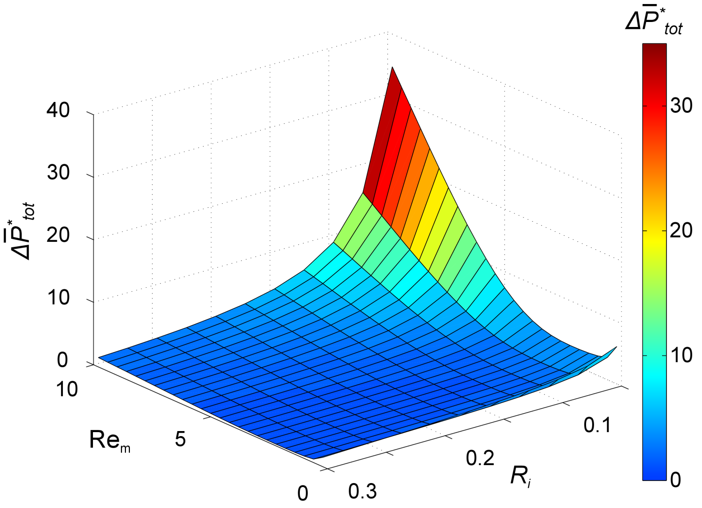

Figure 3.3: Dimensionless pressure as a function of the modified Reynolds number and R_i for a constant gap size and W=10

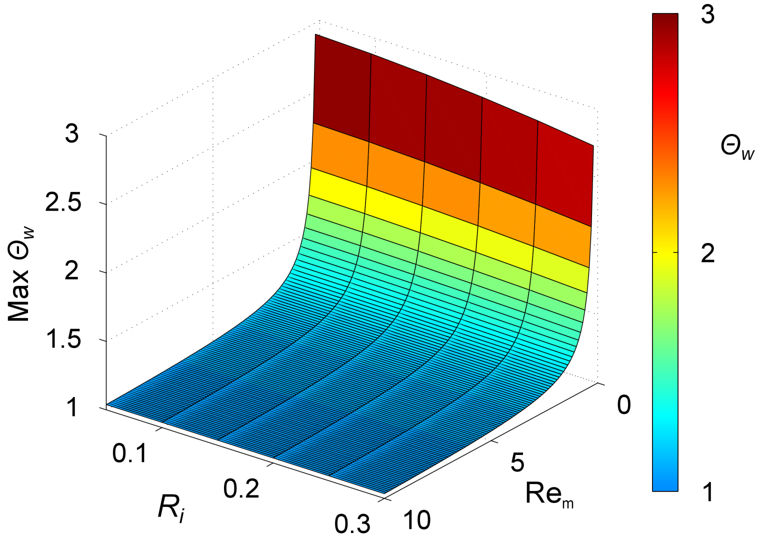

Figure 3.4: Maximum normalized wall temperature as a function of the modified Reynolds number and R_i for a constant gap size and Pr = 7

of only four parameters, R_i, W, Re_m, and α. The dimensionless wall temperature, Θ_w, represents the ratio of the maximum possible heat flux from the surface, $h(T_w - T_o)$, to the actual heat flux, q''_w. From Eq. (3.62), Θ_w for a varying gap height is a function of only R, Re_m, Pr, and α. For a constant gap height the pressure drop and wall temperature are not a function of α.

Because R_i affects the total pressure drop only by being a limit of integration, it is clear that a larger value of R_i would lead to a smaller pressure drop across the device by reducing the flow length. This trend is seen in Fig. 3.3 which shows the dimensionless pressure drop for different values of the modified Reynolds number and R_i for a constant gap size condition. As seen in Fig. 3.3, values lower than 0.1 tend to significantly increase the dimensionless pressure drop. The temperature is also affected by R_i since the maximum wall temperature is typically found towards the center of the device, so a shorter flow length here is also desired. However, as seen in Fig. 3.4 the value for R_i does not significantly change the maximum wall temperature. In addition, total flow coverage of the surface is important, so the largest possible value of R_i that would allow for complete cooling of the surface would be needed to prevent the development of a hot spot in the center of the device. Otherwise placing the devices to be cooled only under the flow coverage areas would be necessary.

W represents the ratio of initial velocity in the tangential direction to the initial velocity in the radial direction. This value is dictated by the size of the inlet flow area relative to the total circumferential area of the device. The magnitude of the tangential flow velocity does not affect the heat transfer because of the idealization that the flow is axisymmetric. Thus, in order to get the smallest total pressure drop for a given heat rate, a small tangential flow to radial flow ratio,W , is desired. However, as W increases, holding all else constant, the normalized pressure drop decreases. This is due to the increased inertial forces cause by the larger θ-direction velocity, and does not indicate a desirable operating space for the device. Rather the device should operate in a way which allows the flow to be evenly distributed over the surface but keeps the velocity ratio, W, low. Visualizing the streamlines as in Fig. 3.2, can help to achieve this goal.

The modified Reynolds number, Re_m, is important in both the heat transfer and the pressure drop in the device. Equation (3.27) shows Re_m consists of the inlet radial Reynolds number multiplied by the aspect ratio, ε. Figures 3.5 and 3.6 show how both the normalized wall temperature and the pressure drop vary with this value. The optimal modified Reynolds number from Fig. 3.5 falls within the range when the normalized pressure drop is around 1, corresponding to values of $\mathrm{Re}_m \approx$ (1-5). In the figure, the value of the velocity ratio, W, is held constant at 10. Varying W slightly from this value leads to similar curves, and further increasing W to larger values may undesirably transition the flow into the turbulent regime as well as increase the pressure drop. From Fig. 3.6 it is clear that a higher Reynolds number is desired to maintain a lower wall temperature. However, beyond a value of about $\mathrm{Re}_m =$ 1, the wall temperature quickly approaches the lower limit at $\Theta_w = 1$. Thus, values of the modified Reynolds number between 1 to 5 are desired to ensure lower pressure drops and wall temperatures.

A value of 0.2 was used for the dimensionless gap slope α in Figs. 3.5 and 3.6. Because

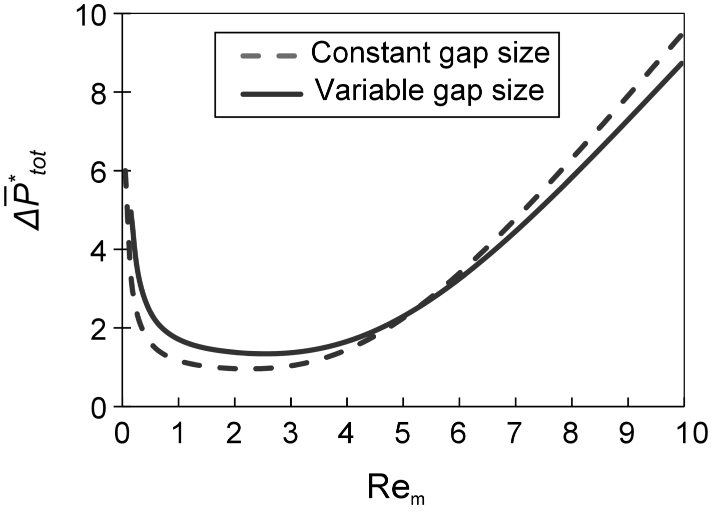

Figure 3.5: Normalized total pressure drop as a function of the modified Reynolds number for W=10, α=1/5, and R_i=0.1.

of the assumption that $\alpha << 1$ in calculating the bulk temperature, 0.2 was chosen as an upper bound for α to avoid errors caused by this assumption. For values of α less than 0.2 the temperature and pressure distributions simply converge to the constant gap size distributions seen in Figs. 3.5 and 3.6.

From Eq. (3.62), the value of the Prandtl number can be seen to affect the maximum wall temperature in the channel. In addition, the pressure drop is not dependent on the Prandtl number because viscosity effects are already taken into account through the Reynolds number. Fig. 3.7 shows how the maximum wall temperature varies due to the Prandtl number for different values of the modified Reynolds number at a constant R_i. For small Prandtl number the maximum temperature is the highest. As the Prandtl number increases the maximum temperature quickly decreases and then remains low as the Prandtl number further increases. Thus materials with high Prandtl number might be desirable for cooling, such as ethylene glycol or mixtures of water and ethylene glycol which have values up to Pr = 100 [57].

Within the most desirable ranges discussed, the device with a constant gap size revealed lower pressure drop and higher wall temperature characteristics than the linearly variable gap size, having slope α, as seen in Figs. 3.5 and 3.6. Thus tapering the channel as seen in the bottom cross-section of Fig. 2.1 while beneficial to the design from a cooling point of view may lead to increased pressure penalties.

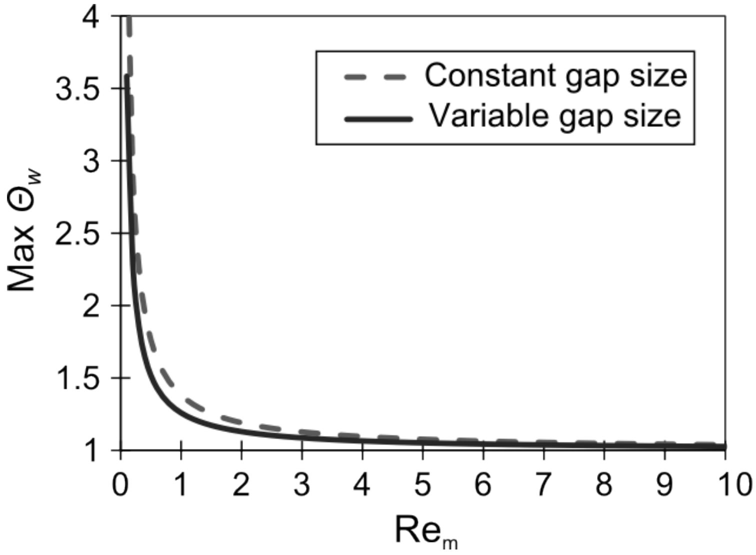

Figure 3.6: Maximum normalized wall temperature as a function of the modified Reynolds number for α=1/5, and R_i=0.1, Pr = 7.

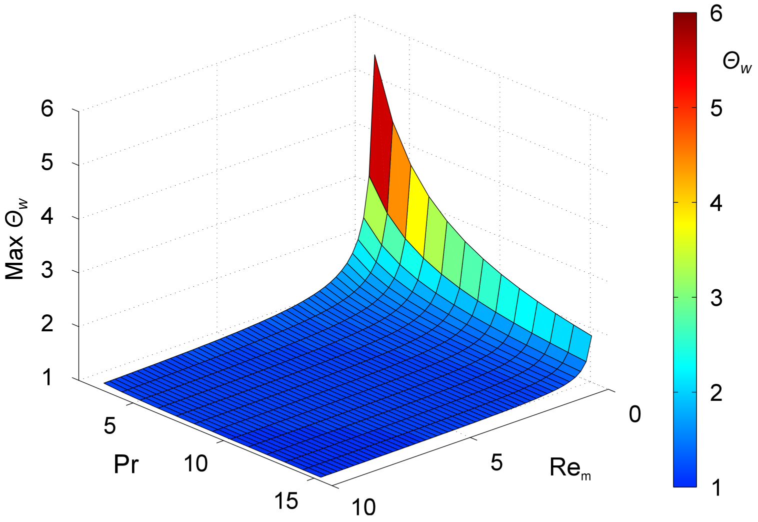

Figure 3.7: Maximum normalized wall temperature as a function of the modified Reynolds number and Prandtl number for a constant gap size and R_i=0.1

3.2 Two Phase and Boiling Heat Transfer Theory

Boiling Heat Transfer

In order to prevent dryout at high fluxes, low exit qualities and subcooled flow in a microchannel device would be desired. For subcooled flow boiling in a microchannel, the forced convective contribution is expected to be large. To predict the heat transfer properties in the channel, thus the contributions of both single phase forced convective effects and nucleate boiling heat transfer must be accounted for. Analysis adapted from Rohsenow [58] suggested adding the single phase and two phase components of total heat flux as

$$q''_{tot} = q''_{sp} + q''_{nb} \tag{3.70}$$

where q''_{sp} is the single phase contribution

$$q''_{sp} = h_l(T_w - T_{b,l}) \tag{3.71}$$

For a spiraling inflow heat sink, correlations for h_l, the heat transfer coefficient of liquid only in the channel, can be found in Sec. 5.4. q''_{nb} is the nucleate boiling contribution which can be found using a correlation for nucleate pool boiling (of which many may be chosen). The correlation suggested by Rohsenow is used in this study:

$$q''_{nb} = \mu h_{lv} \left(\frac{1}{C_{sf}}\right)^{1/r} \mathrm{Pr}_l^{-s/r} \left[\frac{c_{p,l}\,(T_w - T_{sat})}{h_{lv}}\right]^{1/r} \left[\frac{g(\rho_l - \rho_v)}{\sigma}\right]^{1/2} \tag{3.72}$$

Where values of $C_{sf} = 0.0128$, $r = 0.33$ and $s = 1$ are used. The use and validity of this method for predicting subcooled boiling curves is evaluated in Chap. 6.

Nondimensional Characteristics of Two Phase Flow

Important nondimensional parameters can provide insight into the nature of the microchannel flow. Comparison of acceleration, surface tension, inertial and viscous forces based on important nondimensional parameters can indicate which driving forces will aid in heat transfer enhancement.

The Bond number can provide insight into the effects of forces due to acceleration versus surface tension. For this system, the Bond number is defined based on centripetal acceleration in a spiraling inflow:

$$\mathrm{Bo_c} = \frac{(\rho_l - \rho_v)a_c b^2}{\sigma} \tag{3.73}$$

Here the characteristic length chosen is b, the channel height. The centripetal acceleration, a_c is found as:

$$a_c = \bar{v_\theta}^2/r \tag{3.74}$$

Using the single phase theoretical model for the velocity profile, Bond numbers were found for an experimental device with dimensions given in Table 4.1 and saturated water. This definition of the bond number is representative of a vapor bubble in low quality flow. For the lowest flow rate tested, $G_m = 184$ kg/m^{2}s, the Bond number values ranged from $\mathrm{Bo_c} = 0$ to 0.036. For the highest flow rate, $G_m = 716$ kg/m^{2}s, they ranged from $\mathrm{Bo_c} = 0.33$ to 7.9. These values suggest centripetal effects may aid in the removal of vapor from the surface, especially at higher flow rates. The Bond number for gravitational acceleration is $\mathrm{Bo_g} = 0.015$, showing that gravity effects are insignificant as is expected for small channels.

The Weber number provides a comparison of the dynamic pressure effects versus surface tension forces, and is defined as:

$$\mathrm{We} = \frac{G_m^2 b}{\rho_l \sigma} \tag{3.75}$$

Here the characteristic length is the channel height and the density is used as saturated liquid water (since very low qualities are expected). Again, using values for an experimental device with dimensions given in Table 4.1 and saturated water, for the lowest flow rate tested, $G_m = 184$ kg/m^{2}s, the Weber number ranged from We = 0.075 to 1.6. For the highest flow rate,$G_m = 716$ kg/m^{2}s, they ranged from We = 9.1 to 67. These values suggest dynamic forces will aid in the removal of vapor from the surface.

The Capillary number provides a metric on comparing viscous to surface tension forces, and is defined as

$$\mathrm{Ca} = \frac{\mu_l G_m}{\rho_l \sigma} \tag{3.76}$$

For all flow rates tested, the highest value is about 0.06, indicating viscous forces are not significant in the vapor removal process.

Bubble Size and Flow Constriction in a Microchannel

In Mudawar [1], a mechanistic definition of two phase in a microchannel is postulated as flow in which vapor bubbles will constrict the flow. In this study, a characteristic bubble diameter is found from a balance of drag to surface tension forces on the bubble. For water at a mass flux of 1000 kg/m^{2}s the transition hydraulic diameter is 1 mm, with increasing diameters for lower mass fluxes. Thus, for the cases in the experimental system discussed in Chapter. 6, the flow is considered a microchannel with mean mass flux levels G_m <1000 kg/m^{2}s and a hydraulic diameter of $2b = 600$ μm.

For subcooled boiling in the channel, a large range of nucleation sites may be inactive even at high wall superheats, due to subcooled fluid suppressing the growth of vapor bubbles. Alternatively, larger active nucleation sites may lead to obstructed flow in the microchannel. Thus, calculating the range of active cavity sizes allows for better understanding of the flow regimes in the system. Active cavity radius estimates can be found using Hsu's analysis adapted from [59]

$$\left\{ \begin{matrix} r_{c,max} \\ r_{c,min} \end{matrix} \right\} = \frac{\delta_t}{4} \left(1 - \frac{T_{sat} - T_\infty}{T_w - T_\infty} \pm \left[\left(1 - \frac{T_{sat} - T_\infty}{T_w - T_\infty} \right)^2 - \frac{12.8 \sigma T_{sat}(P_l)}{\rho_v h_{lv} \delta_t (T_w - T_\infty)} \right]^{1/2} \right) \tag{3.77}$$

Here, $r_{c,max}$ and $r_{c,min}$ are the maximum and minimum active cavity sites, δ_t is the thermal boundary layer at the surface estimated from:

$$\delta_t = h/k_l \tag{3.78}$$

Fluid properties are found at T_{sat}, and T_∞ is the bulk fluid temperature. A discussion on the effect of active cavity sites for the experimental system tested is discussed in Chapter 6.

Chapter 4

Experimental Methods

4.1 Device Fabrication

The analytical models discussed in Chapter 3 motivated the fabrication of an experimental device that could assess the validity of the theoretical models and quantify the pressure drop and heat transfer properties of a device with spiraling inflow. Figure 4.1 shows a top view of the experimental test section. The device consists mainly of two parts: a bottom thermally conducting portion fabricated from copper alloy 145, and a top insulating cover part made from either polycarbonate or Ultem$^{\text{TM}}$ thermoplastic with identical construction, and labeled throughout the dissertation as device PC and device U, respectively. Two identical copper pieces were fabricated, labeled device 1 and 2 accordingly. Table 4.2 shows the labels used throughout this study for each device consisting of a pair of parts.

The devices were fabricated using simple machining techniques on a lathe and mill.

Table 4.1: Important dimensions in experimental device

Parameter	**Size**
b	300 μm
r_o	1 cm
r_i	0.15 cm
W	6

Table 4.2: Labels for devices used throughout dissertation. The two bottom copper pieces were made with identical construction from the same material. The two plastic cover pieces also had identical construction.

	Ultem$^{\text{TM}}$ThermoPlastic	**Polycarbonate**
Copper Piece 1	Device U1	Device PC1
Copper Piece 2	Device U2	not tested

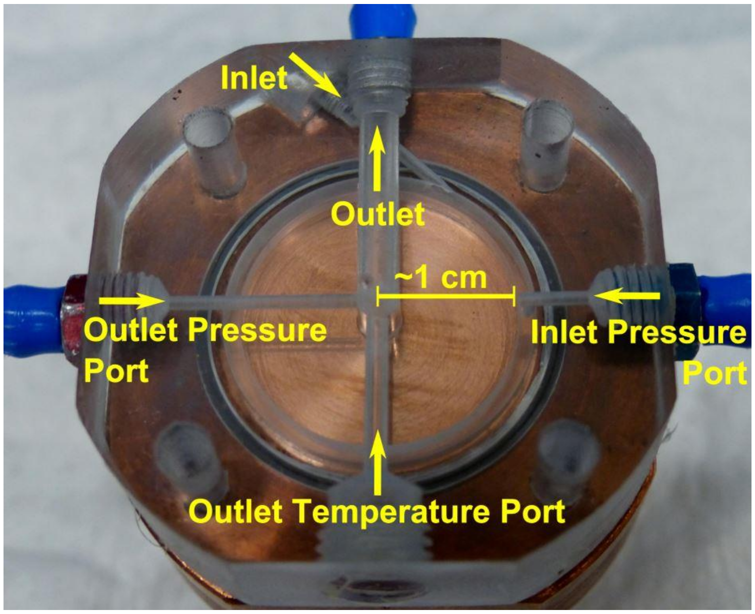

Figure 4.1: Top view of fabricated device

Important heat sink design parameters are shown in Table 4.1. A gap size of 300 μm was chosen based on estimated pressure drops as well as machinability of these dimensions on a lathe. A radius of 1 cm was chosen based on typical size of systems desired for electronics cooling applications. The inlet feeder region is located in the plastic cover and consists of a uniform channel of cross section, A_c, 2.5 mm deep x 1.25 mm wide, which was designed to provide a inlet tangential to radial flow ratio of $W = 6$, where $W = \bar{v}_{\theta,o}/\bar{v}_{r,o}$. This was predicted to provide a uniform flow distribution over the heated surface. The plastic cover also contains the outlet port and connections for the pressure transducers and outlet thermocouple probe as seen in Fig. 4.1. The bottom of the copper piece has three bored holes for cartridge heaters which act as the heat source for testing the heat sink design. Twelve holes for thermocouple probes which measure temperature within the copper at four different radial locations are located along three sides of the device. The two pieces are held together with steel screws and an aluminum frame which uniformly compresses the plastic cover and o-ring onto the copper to seal the device. A side view of the device fully set up is shown in Fig. 4.2. Thermocouple locations are shown in Fig. 4.3. Full CAD drawings with dimensions are shown for the heat sink device in Appendix C.

4.2 Experimental Equipment and Instrumentation

Figures 4.4 and 4.5 show the schematic of the experimental set up in the lab. Distilled water was used as the working fluid. A gear pump rated up to 1630 ml/min and 20 psi

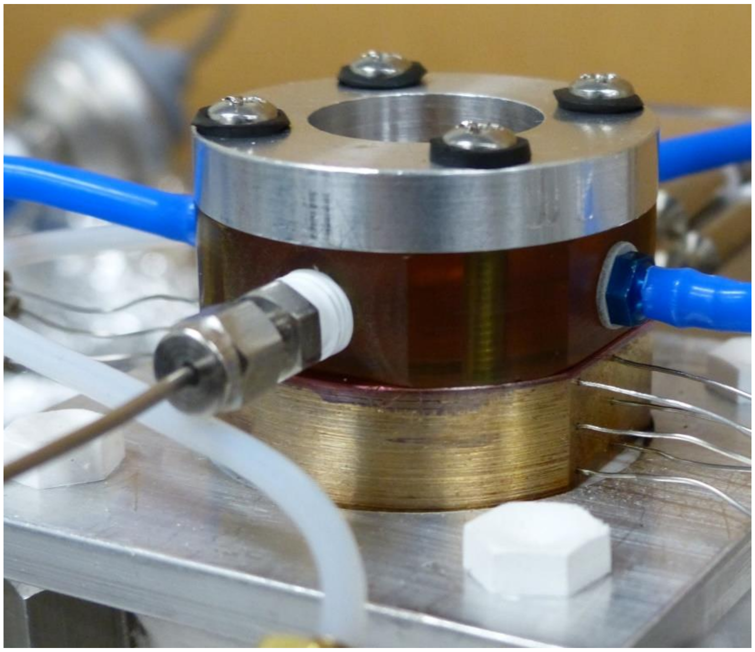

Figure 4.2: Side view of experiment set up on test rig

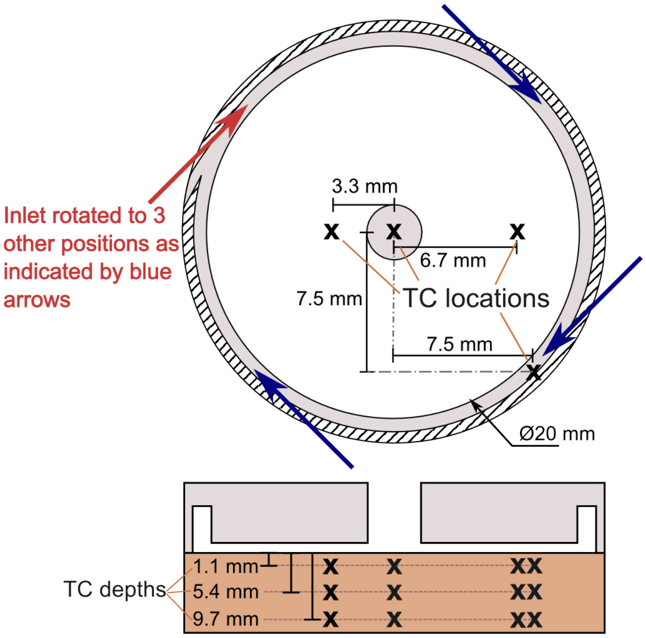

Figure 4.3: Locations of the thermocouples (TCs) within the copper piece and the relative inlet orientations tested

maintained the flow at a constant pressure and flow rate through the system. The flow rate was controlled through a needle valve upstream of the pump, after passing through a 40 μm filter. The flow then passed through a rotameter to measure the flow rate of the system. Two preheaters rated up to 400 W (240VAC) each were set up downstream of the rotameter and controlled by one variable AC (Variac) power supply. The inlet temperature was measured before it flowed into the heat sink. Three Watlow cartridge heaters which output 400 W at 120 VAC were inserted into the bottom of the heat sink. The total power into the heaters was controlled by three separate Variac power supplies which provide the desired heat level. After being heated in the device the water was cooled in a heat exchanger consisting of a coiled copper tube submerged in a cold water or ice water bath. The water then flowed into a 1 gallon reservoir for pumping back into the system. Thermal insulation was wrapped around the bottom of the heat sink and around the top exposed copper regions.

The pressure drop in the system was measured with two Cole-Parmer pressure transducers with ranges 0-345 kPa (50 psi) and an accuracy of 0.25% of full scale. The pressure transducers were connected to the test section through tubing leading into pressure ports with locations shown in Fig. 4.1. The inlet and exit temperatures were measured using T type thermocouple probes from Omega with a diameter of 1/16 in. A thermocouple inserted into the port shown in Fig. 4.1 measured the outlet temperature, and the inlet temperature was measured just upstream of the device inlet shown in Fig. 4.1. It is assumed the outlet thermocouple measures the mean temperature in the outlet channel. This assumption is validated by flow visualization studies discussed in Sec. 5.2, where the dye can be seen to be well mixed in the outlet for all but the lowest flow rate. Additionally, the thermocouple extends halfway through the exit channel, with a corresponding Biot number less than or around 0.1, meaning the tip will measure the mean temperature flowing over this region, even for lower flow rates where mixing might not be complete. The thermocouple is inserted into the plastic cover piece, and thus is essentially insulated from all other regions. The temperature within the copper device was measured using T type thermocouple probes from Omega with a diameter of .02 in. Pressure and temperature data were acquired using National Instruments Data Acquisition systems (DAQs) and LabVIEW software. The mass flow rate was measured using one of two 65 mm variable area rotameters from Omega Engineering for different flow ranges. The lower flow rate rotameter measures up to 70.7 ml/min of water with 2% full scale accuracy. The higher flow rate rotameter measures up to 387 ml/min. It was calibrated using distilled water at room temperature and a triple beam balance giving an average error of 1.3 ml/min. The power into the heaters were monitored using P3 Kill A Watt electricity monitors which have 0.2% Accuracy. Table 4.3 lists the measurement ranges and errors of the instrumentation used. This does not include the DAQ errors associated with the measurements and which are included in the error analysis. The method of determining the uncertainty for these measurements is discussed in Appendix D.

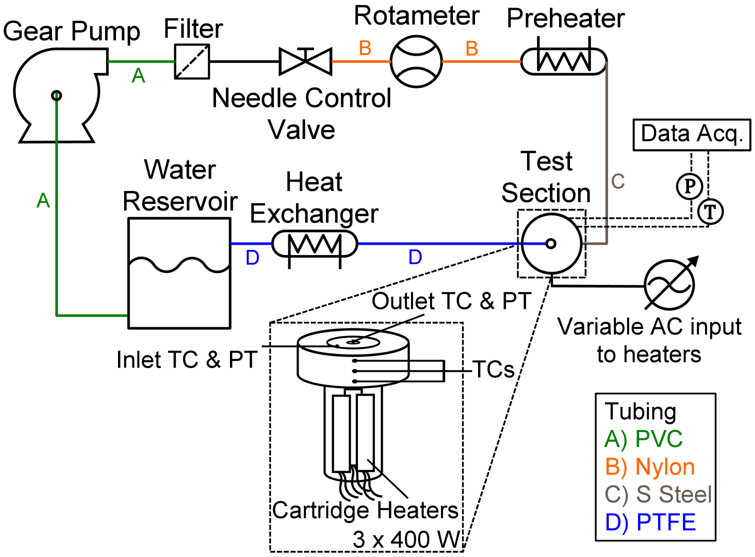

Figure 4.4: Schematic of experimental components

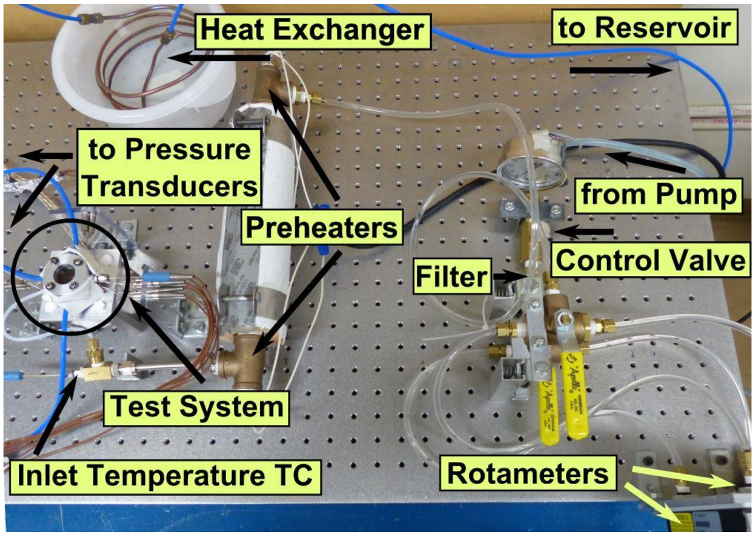

Figure 4.5: Setup of experimental components in the laboratory

Table 4.3: Instrumentation range and accuracy used for experimental results

Measurement	**Device Range**	**Accuracy**
Volumetric Flow Rate	0-387 ml/min	1.2 ml/min
Pressure	0-345 kPa	0.86 kPa
Temperature	up to 350°C	greater of 0.5°C or 0.4%(from 0°C)
Power	–	0.2%

4.3 Testing Procedure

The heat sink was assessed for heat transfer and pressure drop properties over a range of flow rates and heat inputs. For pressure drop tests at room temperature the pressure at the inlet and outlet at each flow rate was recorded for 30 seconds and averaged over three tests. For heat transfer tests the following procedure was followed:

1. Turn on the pump and adjust control valve until the desired flow rate is reached
2. Plug in and turn on the cartridge heaters, and adjust the Variacs to the desired heat rate
3. Wait for the system to reach steady state. While this is done visually, analysis shows there was a temperature variation of at most 1.2 °C/min and 98% of the temperature variations were within 0.8°C/min for single phase flow. For two phase flow, 98% of the average temperature variations were within 2.0°C/min.
4. Record temperature data for over 1.5 minutes and pressure data (if recorded) for about 30 seconds
5. Go to step 3 and repeat for all desired heat rates
6. Let system cool back to room temperature and repeat all steps for all desired flow rates

For tests with preheated fluid temperatures, the preheaters were adjusted until the desired inlet temperature was reached. This inlet temperature was monitored throughout testing. Ice was replenished as needed in the heat exchanger cold water bath throughout testing to ensure that the inlet temperature was maintained at room temperature (18-24°C). The flow rate was always checked after adjusting heat input to ensure accurate measurements.

4.4 Experimental Calculations

The temperature and pressure data was accrued using LabVIEW software and imported to MATLAB for processing. For each flow rate and heat rate pair tested, the set of tem-

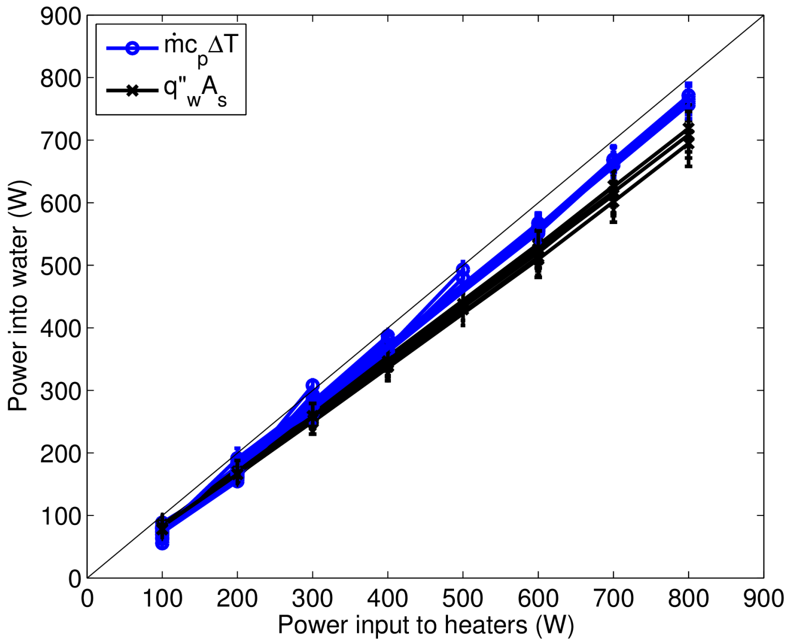

Figure 4.6: Comparison of two methods for measuring heat rate into fluid

perature data was calculated by averaging over 1.5 minutes of steady state data. For single phase tests, the total heat into the water was calculated as

$$\dot{Q} = \dot{m}c_p(T_i - T_o) \tag{4.1}$$

using the measured flow rate and inlet and outlet fluid temperatures. For boiling tests, the total heat into the water was calculated from a discretized integrated total of the heat flux from the lower two thermocouples at each radial location.

$$\dot{Q} = -\int_{-r_o}^{r_o} \frac{k_{\mathrm{Cu}}(T_{mid}(r) - T_{bot}(r))}{\Delta z}\pi r dr \tag{4.2}$$

This average was taken because the asymmetry in the heaters did not provide uniform heat flux through the thermocouple locations. However, this method agreed well with the total heat rate into the water for single phase heat transfer measured from the bulk fluid temperature difference. Comparison of the two methods for single phase tests is shown in Fig. 4.6. This data revealed a total average system loss of 12% of the power input, ranging from 4 to 22% over all tests. The top insulating portion of the device is made from plastic with a thermal conductivity more than 1000 times less than that of copper; therefore, negligible heat is expected to flow into the fluid from the plastic cover. Thus, the average heat flux to the surface, $\bar{q}''_w$, is calculated as the total heat into the water divided by the total heated copper surface area, A_{Cu}.

$$\bar{q}''_w = \frac{\dot{Q}}{A_{\mathrm{Cu}}} \tag{4.3}$$

For the device tested, $A_{\mathrm{Cu}} = 4.18\ \mathrm{cm}^2$. This value includes the portion of the surface heated below the feeder channel. This area is likely to have different heat transfer properties than the microchannel region but it is assumed heat is still dissipated here. The surface temperature, T_w, was calculated by using the average heat flux and the thermocouple measurement closest to the top at each radial location as:

$$T_w(r) = T_{top}(r) - \frac{\bar{q}''\Delta z}{k_{\mathrm{Cu}}} \tag{4.4}$$

Here the value for thermal conductivity of Copper Alloy 145 $k_{\mathrm{Cu}} = 355$ W/mK was used, and the distance from the surface to the top thermocouple is $\Delta z = 1.1$ mm. Because the thermocouple distance to the top is small, using the average heat flux won't lead to large errors in the surface temperature. To calculate the heat transfer coefficient a predicted fluid temperature at location r was calculated from an energy balance as the total sensible heat into the water or the saturation temperature

$$T_b(r) = \min\left[T_{sat}, \frac{q''_w(\pi(r_o^2 - r^2))}{\dot{m}c_p} + T_o\right] \tag{4.5}$$

The heat transfer coefficient can then be found as

$$h(r) = \frac{\bar{q}''}{T_w(r) - T_b(r)} \tag{4.6}$$

Because three radial locations were recorded, the weighted average of the three locations was taken using:

$$\bar{h} = \frac{h_1A_1 + h_2A_2 + h_3A_3}{A_{tot}} \tag{4.7}$$

where the three areas are calculated using the mean radii between measurement locations, r_{mi}, as follows

$$A_1 = \pi(r_{m1}^2) \tag{4.8a}$$
$$A_2 = \pi(r_{m2}^2 - r_{m1}^2) \tag{4.8b}$$
$$A_3 = \pi(r_o^2 - r_{m2}^2) \tag{4.8c}$$
$$A_{tot} = A_1 + A_2 + A_3 \tag{4.8d}$$

The mean Nusselt number was calculated using the average heat transfer coefficient:

$$\mathrm{Nu_m} = \frac{\bar{h}d_h}{k_l} \tag{4.9}$$

For pressure data, the value was calculated by averaging over the recorded pressure data; the pumping power was calculated from:

$$\dot{\mathcal{W}} = \dot{m}(P_{in} - P_{out}) \tag{4.10}$$

The method of determining the uncertainty propagation through each of these calculations is discussed in Appendix D.

Chapter 5

Single Phase Experimental Results

5.1 Pressure Measurements

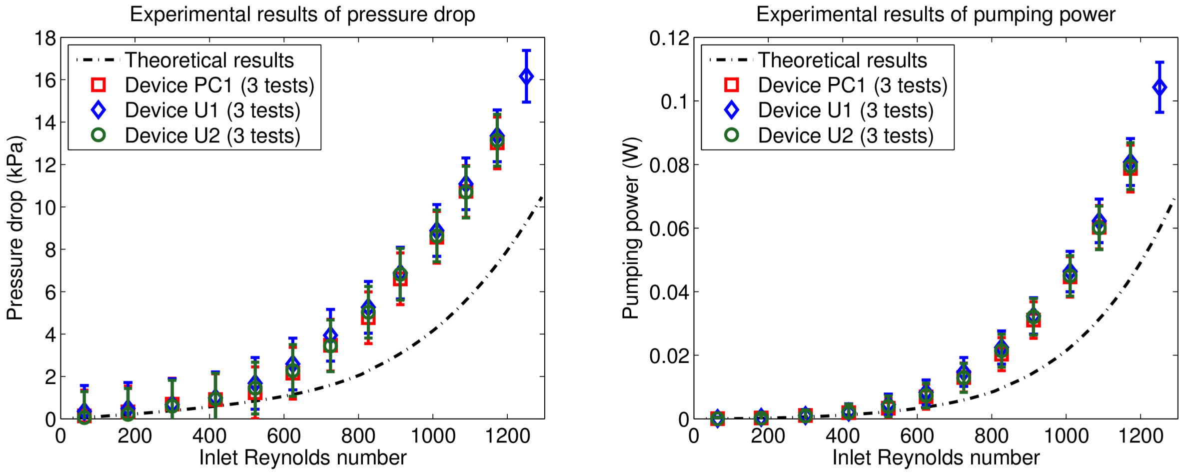

(a) Pressure drop (b) Pumping power

Figure 5.1: Experimental results from pressure drop tests at room temperature for three devices over the range of flow rates tested in the system

The pressure drop across the system was measured at room temperature (21-23° C) for flow rates up to 387 ml/min, corresponding to inlet total Reynolds numbers of up to 1250. The inlet Reynolds number is calculated from:

$$\mathrm{Re_o} = \frac{\sqrt{v_{r,o}^2 + v_{\theta,o}^2}\, d_h}{\nu} \tag{5.1}$$

Shown in Fig. 5.1, the results of the pressure drop experiments were consistent across three different devices with identical construction and labeled as described in Tab. 4.2. Figure 5.1a shows a comparison of the pressure drop to the theoretical model formulated in Sec. 3.1 and includes a model on the total pressure drop and gains associated with the inlet and outlet regions. Appendix E outlines the mathematical formulations for each of these pressure changes in the experimental device. The inlet and exit effects include the losses through the inlet and outlet channels and the sudden contraction of the inlet which are at most 5% of the total error in the data collection system. This also includes the pressure gain associated with the sudden expansion of the flow at the outlet which contributes a significant decrease in the theoretical pressure drop (at most 22% and on average 17% of the theoretical value). A model of increased friction losses in the developing region of the flow for axisymmetric flow adds at most 5% to the theoretical pressure drop and is not shown in Fig. 5.1a. This model is based on finding an apparent friction factor from data for laminar flow in parallel plates and adjusting the coefficient of the last term in Eq. (3.44) accordingly. The data show a fit to the analytic model within the error of the measurement system for low flow rates (up to $\mathrm{Re_o} \approx 620$) and divergence from the model for higher flow rates. For the values above $\mathrm{Re_o} = 620$ the data is on average 76% higher than the analytical prediction. The total pumping power for each of these flow rates is shown in Fig. 5.1b and is also compared to the theoretical model using Eq. (4.10). The largest expected pumping power at room temperature was about 0.1 W.

The discrepancy between the theory for pressure drop and the data is likely attributed to asymmetries in the flow distributions which lead to increased pressure drop in the experimental device due to inertial and friction loss in the higher flow regions. Additional dissipation in the entrance and exit regions, not predicted by the model, may also lead to increased pressure losses. The largest predicted Reynolds number was about 2160 at the outlet for the highest flow rate tested at room temperature. This indicates the flow is generally in the laminar flow regime yet approaches the transition region for the higher flow rates tested. As a result, certain regions of the flow may be transitioning to the turbulent regime or have instabilities which would lead to additional friction losses not accounted for by laminar theory. Taylor et al. [60] have also shown that surface roughness effects can lead to depression of the onset of turbulence in microchannels. Flow visualization studies, discussed in Sec. 5.2, provide visual evidence for unstable and turbulent regions in the flow for higher flow rates.

Data were recorded for the measured pressure drop with the addition of heat for higher flow rates ($\mathrm{Re_o} > 800$). Generally, the pressure drop increases as heat is added for the higher flow rates. For the data shown in Fig. 5.5 and discussed in Sec. 5.3, the pressure drop increases by as much as 60%. Although the viscosity of the fluid decreases as it heats up, the resulting increase in Reynolds number leads to turbulent regions in an increasingly larger portion of the flow which cause increased pressure losses. Indeed, the largest Reynolds number in the heated flow are expected to be turbulent, with maximum values at about 3800. This expected value was calculated using the laminar flow velocity distributions but accounting for a decrease in viscosity for the total Reynolds number calculations from Eq. (5.1).

Additional information on the diodicity of the device was also obtained. The pressure drop for the flow in reverse through the system was measured, where the inlet is now the axial center port and the outlet is the tangential outer port, and is shown in Fig. 5.2a. This

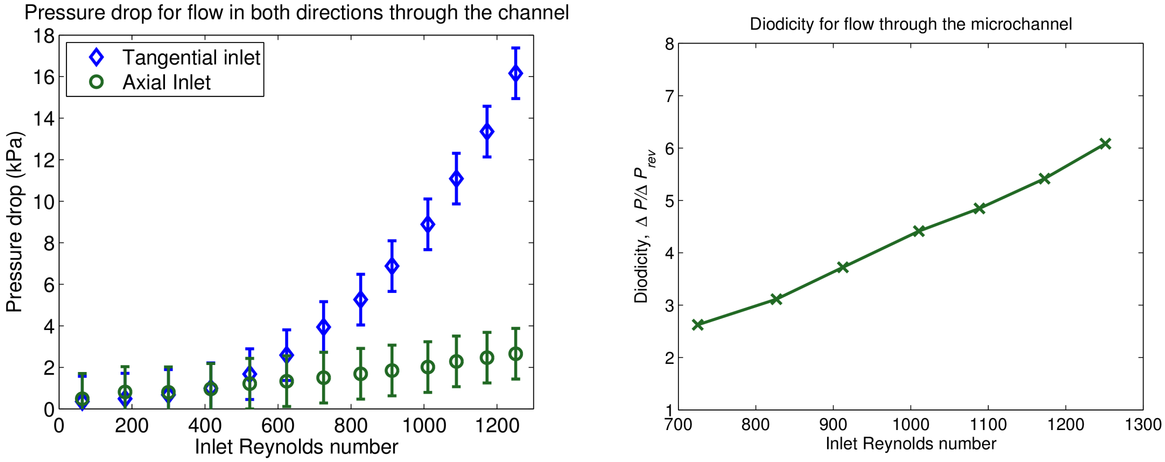

(a) Pressure drop

(b) Diodicity

Figure 5.2: Pressure drop tests for flow in reverse (axial direction) through the channel, compared to the tangential inlet direction used for heat transfer tests

reverse set up indicates a regime that has undesirable heat transfer characteristics due to assymmetry of the flow, however is a feature that can be desired for passive valve systems such as vortex diodes as discussed in Sec. 1.2. Diodicity, or the ratio of pressure in the tangential inlet direction over the axial inlet direction, is plotted in Fig. 5.2b, and shows increasing values as inlet Reynolds number increases. The peak diodicity for the system was 6 at the highest inlet Reynolds number tested, 1250. This is lower than experimental values previously studied in this type of geometry, however the range of Reynolds numbers tested is also much lower in this experimental set up. From Fig. 5.2 it can be seen that the value is likely expected to continue increasing at an increasing rate for higher Reynolds numbers. One key difference in this type of design from previous studies however, is the lack of nozzling at the inlet and outlet and the inlet feeder channel region.

5.2 Flow Visualization

Dyed water was injected through a port in the top polycarbonate cover to determine flow regimes for the range of flow rates tested. Videos and images were recorded. Figure 5.3 shows images of the transition of flow regimes at four different flow rates. For flow rates up to about $\mathrm{Re}_o = 620$ (190 ml/min), laminar properties were visible. The laminar flow showed distinct boundaries that indicated the dye did not visibly diffuse in the channel. The first two images in Fig. 5.3 show laminar properties with no fading of the dyed water line along the streakline. Above $\mathrm{Re}_o = 620$, diffusive effects became evident. In particular, the third and fourth images in Fig. 5.3 show the increased spread of the dyed water in the channel. The dyed water no longer had a distinct edge especially in regions close to the outlet of

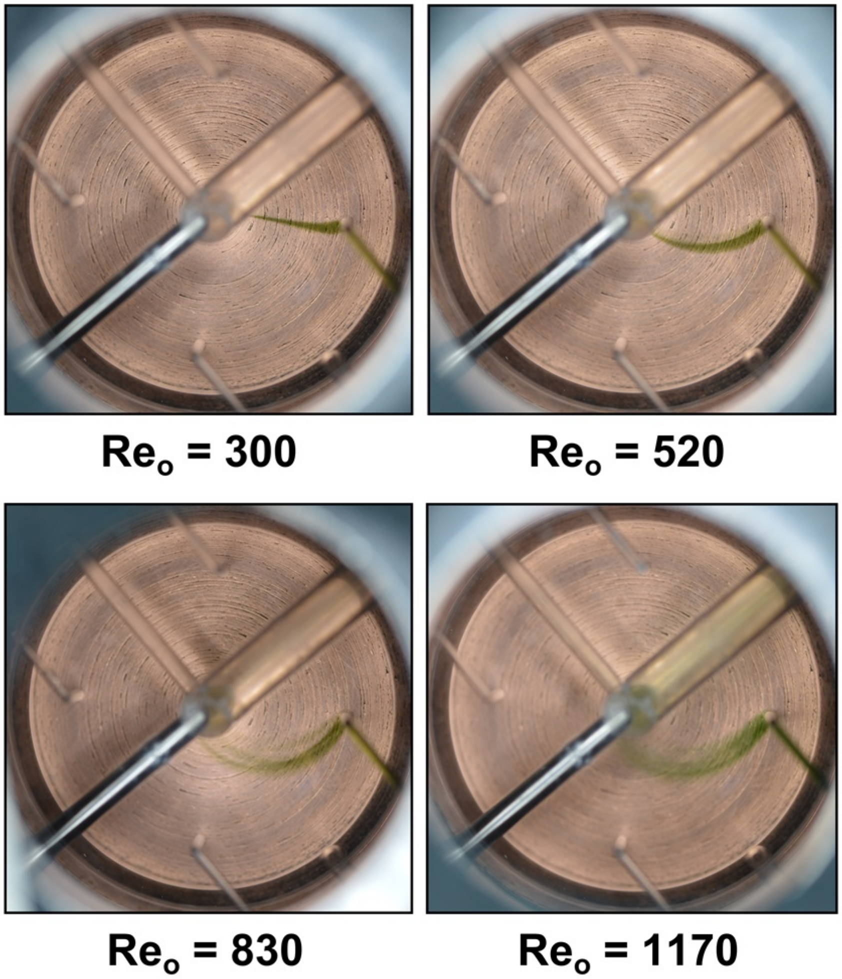

$Re_o = 300$ $Re_o = 520$

$Re_o = 830$ $Re_o = 1170$

Figure 5.3: Flow visualization using dyed water injected at r = 0.75 cm

the channel. This indicates that instabilities and possibly turbulent effects were causing the dyed water to spread before exiting the channel. This effect provides an explanation for the increased pressure drop and enhanced heat transfer in the device at higher flow rates. Even at the lower flow rates, video recordings showed oscillatory motions in the laminar streakline, indicating secondary flow motions are occurring. These motions will also tend to enhance dissipation of heat. Flow visualization studies also showed that the streaklines of the dye agreed well with expected streamlines of the flow from the theoretical analysis of Sec. 3.1. Two images are shown in Fig. 5.4 of superposed streamlines to the experimental images. This indicates, that although the pressure drop analysis may underestimate the flow, the theoretical velocity distributions can still provide a good metric for the extent of flow spread in the system through the streamlines.

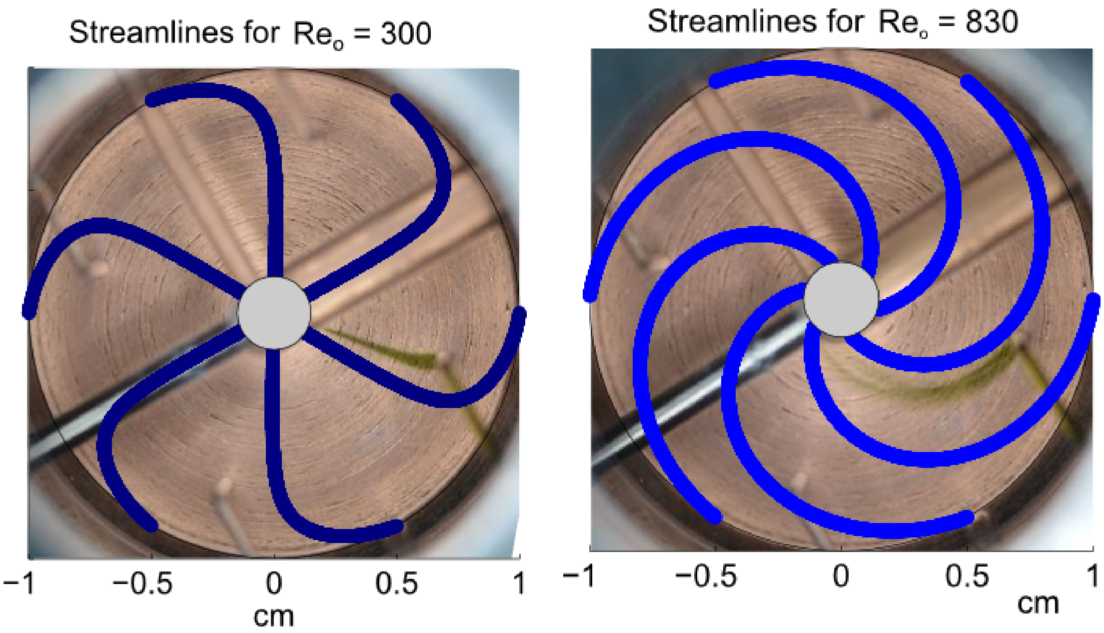

(a) (b)

Figure 5.4: Comparison of flow visualization streaklines to modeled streamlines based on the analysis in Sec. 3.1

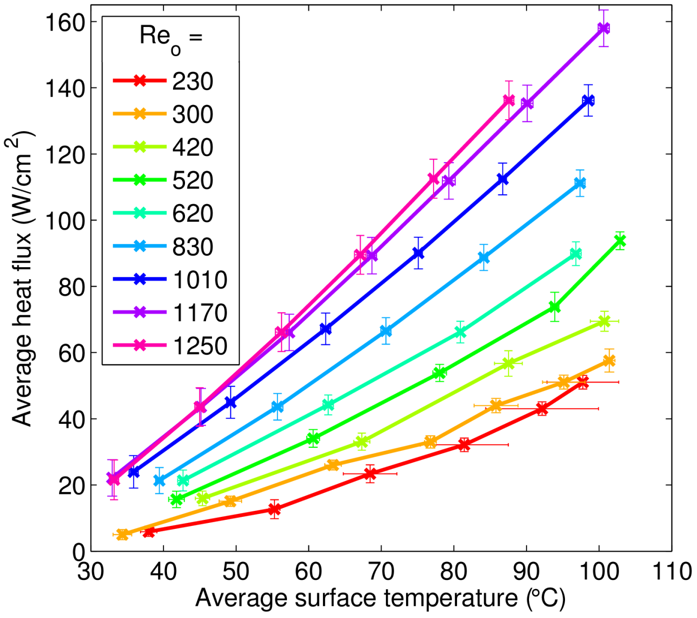

Figure 5.5: Average wall heat flux, q''_w, of the system for two devices over a range of flow rates tested

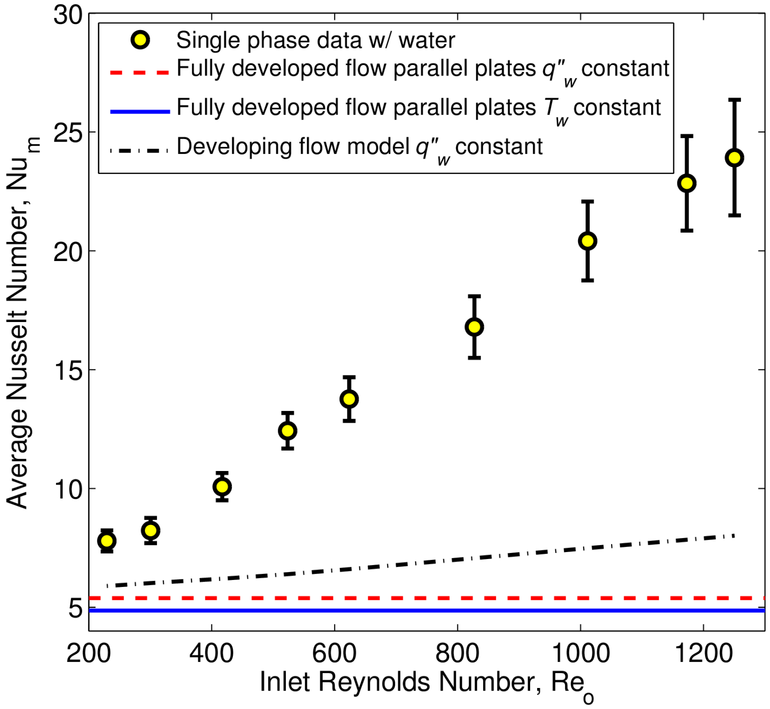

Figure 5.6: Average Nusselt numbers of the system for two devices over the range of flow rates tested. These values are compared to a developing flow estimate of Nusselt values for laminar flow between parallel plates with a constant wall heat flux at one wall. Also shown are the values for fully developed flow between parallel flat plates with one wall insulated and both a constant wall heat flux and a constant wall temperature condition.

5.3 Heat Transfer Characteristics

Figure 5.5 shows the average wall heat flux plotted against the average surface temperature for experiments done over a range of flow rates and heat inputs. The average wall heat flux, $\bar{q}''_w$, and the average surface temperature, T_w, were calculated using Eqs. (4.3) and (4.4), respectively. Each point corresponds to the average of four points with the same flow rate and same heat input but with different inlet orientations as shown in Fig. 4.3. Flows with inlet Reynolds numbers of 830-1250, corresponding to rates of 256-387 ml/min, were tested on Device U and flows with inlet Reynolds numbers of 230-620, corresponding to rates of 71-193 ml/min, were tested on Device PC. Flow rates beyond an inlet Reynolds number of 1250 were not tested due to the limits on the capabilities of the experimental set up. As expected, higher flow rates provided cooler surfaces for the same heat flux. The highest recorded heat flux was 158 W/cm^2 at a surface temperature of 101°C. Figure 5.5 shows a linear surface temperature response to increased heat input for each given flow rate, corresponding to relatively constant heat transfer coefficients for each flow rate.

Heat transfer coefficient data was averaged over all the single phase flow data points tested for each flow rate and used to calculate an average Nusselt number, $\mathrm{Nu_m}$, as shown in Eq. (4.9). Figure 5.6 shows the Nusselt number for a variety of inlet Reynolds numbers, $\mathrm{Re_o}$. The highest average Nusselt numbers recorded were about 24. The heat transfer characteristics are superior to fully developed laminar flow in parallel plates for both constant wall heat flux and wall temperature conditions, values of $\mathrm{Nu} = 5.39$ and $\mathrm{Nu} = 4.86$, respectively. Figure 5.6 also shows a model of developing flow in the device using Nusselt number values for parallel plates in hydrodynamically and thermally developing laminar flow with a constant wall heat flux from [61]. This was correlated with dimensionless path length, s^*, values in the channel which were modeled using the local values within the channel as:

$$s^* = \frac{s}{d_h \mathrm{RePr}} \tag{5.2}$$

Where s is the length of flow along the predicted streamline within the device, and Re is the predicted Reynolds number at the corresponding radial location. The developing flow model still lies significantly below the data collected. The enhancement of the flow is predicted to be attributed to extra heat dissipation due to instabilities, turbulence and accelerating effects of the flow. The Nusselt number also increases significantly as the flow rate increases, corresponding to flow that is both increasingly more in the turbulent flow and developing flow regimes as the flow rate increases. Thus, a more detailed model which incorporates the accelerating effects of the radial inflow, the temperature effects on the fluid properties and the turbulent transitions at higher flow rates within the flow would be necessary to accurately model the full effects of the heat transfer in the device over this range of flow rates.

Enhancement due to buoyant forces are not expected in the system since the Grashof number for the flow is always small compared to the square of the Reynolds number. Additionally when heated, the largest expected Rayleigh numbers are far below the critical value for the formation of instabilities due to temperature gradients.

5.4 Nusselt Correlation

The Nusselt numbers for the flow increase slightly with heat addition, so a correlation for Nusselt number was proposed in terms of an average Reynolds number in the flow, where the Reynolds number used is an averaged value based on the estimated velocity field in the flow using a viscosity based on the mean temperature of the flow, $T_{b,m}$.

$$\mathrm{Re_{avg}} = \frac{\mu(T_{b,m})}{\pi(r_o^2 - r_i^2)\mu(T_o)} \int_{r_i}^{r_o} \int_0^{2\pi} \mathrm{Re}(r) r d\theta dr \tag{5.3}$$

A power law correlation was proposed of the form:

$$\mathrm{Nu} = A\mathrm{Re_{avg}^b} \tag{5.4}$$

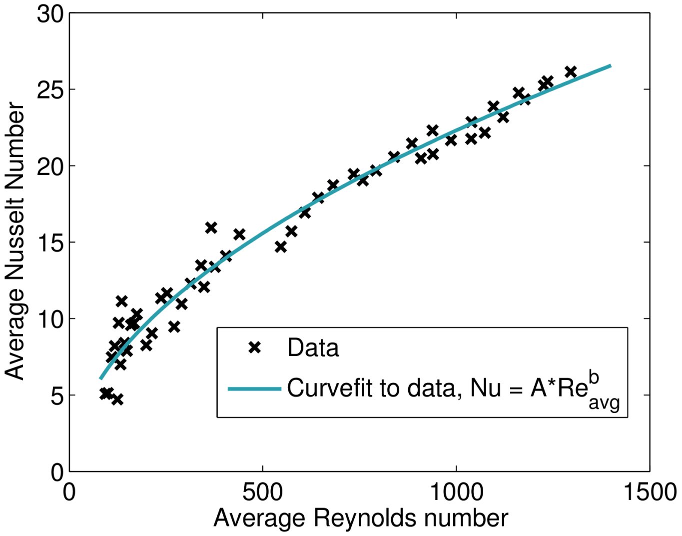

Figure 5.7: Curvefit for Nusselt number versus averaged Reynolds Number, with values of A = 0.62, b = 0.52 and an R^2 value of 0.97

Values of A = 0.62 and b = 0.52 were found with an R^2 value of 0.97. The data used to fit this correlation and the curve fit is shown in Fig. 5.7. This correlation can be used to solve for the single phase contribution to heat transfer in the device until a fully turbulent transition occurs.

5.5 Asymmetry Characterization

In order to assess the asymmetries and uniformity of temperatures on the heat sink surface, temperature measurements were taken at four inlet orientations relative to the thermocouple locations in the copper conducting piece. Figure 4.3 shows the thermocouple (TC) placement within the copper piece and the relative inlet orientations tested. Figure 5.8 shows the average surface temperature variation relative to the center surface temperature as a percentage of total fluid temperature gain across the system and linearly interpolated from the 13 TC locations. Here Θ_w is defined as:

$$\Theta_w = \frac{T_w - T_{w,center}}{T_{b,i} - T_{b,o}} \tag{5.5}$$

The value is averaged over all data collected for the single phase system. Figure 5.8 shows that the surface is cooler closest to the inlet region and along the path from the inlet to the outlet region. The hottest regions form far from the inlet flow, indicating there is likely not a uniform distribution of the flow throughout the device. However, the surface still stays relatively even in temperature since the total average gradient across the surface is about

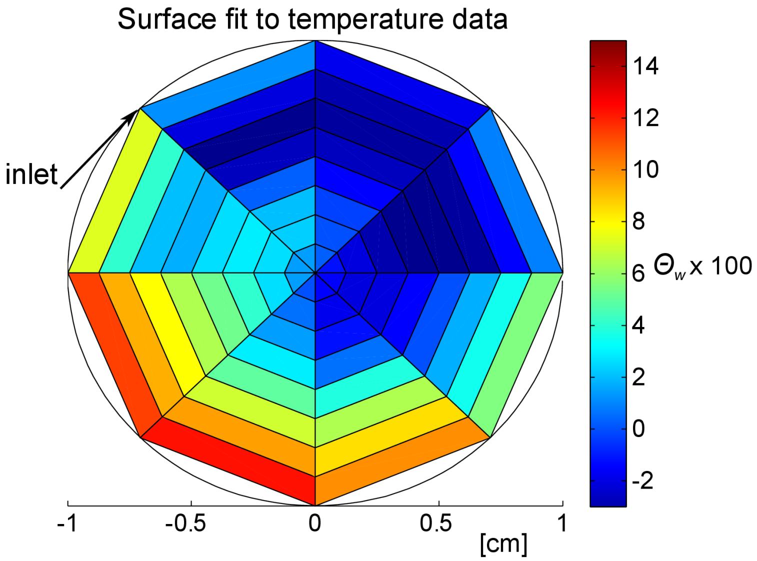

Figure 5.8: Percentage of temperature variations at the heated wall averaged over all tests relative to total fluid temperature gain across surface

18% of the total fluid temperature gain. It is expected that the total surface temperature would increase by as much as the fluid temperature if the wall heat flux and heat transfer coefficient were constant across the device.

The wall heat flux variations were calculated relative to the center wall heat flux at the three inner TC locations seen in Fig. 4.3. An average variation of about 19% relative to the center heat flux value across the surface was shown. The variations followed trends expected from the surface temperature distribution, high fluxes were found close to the inlet flow path and lower heat fluxes further from the inlet where cooling was not as effective. This means that neither a constant wall temperature nor a constant wall heat flux assumption is entirely accurate, but can still lead to appropriate analysis with only about 9-10% variation from the mean value of the data. Regions of high heat flux lead to lower predicted surface temperatures, increasing the last term of Eq. (4.4). However, because this term is relatively small (at most 5°C), the variation due to asymmetries would likely be small when compared to total bulk liquid temperature rise.

5.6 Discussion

The ability of this device to provide both high flux cooling at low and uniform wall temperatures has been shown. One specific data point of interest is at a volumetric flow rate of 387 ml/min ($\mathrm{Re_o}$= 1250) with an average heat flux of 113 W/cm^2, average surface temperature of 77°C and a ratio of work to heat, $\dot{\mathcal{W}}/\dot{Q}$, of 2.92×10^{-4}. Comparison to literature values for other single phase microchannel high heat flux cooling devices, from a review by Agostini et al.[2], show that the ratio of pumping power to heat rate for this device,

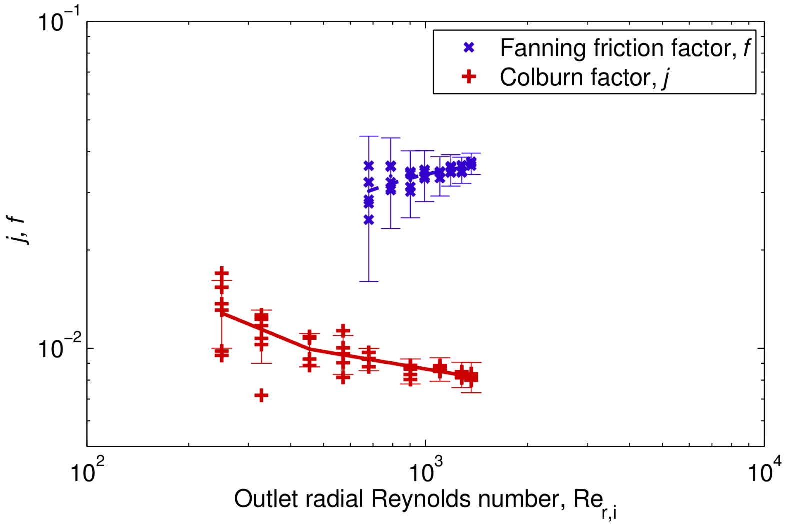

Figure 5.9: Experimental values for the friction factors based on pressure drop tests at room temperature, as well as colburn factors based on heat transfer tests over a range of heat and flow rates

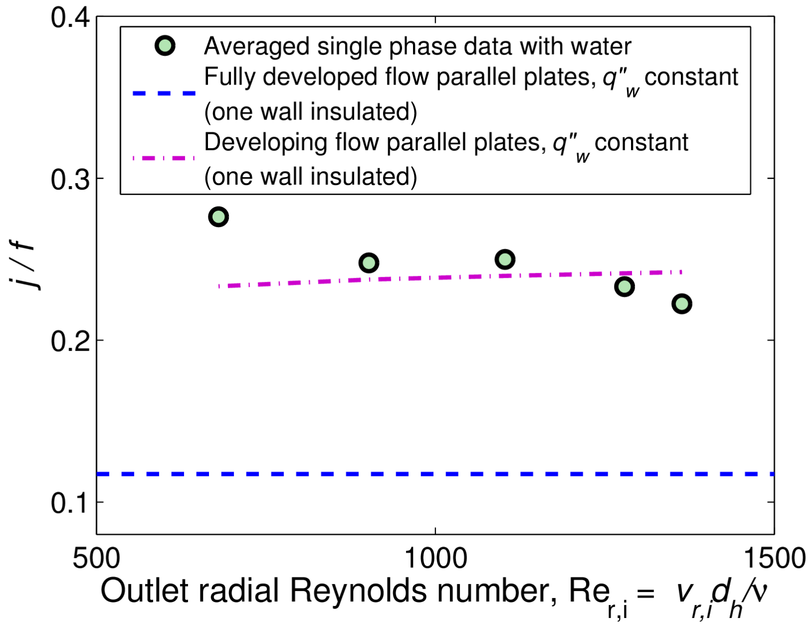

Figure 5.10: Average goodness factors, j/f, averaged over all tests for each flow rate plotted against the outlet radial Reynolds number, $\mathrm{Re}_{\mathrm{r,i}}$, defined as $v_{r,i}d_h/\nu$, and compared with developing flow and fully developed flow solutions for parallel plates under constant heat flux from one wall

operating at a surface temperature below 85°C, is an order of magnitude lower than most of the devices listed; however, the heat rate is only about one quarter of the highest rate shown. The thermal resistance, calculated using $1/\bar{h}$, at this operating condition is about 0.4 K cm^2/W. This value is higher than the average device listed in [2] at 0.18 K cm^2/W. Decreasing the gap size would likely decrease the resistance to comparable levels, although at an increased pumping cost.

Another metric often used to evaluate heat exchanger surfaces is the ratio of the Colburn factor to friction factor, or the 'goodness factor', written as j/f. Where

$$j = \frac{\text{Nu}}{\text{Re}_{\text{r,i}}\text{Pr}^{1/3}} \tag{5.6}$$

and an apparent friction factor, f, was found for the device using a normalized total pressure drop across the channel as:

$$f = \frac{\Delta P_f d_h}{2 s \rho \bar{v}_{r,i}^2} \tag{5.7}$$

Here, the mean outlet radial velocity at r_i is used as the characteristic velocity, since the flux at the minimum flow area is often used in literature [62]. In Eq. (5.7), the modeled flow path length, s, is used as the characteristic length. The pressure drop, ΔP_f, is the measured pressure drop in the channel due to friction losses in the system. Thus, the modeled entrance and exit effects, as well as the dynamic pressure changes through the system, are subtracted from the total measured pressure drop. Figure 5.9 shows the values of the friction factor, f, using the data for ΔP at room temperature seen in Fig. 5.1, and plotted against the Reynolds number based on $\bar{v}_{r,i}$ and d_h. Values below $\text{Re}_{r,i} = 600$ were not shown because the error in the friction factor was in in excess of 100%. This data shows the friction factor increases as the Reynolds number increases. This is indicative of flow in a transition region from laminar to unsteady turbulent flow, as is the expected flow regime shown from flow visualization tests. Also plotted are values of j for all the heat and flow rates tested from data seen in Fig. 5.5. Each value for j has properties calculated at the mean fluid temperature, $T_m = (T_o + T_i)/2$. The Colburn factor values decrease as the Reynolds number increases. While the flow is expected to be in a transition region here, the increased heat transfer due to developing flow at lower Reynolds number competes with the effect of a drastic increase in heat transfer in a transition region. In other words, the Nusselt number does not increase faster than the Reynolds number. The errors in Fig. 5.9 are shown for the average values of j and f.

Figure 5.10 shows the goodness factor, j/f, for the device, which was calculated using averaged values over the whole range of heat rates for each flow rate in excess of $\text{Re}_{r,i} = 600$. Also shown is a model for the apparent goodness factor, based on developing laminar flow between parallel plates with a constant wall heat flux and one insulated wall. The model used the same flow path length, s, hydraulic diameter, d_h, and Reynolds number as the radial inflow device to correlate an apparent friction and Colburn factors from data shown in [61], [63]. The experimental values are comparable to the expected value for developing flow in parallel plates with one insulated wall and one wall with a constant heat flux, showing enhancements from fully developed parallel plate flow.

Chapter 6

Two Phase Experimental Results

Boiling heat transfer experiments enabled two phase flow characterization of the spiraling radial inflow microchannel heat sink for heat rates up to 300 W/cm^2 using distilled water as a working fluid. Pressure drop and heat transfer data were acquired for a range of mass flow rates, heat rates and subcooling levels. Values of the mean mass flux rates, inlet temperatures and maximum wall heat flux levels are shown in Tab. 6.1. The mean mass flux rate value used throughout this chapter is found from a flow length averaged mass flux rate through the channel:

$$G_m = \frac{1}{r_o - r_i} \int_{r_i}^{r_o} G(r) dr \tag{6.1}$$

Flow images were acquired for a variety of flow conditions in order to help characterize the modes of heat transfer and identify distinct regimes of boiling heat transfer. Boiling experiments in the device revealed that, beyond the single phase flow regime, the flow throughout the entirety of the device could be characterized into one of three regimes: partial subcooled flow boiling(PSFB), oscillatory flow boiling(OFB), and fully developed flow boiling(FDFB).

Table 6.1: Range of mean mass flux rates, G_m, and corresponding inlet temperatures and max heat flux levels tested

G_m [kg/m^{2}s]	T_o [°C]	q''_{max} [W/cm^2]
184	22, 45, 60, 79	169, 150, 150, 150
255	20, 45, 60, 70	213, 195, 193, 193
320	21, 45, 59	236, 240, 236
381	21, 45	265, 235
442	21, 45	277, 259
505	22, 45	295, 291
618	21	301
716	21	293

Pressure drop, heat transfer and flow characteristics in each of these regimes are distinct and described in each section of this chapter, accordingly.

6.1 Flow Regime Characterization

For each combination of heat rate, flow rate and subcooling level tested, the entirety of the device tended to adhere to similar flow boiling characteristics. Thus, for each set of conditions recorded, the flow through the heat sink is characterized as falling into one of the following three regimes.

Partial subcooled flow boiling

In the partial subcooled flow boiling (PSFB) regime, heat transfer into the fluid is arises from a combination of both forced convective and nucleate boiling effects. The onset of this regime is characterized by the onset of nucleate boiling, resulting in an increased heat transfer coefficient relative to single phase flow. Sparse bubbly regions are seen on the surface and in the bulk of the flow. These bubbles can quickly grow to the height of the channel and draw other bubbles towards the exit, but do not restrict the flow. At the outlet, the flow in this regime is always expected to be subcooled. However, it is observed from flow images and videos that bubbles are seen at the outlet. This is likely due to dynamic or buoyant forces dragging vapor bubbles into the bulk flow and to the outlet. This vapor will quickly condense downstream. Because of the large contribution due to forced convective effects, tests with lower subcooling levels had higher wall temperatures for a given heat rate. However, the lower subcooling levels corresponded generally to higher heat transfer coefficients as nucleate boiling effects increase with more vapor generation at the surface. For the highest flow rates tested, the flow throughout the device never transitioned beyond the PSFB regime due to high levels of subcooling and low levels of vaporization on the surface.

Oscillatory flow boiling

Oscillatory flow boiling (OFB) is characterized by large oscillations in both surface temperature and pressure drop across the channel. The oscillatory behavior is likely due to bubble constriction and obstruction of the flow. Previous studies have shown that flow constriction due to vapor generation is generally due to compressibility upstream of the channel, which allows for backflow when vapor grows rapidly in the channel [1]. Future design constraints should be established to avoid this from occurring. Heavily throttling the flow upstream is suggested, however, this can likely lead to large pressure penalties associated with the flow.

In this regime, flow alternates between PSFB and FDFB. As the surface temperature rises, wall superheat will initiate larger regions of nucleate boiling. This will tend to cause

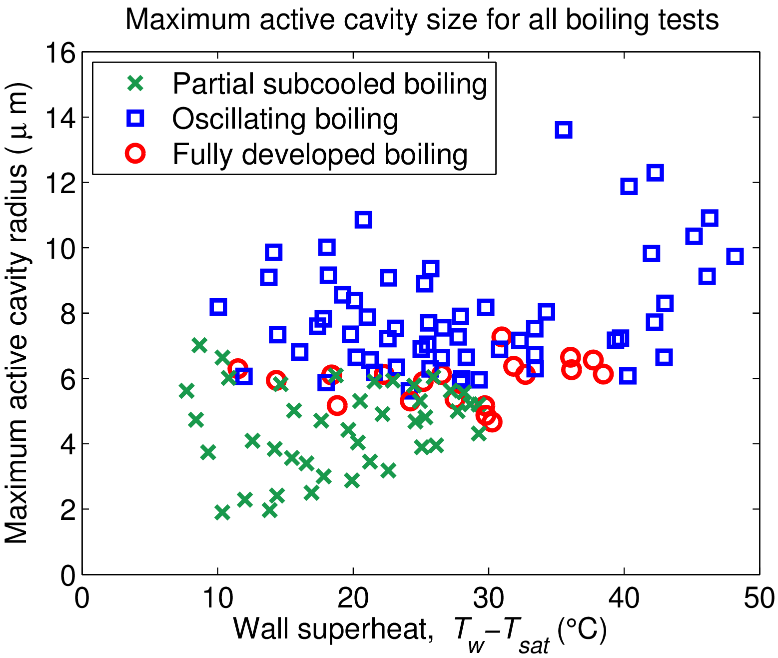

Figure 6.1: Active cavity radii versus wall superheat over all flow rates and heat rates tested, identifying the boiling regimes for the data

large bubbles to grow in the channel, constricting the flow, and result in pressure build-up. Because of the use of microchannels on the order of 300 μm, it can be expected the growth of a bubble can rapidly result in this type of constriction. Once enough pressure builds up behind a bubble, it will be dragged out of the way and subcooled liquid rushes in, causing the surface temperature to drop. This cooling effect temporarily suppresses further nucleation. The surface will then heat back up and continue this sequence in an oscillatory way, alternating between forced convective dominated heat transfer and nucleate boiling dominated heat transfer. If vapor constriction and pressure oscillations significantly decrease the flow rate it may lead to early onset of critical heat flux. Because of the nature of the design, however, the tangential distribution of the fluid can tend to suppress the likelihood of dryout occurring on any one specific region. The spiraling flow allows the flow to fully spread over the channel and increase the likelihood of bubble entrainment along the flow path. This enhancement is less likely to occur in parallel microchannel systems where a bubble might restrict flow to one channel and all flow is diverted to another channel. For OFB, a decrease in subcooling levels tends to decrease the level of oscillation because of less aggressive nucleation suppression. The average exit quality in this regime is occasionally nonzero, but not necessarily. More details on the oscillatory behavior of the system are discussed in Sec. 6.7.

An analysis on the range of active cavity radii reveals that oscillatory flow occurs when larger cavity sites become active. Figure shows the maximum active cavity radius based on Hsu's analysis shown in Sec. 3.2, and using properties at the outlet temperature of the system, where the first nucleation sites are predicted to occur.

Fully developed subcooled flow boiling

Fully developed flow boiling (FDFB) is characterized by vapor rapidly leaving the surface. Thus, large fluctuations in pressure and temperature are not sustained, but small and rapid fluctuations of temperature and pressure occur as vapor is continuously driven through the exit. Bubbly flow is seen throughout the channel with coalescing of bubbles into larger slugs of vapor. This regime was always characterized by a nonzero average exit quality. In this regime, decreased subcooling levels resulted in reduced wall superheat for the same heat rate, likely indicating large contributions of nucleate boiling or evaporative heat transfer and corresponding to increased exit quality.

The generation of large vapor slugs in FDFB, OFB, and occasionally in PSFB may result in annular flow through the channel, where one large bubble fills the majority of the cross-section of the channel and a thin film of liquid evaporates on the surface. This mechanism would result in high heat transfer coefficients due to evaporative rather than nucleate boiling heat transfer driving the cooling of the surface. Evidence for this is seen in the fact that large regions of vapor are present in images of boiling, seen in Sec. 6.6 yet the surface temperatures indicate dryout cannot be occurring over these large regions. However, these regions of annular flow may be the mechanism for initial dryout in the channel, where the wetted surface evaporates into a bubble and dries out the surface.

Flow Regime Maps

A flow regime map which is dependent on important nondimensional parameters of the flow can help to indicate the type of flow regime that is expected to occur in a spiraling radial inflow device. Figure 6.2 indicates the flow regimes dependent on the exit quality or subcooling level versus the Jakob number. The Jakob Number, Ja, is indicative of the ratio of sensible heat of the fluid through the total temperature gradient in the system to the latent heat of the fluid is defined as

$$\mathrm{Ja} = \frac{\rho_l}{\rho_v}\frac{c_{p,l}(T_w - T_{b,l})}{h_{lv}} \tag{6.2}$$

this nondimensional value is chosen because it tends separate the oscillation regime from the other boiling regimes due to its dependence on the temperature gradient from the surface to bulk fluid temperature. This is plotted relative to the exit quality, x_e, or the nondimensionalized subcooling level, $\Theta_{sub,e}$, defined as:

$$\Theta_{sub,e} = \frac{T_{l,e} - T_{sat}}{h_{lv}/c_{p,l}} \tag{6.3}$$

which indicates the level of subcooling or level of vapor fraction present in the channel.

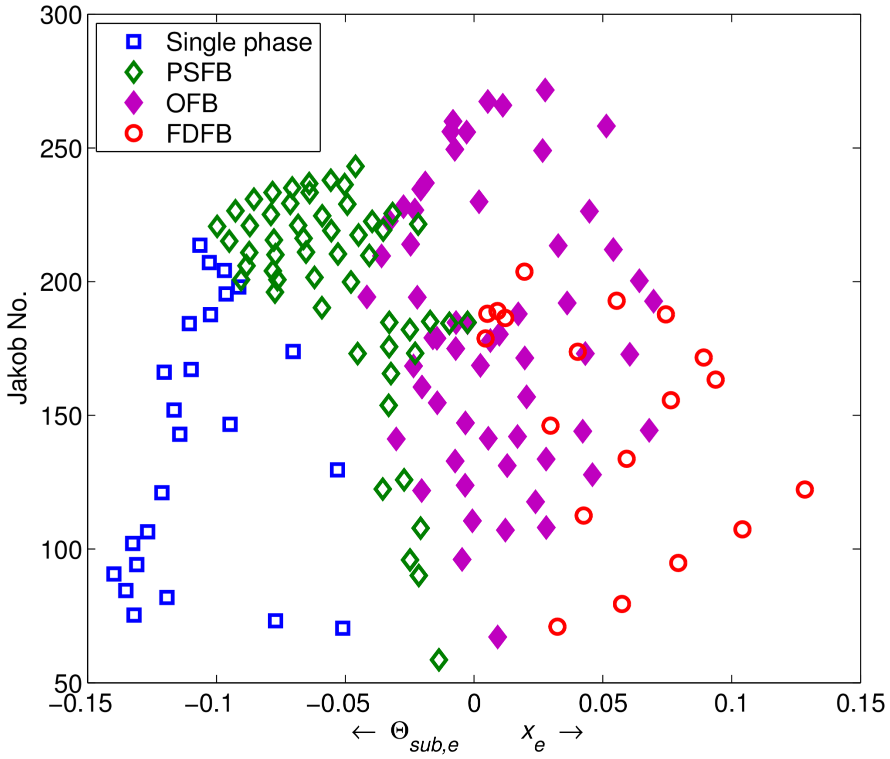

Figure 6.2: Flow regime map for all data showing the level of exit quality or subcooling versus the Jakob number

The map in Fig. 6.2 shows, that once beyond the single phase flow regime, flows with high subcooling levels and high Jakob numbers will be in the partial subcooled flow boiling regime. Once the exit temperature is very close to saturation or the exit vapor quality, x_e, becomes positive, oscillatory flow boiling is seen. At higher Jakob numbers there tends to be more oscillatory data points because of the larger temperature gradients from the bulk fluid to surface that can lead to explosive and unsteady vaporization. For low Jakob numbers and higher quality levels, fully developed boiling is seen to occur, indicating more sustained yet steady vaporization of the flow. It would be of interest to analyze how this flow regime map compares to similar devices with similar geometry to indicate the validity of the nondimensional aspect; however, currently no data exists.

6.2 Heat Transfer Characteristics

Boiling curves for low, mid, and high-range flow rates and varying fluid subcooled levels are shown in Figs. 6.3, 6.4, and 6.5. Corresponding heat transfer coefficients are shown in

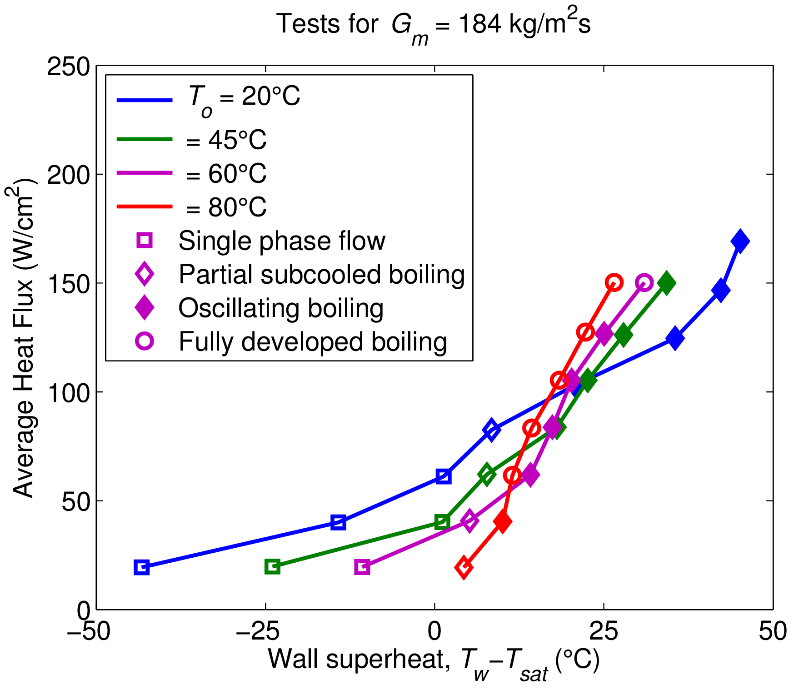

Figure 6.3: Boiling curve at a mean mass flux $G_m = 184$ kg/m^{2}s for four different subcooling levels

Figs. 6.6, 6.7 and 6.8. The full range of test flow rates and subcooling levels is shown in Table 6.1. The full data set for all tests is shown in Appendix F. For all boiling tests, outlet saturation temperatures varied between 100 to 112°C based on outlet pressure measurements. Each point on the boiling curves is averaged over the four orientations tested. The flow regime for each averaged data point is identified as follows: the system is said to be in the oscillatory flow regime if 2 or more of the tests at a specified heat rate showed temperature fluctuations greater than 5°C. Fully developed boiling is marked as a nonzero exit quality data point that is not in OFB. Onset of nucleate boiling is identified as an increase in the slope of the heat flux versus wall superheat and corresponding increase in the heat transfer coefficient. This value typically occurs once the average superheat is beyond about 4°C.

For the lowest mass flow rate, Fig. 6.3 shows that, as surface temperature levels increased beyond the onset of nucleate boiling, the system quickly, often immediately, entered the OFB regime, and an increase in wall surface temperatures is observed. Lower Weber and Bond numbers associated with lower flow rates and lower outlet subcooling levels can lead to larger bubbles in the channel because of reduced drag and buoyant forces dragging the bubbles into the flow. This can cause more flow constriction and oscillatory behavior. Beyond this the flow stabilizes into fully developed flow boiling. For subcooling levels of 55°C and below, it was difficult to maintain heat flux rates beyond 150 W/cm^2 without significant jumps in temperature, indicating lower critical heat flux levels. For lower levels of subcooling,

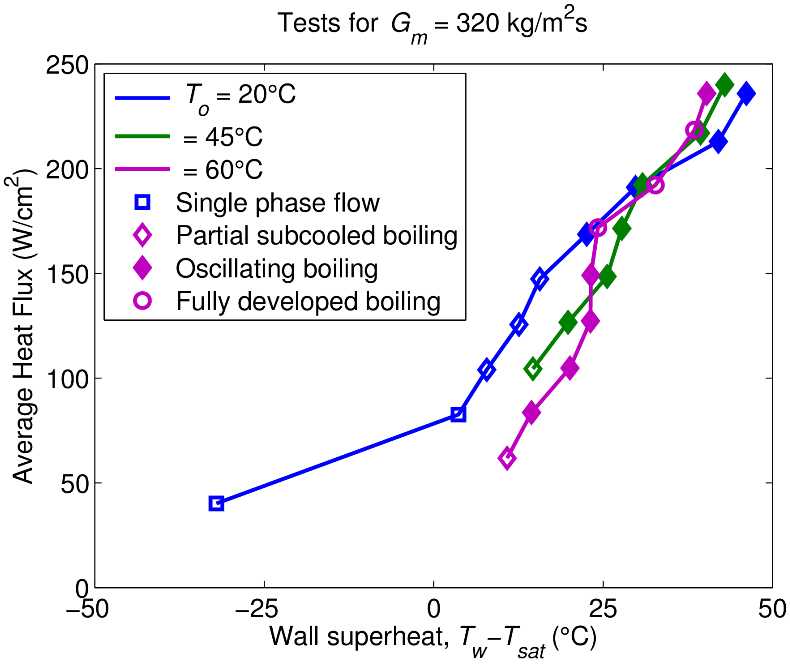

Figure 6.4: Boiling curve at a mean mass flux $G_m = 320$ kg/m^{2}s for three different subcooling levels

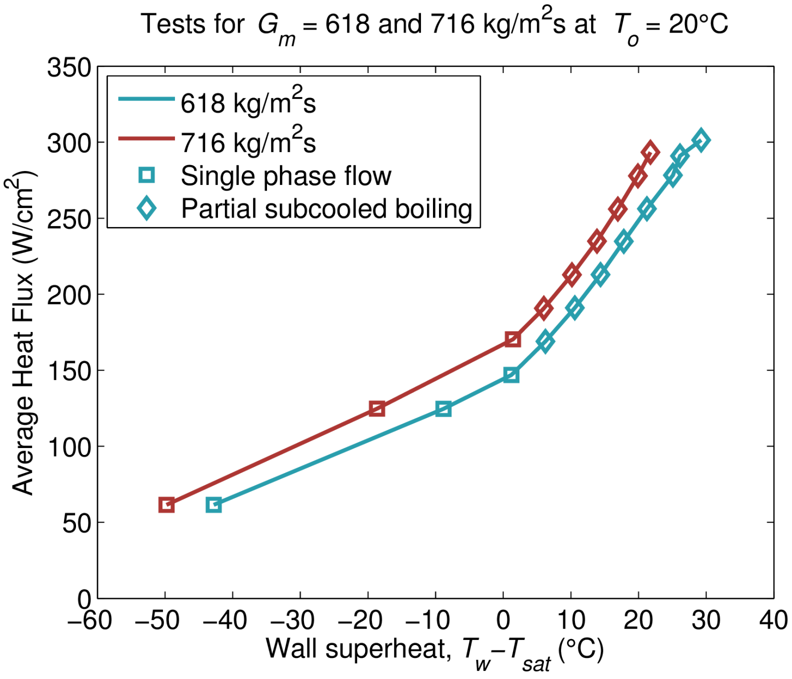

Figure 6.5: Boiling curve at mean mass fluxes G_m = 618 and 716 kg/m^{2}s

nucleate boiling or evaporation is the dominant method of heat transport and higher heat transfer coefficients are seen in Fig. 6.6. Additionally, the heat transfer coefficient levels out as nucleate boiling contributions reach a maximum.

For midrange mass fluxes, similar enhancements due to low flow rates were seen. Fig. 6.4 shows the boiling curve and Fig. 6.7 shows the heat transfer coefficients for a flow rate of 320 kg/m^{2}s. The main difference is that the heat transfer coefficients did not increase as rapidly, although higher values of heat transfer coefficients and heat fluxes were seen, with values up to 6.5 W/cm^{2}K. Heat transfer coefficients were highest when boiling or vaporization contributions were largest in FDFB. Lower subcooling levels still outperformed the higher levels.

Fig. 6.5 shows the boiling curves for two highest mass flux levels tested. For the highest flow rates, large subcooling levels prevented the development of oscillatory or fully developed boiling. The boiling curve followed the trends of a typical boiling curve leveling off slightly near the highest flux levels of 300 W/cm^2. This value was the experimental limit, but it is expected that critical heat flux levels are beyond this rate due to the low surface temperatures and the stability of the flow at these flux rates. Fig. 6.8 shows that heat transfer coefficients steadily increased as nucleate boiling contributions became larger, but the highest values were not seen at these highest flow rates, rather at the midrange flow rates subject to larger nucleate boiling or evaporation contributions in FDFB.

A model of partial subcooled boiling heat transfer is discussed in Sec. 3.2 and seen in Eq. (3.70). This model accounts for the enhanced single phase forced convective effects in a spiraling radial inflow based on Nusselt number correlations from Sec. 3.1. The expected heat flux is calculated based upon the experimental wall superheat. A comparison of the values predicted from this model to the experimental values for tests at $T_o = 20$°C are seen in Fig. 6.9. Three key features can be seen in this comparison. First, at the onset of boiling, or at the lowest heat flux levels, the model tends to underpredict the total heat flux, indicating there may be additional enhancements in the system beyond single phase forced convective effects in this regime. Second, as the heat flux increases, the model tends to overpredict the total heat flux, indicating that the model does not accurately predict a transition into departure from nucleate boiling which typically occurs at higher flux levels on boiling curves. The total mean absolute errors during all partial subcooled flow boiling for this data is 24%. Finally, Fig. 6.9 shows that as the flow enters the oscillatory flow boiling regime, the curves diverge significantly from the model predicted values indicating very large inaccuracies in the predictions. An example of a comparison of the model and experimental boiling curves is shown in Fig. 6.10 for the two highest mass flux levels. Thus, the model reveals relatively accurate predictions for the partial subcooled flow boiling regime which is typical at higher mass flux levels.

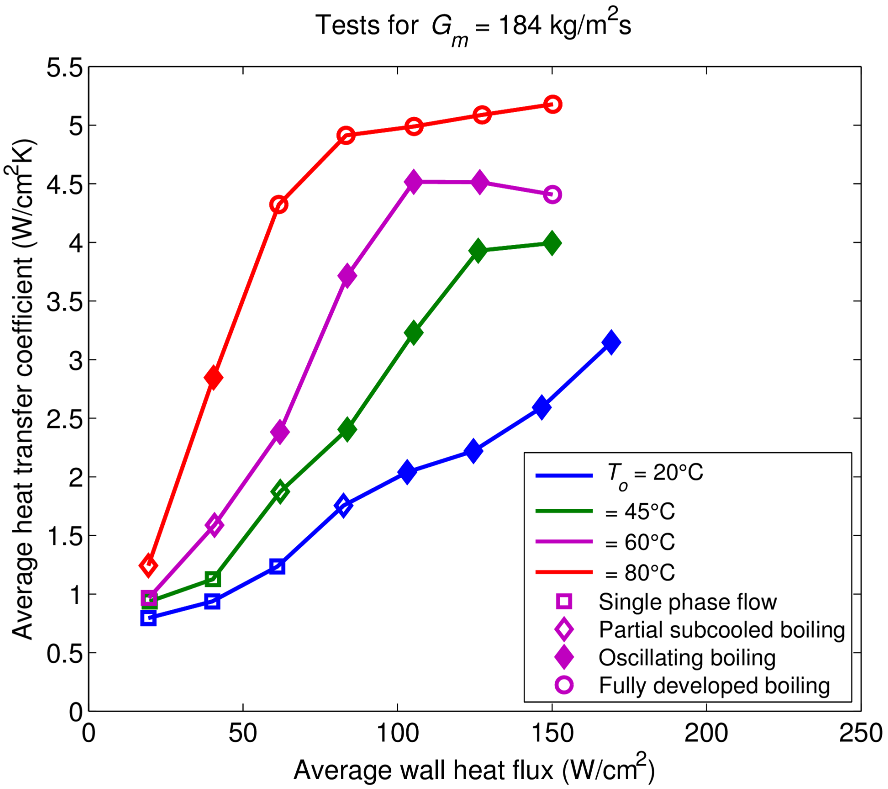

Figure 6.6: Heat transfer coefficients for a mean mass flux $G_m = 184$ kg/m^{2}s for four different subcooling levels

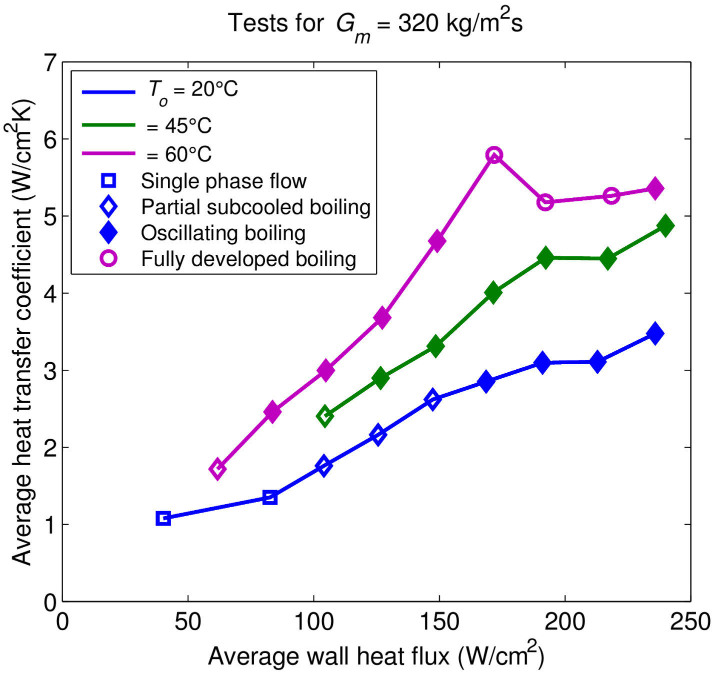

Figure 6.7: Heat transfer coefficients for a mean mass flux $G_m = 320$ kg/m^{2}s for three different subcooling levels

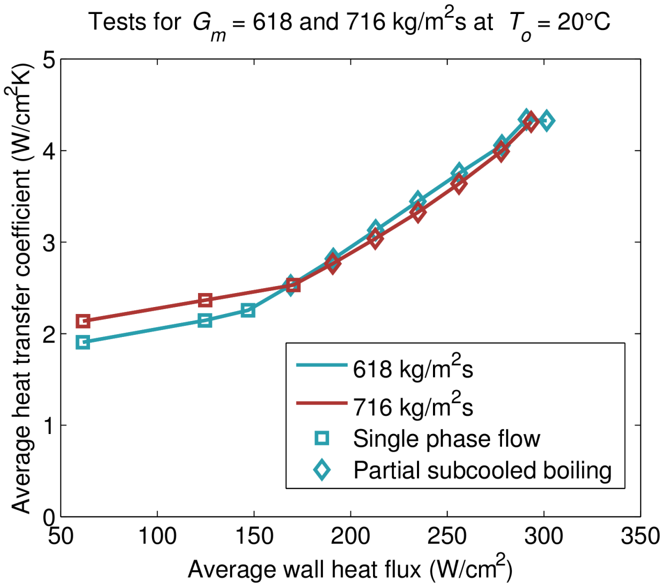

Figure 6.8: Heat transfer coefficients for mean mass fluxes $G_m = 618$ and 716 kg/m^{2}s

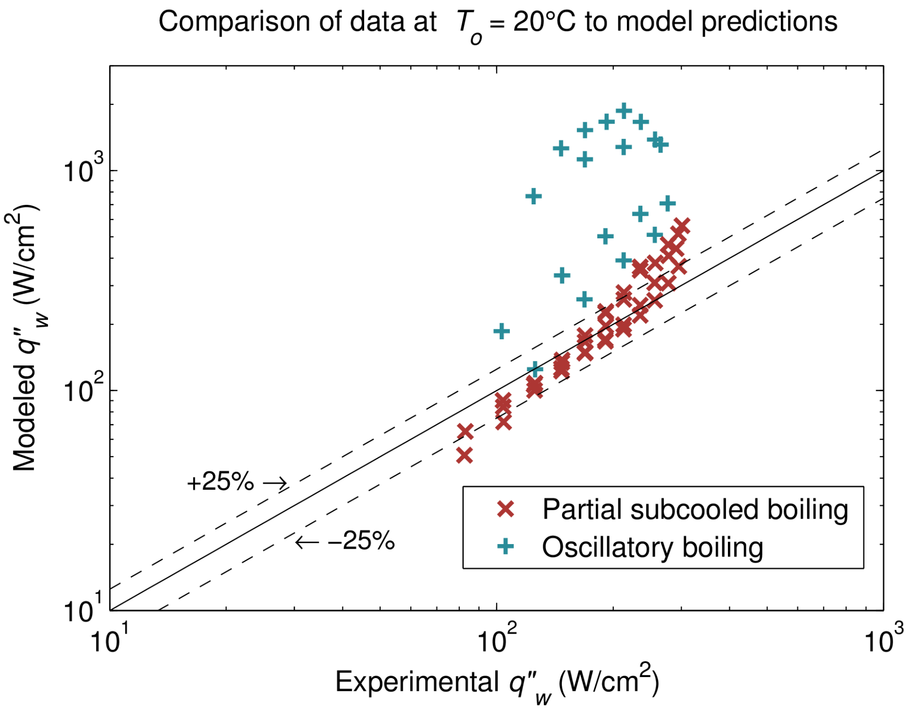

Figure 6.9: Comparison of the Rohsenow partial subcooled boiling model [58] with experimental data for tests done at $T_o = 20°\mathrm{C}$

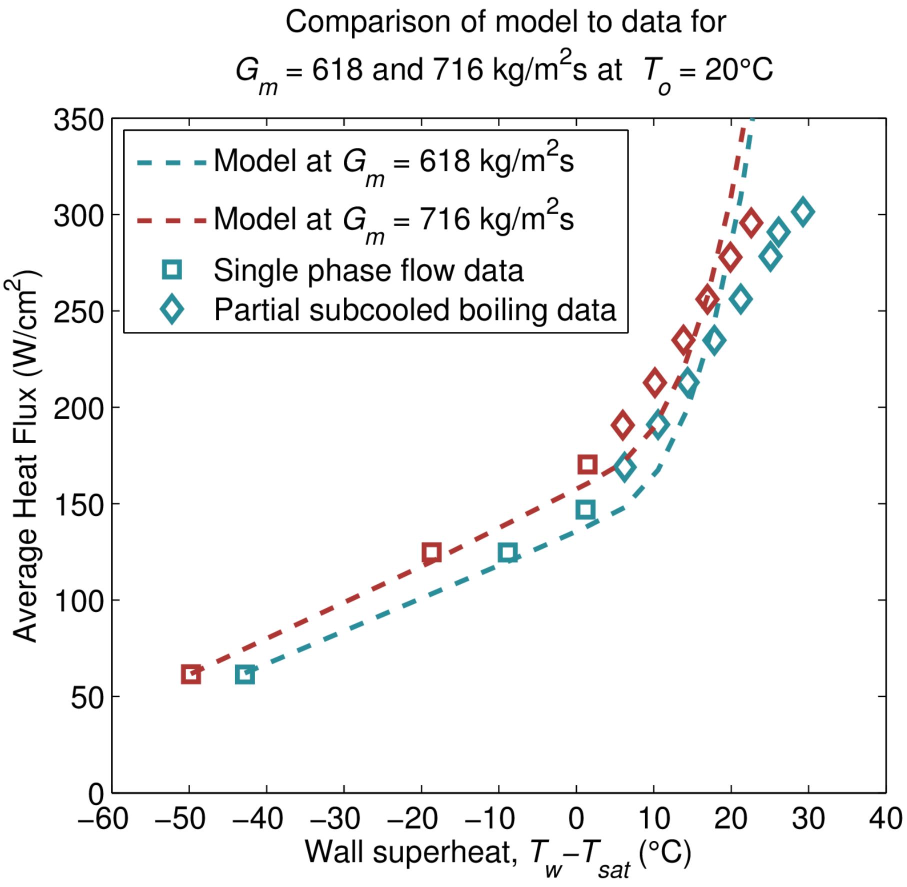

Figure 6.10: Boiling curve for the two highest mean mass flux rates and using the model proposed by Rohsenow [58] seen in Eq. (3.70)

6.3 Critical Heat Flux

The maximum heat flux levels shown in the boiling curves and listed in table 6.1, are the peak heat flux levels reached for tests at least two different orientations. The tests were not recorded if either the surfaces temperature steadily and rapidly increased, indicating thermal runaway or dryout, or if the surface temperatures reached higher then around 175°C and were considered unstable for the test set up. Otherwise the heat was increased at increments of about 21 W/cm^2 until the maximum experimental limit was reached, around 300 W/cm^2. At the highest flow rates, the peak heat flux values were very stable and had relatively low surface temperatures, so it is likely that the critical heat flux at these rates are higher.

Bergles and Kandlikar [64] have discussed the nature of critical heat flux in microchannels, stating that most data for critical heat flux values in the literature are a result of instabilities. Thus, models do not predict the real level of critical heat flux for microchannels. The current system is also subject to instabilities during flow boiling. In order to understand the general trends, however, the peak heat flux levels measured were compared to models of critical heat flux in both regular and microchannels. Figure 6.11 shows a comparison of these peak flux values to three models. The critical heat flux is represented in dimensionless form as the maximum boiling number of the flow, defined as:

$$\mathrm{Bo}_{\mathrm{max}} = \frac{q''_{max}}{Gh_{lv}} \tag{6.4}$$

The first model is a model for critical heat flux values for pool boiling based on a study by Zuber, from [65]. The critical heat flux for this model is found from:

$$q''_{max,Zuber} = 0.149\rho_v h_{lv}\left(\frac{\sigma(\rho_l-\rho_v)g}{\rho_v^2}\right)^{1/4} \tag{6.5}$$

This general trend holds for the two phase flow, but underpredicts the data by as much as 55% (with a mean absolute error of 36%). The second model comparison is a model for subcooled flow boiling in regular channels from Celata et al.[66]. The critical heat flux for this model is found from:

$$q''_{max,sub} = \frac{Gh_{lv}C_c}{Re^{0.5}} \tag{6.6}$$

Where:

$$C_c = (0.216 + 0.474P/10)\Psi \tag{6.7}$$

$$\Psi = \begin{cases} 1 & \text{for } x_e < -0.1 \\ 0.825 + 0.986x_e & \text{for } 0 > x_e < -0.1 \end{cases} \tag{6.8}$$

Where P is in bar and x_e is the level of subcooling at the flow exit. Although, the diameter and subcooling levels are outside the “range of applicability” for this model, the general trend still follows, but always showing much lower values than the experimental system.

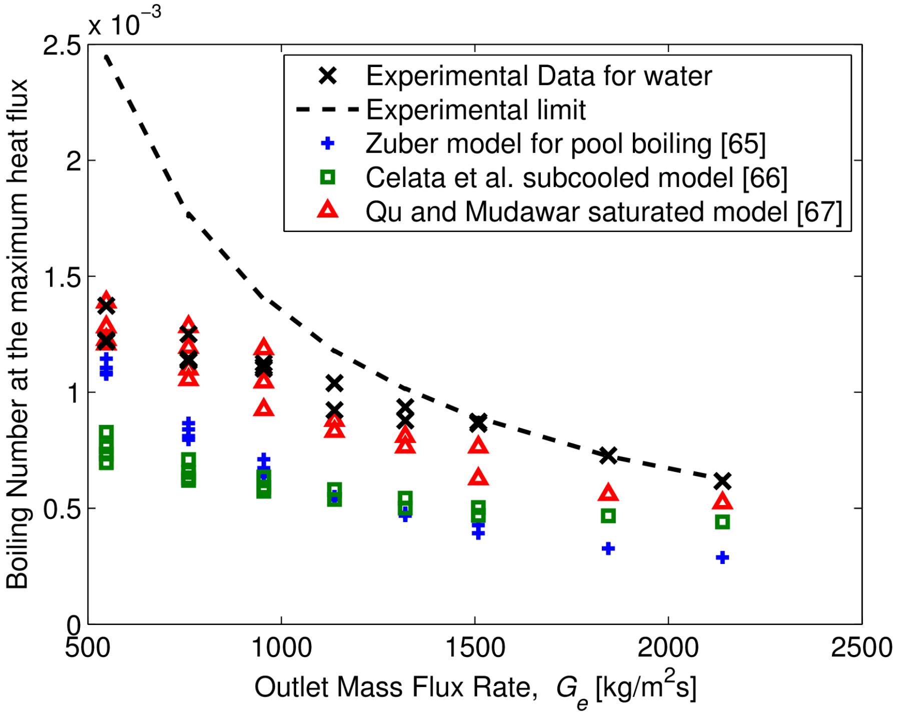

Figure 6.11: Experimental maximum heat flux rates tested compared to critical heat flux models

The mean absolute error for this model is 42%, underpredicting by as much as 48%. The last correlation shown in Fig.6.11, is the saturated flow boiling correlation proposed by Qu and Mudawar [67] for flow boiling of water and R113 in microchannels which was derived from correlations of Katto and Ohno.

$$q''_{max,sat} = 33.43 G h_{lv} \left(\frac{\rho_v}{\rho_l}\right)^{1.11} \mathrm{We_L}^{-0.21} \left(\frac{L}{d_h}\right)^{-0.36} \tag{6.9}$$

Where Weber number here is based on the flow length of the passage, L, characterized here as the total path length for a specified flow rate in the single phase. This model generally underpredicts the critical heat flux by up to 28%, yet it provides the most accurate prediction with a mean absolute error of 11%. For the last two models the exit mass flux rate of the experimental device is used in order to compare to the experimental data. This would result in the highest possible prediction, but is indicative of the mass flux rate where the initial dryout may occur.

It is of interest to explore what design aspects could be adjusted to increase the CHF levels. From the data, it is clear that increasing the flow rate would result in higher possible flux levels due to larger forced convection heat transfer contributions and higher exit subcooling levels. This may be undesirable, because it could lead to higher pumping penalties

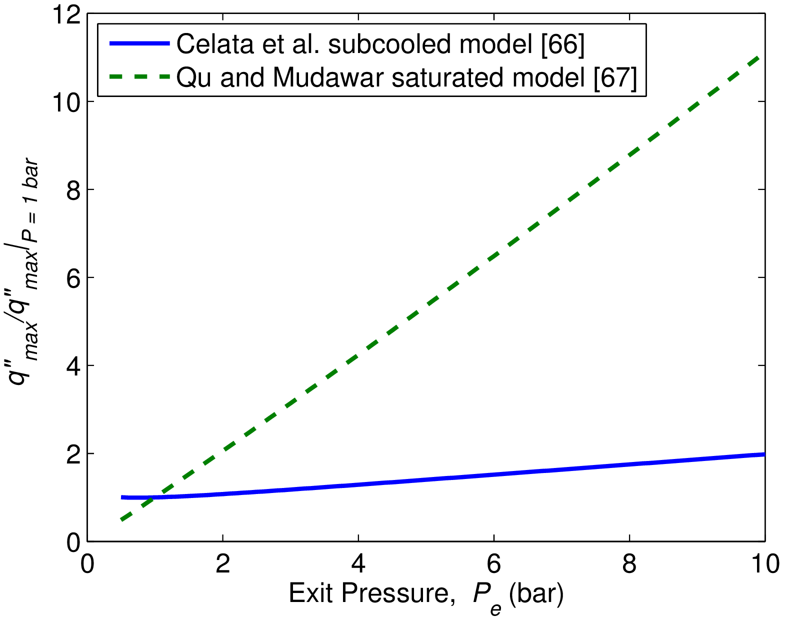

Figure 6.12: Effect of pressure variation on critical heat flux for two models, the value of the critical heat flux is shown relative to the model estimates at P = 1 bar

and reduced heat transfer coefficients. Increasing the pressure in the channel is also expected to increase critical heat flux levels. The increased density of vapor at higher pressures can lead to more stable vaporization, however, at a higher saturation temperature. Both critical heat flux models for flow boiling predict that increased channel pressure will result in higher critical heat flux values. Figure 6.12 shows how the models for critical heat flux increase with pressure, plotted relative to the model value for critical heat flux levels at 1 bar. For the model by Qu and Mudawar for saturated microchannel boiling, critical heat flux level enhancements are fairly large at increased pressure, with values at P = 10 bar at 11 times the value for P = 1 bar. This would indicate the highest values tested experimentally would be greater than 2500 W/cm^2 at an exit pressure of 10 bar. The Celata model for subcooled flow boiling model has less drastic critical heat flux enhancements at increased pressure. The critical heat flux value is modeled to increase up to 590 W/cm^2 at P = 10 bar and up to 440 W/cm^2 at P = 5.5 bar which is the recommended upper limit of validity for the Celata et al. model.

6.4 Pressure Drop Characteristics

The pressure difference across the channel was measured for all flow rates and heat rates tested. The measurements were averaged for about one minute, over each combination, so

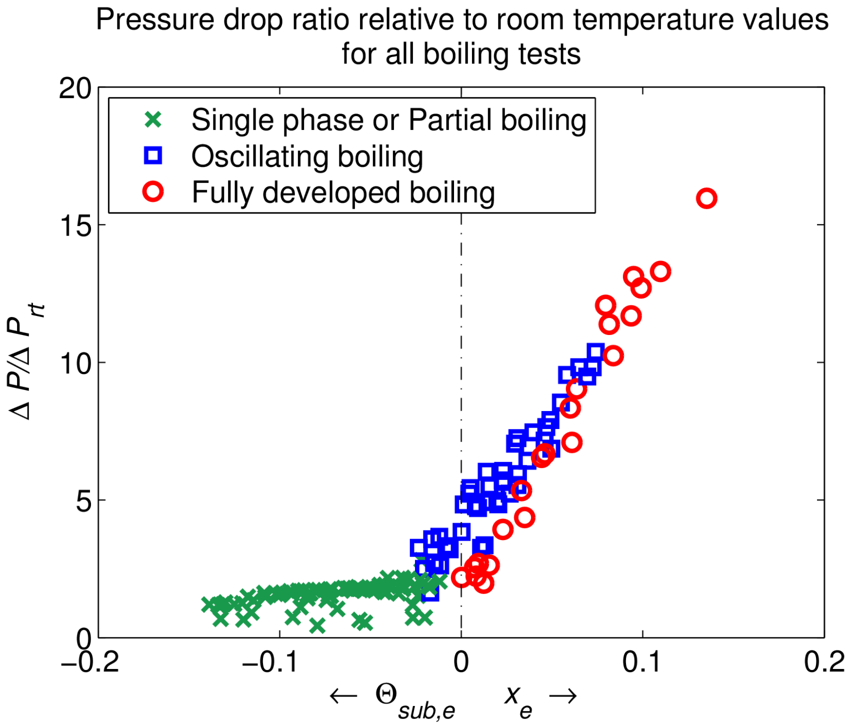

Figure 6.13: Pressure drop in the channel relative to the room temperature value at the same rate versus x_e or $\Theta_{sub,e}$ as defined in 6.3

oscillatory effects were averaged out. As the heat rate increased the pressure tended to generally increase. As the flow rate increased, the pressure drop increased which is expected for single phase flow. The data for all pressure drop tests averaged over four orientations are shown in App. F. For partial subcooled flow boiling, the pressure drop across the channel stayed relatively constant relative to the pressure measured at the same heat rate with no heat addition, although it did increase slightly with heat rate. Over this regime the pressure drop increased by an average of 84% and was at most 3.8 times larger than the pressure drop measured using no heat addition at room temperature. This demonstrated similar characteristics as for single phase flow implying the contributions of nucleation on the surface does not significantly affect the pressure drop in the channel. The oscillatory boiling and fully developed boiling regimes showed significant jumps in the pressure drop across the channel. On average, the pressure drop for oscillatory boiling is 4.9 times (and at most 12.1 times) larger than the pressure drop with no heat addition at room temperature. The pressure drop in the fully developed regime is on average 7.5 times (and at most 17 times) larger than the pressure drop with no heat addition at room temperature. Thus, increased exit quality seem to significantly affect the pressure drop in the channel, due to decreased density of the vapor causing rapid acceleration of the flow. A plot of all of the data of the pressure drop in the channel relative to the room temperature value at the same rate is shown in Fig. 6.13. The pressure drop is plotted against the exit quality, x_e or the nondimensionalized subcooling level, $\Theta_{sub,e}$, defined as in Eq. (6.3). This figure reveals the increased pressure drop due to increased vapor quality in the channel. It also reveals additional pressure drop effects due to the oscillating effects which aggressively disturb the flow.

6.5 Surface Temperature and Heat Flux Variations

The temperature and heat flux variations across the surface of the microchannel for all boiling tests was assessed in the same manner as discussed in Sec. 5.5. Figures 6.14 - 6.16 show the average fits for surface temperature variations relative to the center value for each flow regime and across three different subcooling ranges. The value is given in terms of a nondimensional temperature, Θ_w defined in Eq. (5.5), which represents the variation of the surface temperature relative to the total fluid temperature gain. Tables 6.2 and 6.3 show the total percentage variation across the surface for wall temperature based on Θ_w and heat flux.

Figure 6.14a shows average temperature variations for partial subcooled boiling at subcooling levels around 80°C, and revelas a relatively uniform surface temperature with total surface temperature variations at 12.6% of the bulk fluid temperature gain. Similar to single phase flow experiments, the lowest surface temperatures are found close to the inlet. This temperature distribution correlates well with the flow images, where bubbles are first seen to form in the lower left corner of the device. For subcooling of around 55°C and 20-40°C, Figs. 6.15a and 6.16a shows surface temperature variations up to 24.6 and 19.0%, respectively. With the highest surface temperatures at the outer region and the coolest at the center and close to the upper right from center, as is seen in single phase and for subcooling of 80°C. This indicates that the subcooled inlet fluid may be suppressing bubble growth in this region, while the majority of the surface has a relatively uniform surface temperature indicating more uniform vapor generation on the rest of the surface.

Figure 6.14b, 6.15b and 6.16b show average temperature variations for oscillatory flow boiling. For subcooling levels of 80°C, similar trends to partial subcooled boiling are seen although with cooler temperatures at the center of the device. This is likely caused by high heat transfer coefficients at the exit, where vapor is drawn towards the outlet in an oscillatory motion, resulting in turbulent convection. The regions of higher temperature may have higher tendency of vapor crowding with flow being diverted around the area. For subcooling of around 55°C and 20-40°C, the center, is again the coolest region, indicating high heat transfer coefficients in this region, and lower heat transfer coefficients around the edges near the feeder channel region, the opposite trend as the bulk fluid temperature variation. The total surface temperature variation is only up to 27% indicating relatively uniform surface temperatures when compared to what is expected from flow in a channel with a constant heat transfer coefficient.

Fully developed flow boiling surface temperature variations were shown for only the

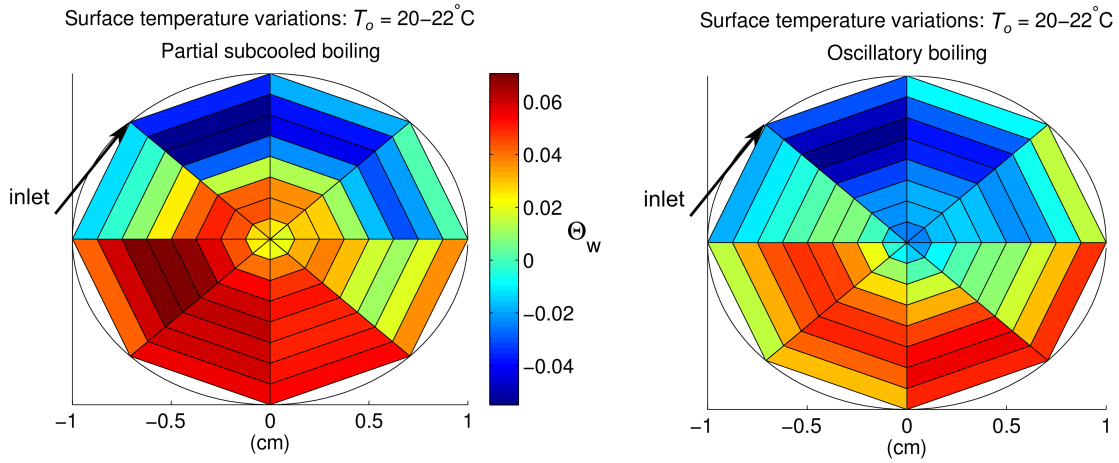

(a) (b)

Figure 6.14: Surface temperature variations for partial subcooled and oscillating boiling regimes with a inlet temperature of 20-22°C (Subcooling ∼ 80°C)

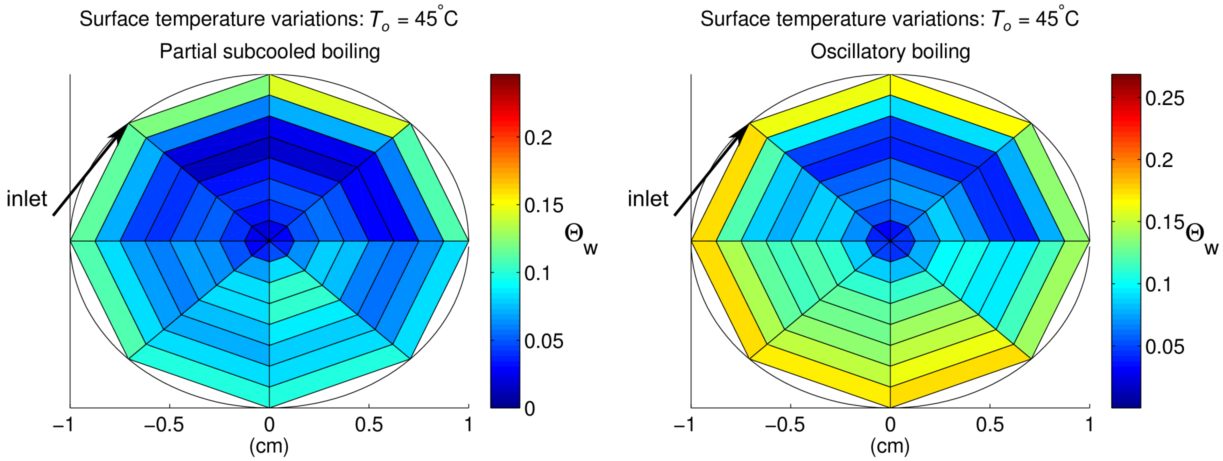

(a) (b)

Figure 6.15: Surface temperature variations for partial subcooled and oscillating boiling regimes with a inlet temperature of 45°C (Subcooling ∼ 55°C)

lowest subcooling range (20-40°C) in Fig. 6.16c. Higher subcooling tests did not have enough fully developed boiling data to make comprehensive asymmetry assessments. Temperature variations were fairly high in this regime, up to 40.7%. Lower temperatures at the center, indicate high heat transfer coefficients at the outlet. The highest surface temperatures were found far from the exit as is seen in single phase and partial subcooled boiling. Here the dynamic forces are weaker and likely have reduced ability to draw vapor off the surface.

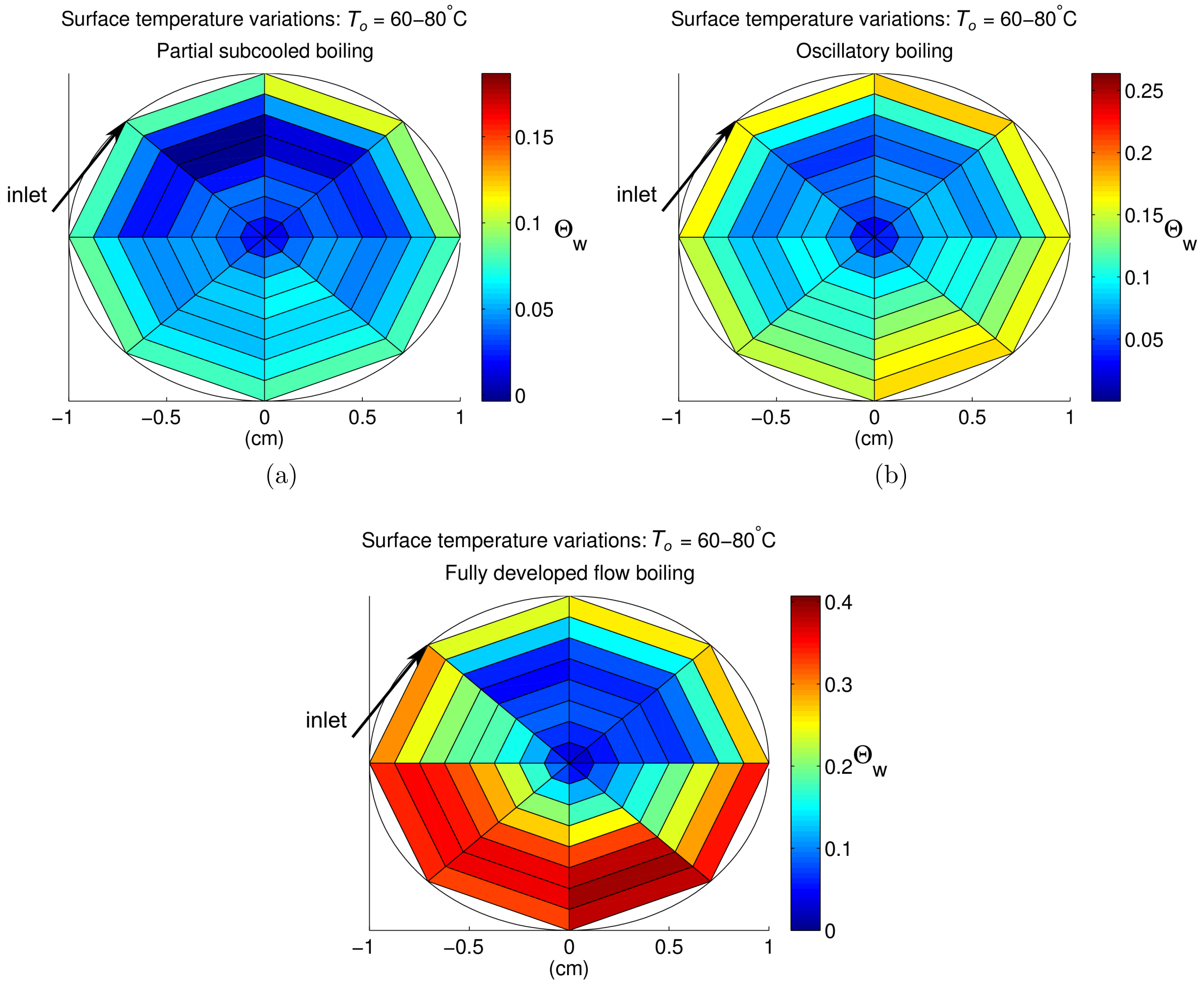

(a)

(b)

(c)

Figure 6.16: Surface temperature variations for partial subcooled, oscillating, and fully developed boiling regimes with a inlet temperature of 60-80°C (Subcooling ∼ 20-40°C)

Heat flux variations were found based on the total percentage difference relative to the average heat flux value. The largest extent of heat flux variation is shown in Tab. 6.3 using the three thermocouple locations underneath the microchannel surface. For partial subcooled flow boiling, the heat fluxes were largest near the inlet region and at center for all three sets of inlet subcooling. The flux variation on the surface was on average up to 25% of the average flux, indicating a condition that is not quite a uniform heat flux. For oscillatory boiling, average variations in heat flux are up to 40%. The highest values are in the center outlet region where high heat transfer coefficients are expected. Additionally, the inlet region showed higher values than the outlet region following similar trends to where surface temperature variations predicted higher heat transfer coefficients. For fully developed boiling, average variations were about 55%. The heat flux at the center was significantly higher than in the outer regions of the channel, likely indicating turbulent heat transfer coefficients at the exit where vapor is drawn towards the outlet. Similar trends as seen for oscillatory flow boiling are seen.

These observations indicate that neither a constant wall surface temperature or wall heat flux condition is expected in a device of this type. However, relatively uniform surface temperature and heat fluxes can be expected especially during partial subcooled flow boiling. indicating increased enhancement towards the center of the device and surface temperature variations significantly lower than the bulk fluid temperature rise.

6.6 Boiling Flow Visualizations

In order to observe the main boiling flow characteristics, images were taken for tests at mean mass flux rates of 255 and 320 kg/m^{2}s. Images with 1/1000 s exposure time are shown.

Table 6.2: Values for percent of surface temperature variations, $\Theta_w \times 100$, for three different flow regimes and fluid subcooling levels

	T_o = 21°C	45°C	60-80°C
PSFB	12.6%	24.6%	19.0%
OFB	24.5%	26.9%	26.4%
FDFB	-	-	40.7%

Table 6.3: Values for heat flux variations relative to the average heat flux, $q''_i/\bar{q}''$ for three different flow regimes and fluid subcooling levels

	T_o = 21°C	45°C	60-80°C
PSFB	24.6%	25.3%	23.6%
OFB	40.0%	30.7%	28.1%
FDFB	-	-	54.9%

Things to note in these images were the bubble size, location of bubble generation, level of bubble coalescence, and regions of perceived dryout of the surface.

As discussed in Sec. 6.1, partial subcooled flow boiling images, Figs. 6.17 and 6.18, show sparse nucleation sites with the initiation of bubbles becoming entrained in the flow. As the heat rate increases however, vapor begins to blanket regions of the surface. This is especially true far from where the inlet directs the flow, which is seen in the left side of these images and especially the bottom left quarter of the microchannel. Figure 6.19 shows an illustration for a typical test during PSFB, indicating the development of small nucleation sites, as well as larger regions of bubbles coalescing in the channel.

Oscillatory flow boiling images are seen in Figs. 6.20 and 6.21. During oscillatory boiling, there are regions with large bubbles or unsteady vapor regions which are seen entrained in the flow as well as regions that look very similar to the PSFB images, with only sparse nucleation sites when subcooled water rushes in and suppresses most of the nucleation. In the top left image of 6.21, a vapor region being pulled into the outlet can be seen. This image likely shows the point at which the subcooled liquid rushes in and pushes a vapor bubble constricting the flow out of the microchannel region. The bottom two set of images in Fig. 6.20 also show two distinct regions when nucleation begins to occur (left image) and when vapor begins to take over regions of the channel (top half of the right image). Figure 6.22 and 6.23 show illustrations for typical tests during OFB, indicating the transition between regions of sparse bubbles and nucleation sites with large vapor swaths in the channel.

Fully developed boiling is seen in Fig. 6.24 showing large regions of vapor being generated on the surface and being swept inwards, especially in the left half of the images. Furthest downstream from the inlet. While it seems these large regions of vapor should initiate dryout on the surface, subsequent flow images indicate vapor being quickly drawn away and liquid then filling in the region (as can be seen in the top left image). This is corroborated by the surface temperatures associated with FDFB being significantly below what is expected for dryout levels. It is postulated that these regions may be subject to annular flow which actually grow from small nucleation sites, and expand into the flow. This leads to the vaporization on the thin film on the surface. Additionally, in regions where these large vapor swashes are seen, waves or ripples can still be seen in the images, indicating that there is not a single phase in the cross-section of the channel, but likely a vapor core and films of liquid on the surfaces of the channel. Once this vapor film is thin enough, dryout may occur in this regime. Figure 6.25 shows an illustration for a typical test during FDFD. Here, large regions of unstable vapor are seen in the channel, as well as regions with many nucleation sites and bubbles entrained in the flow.

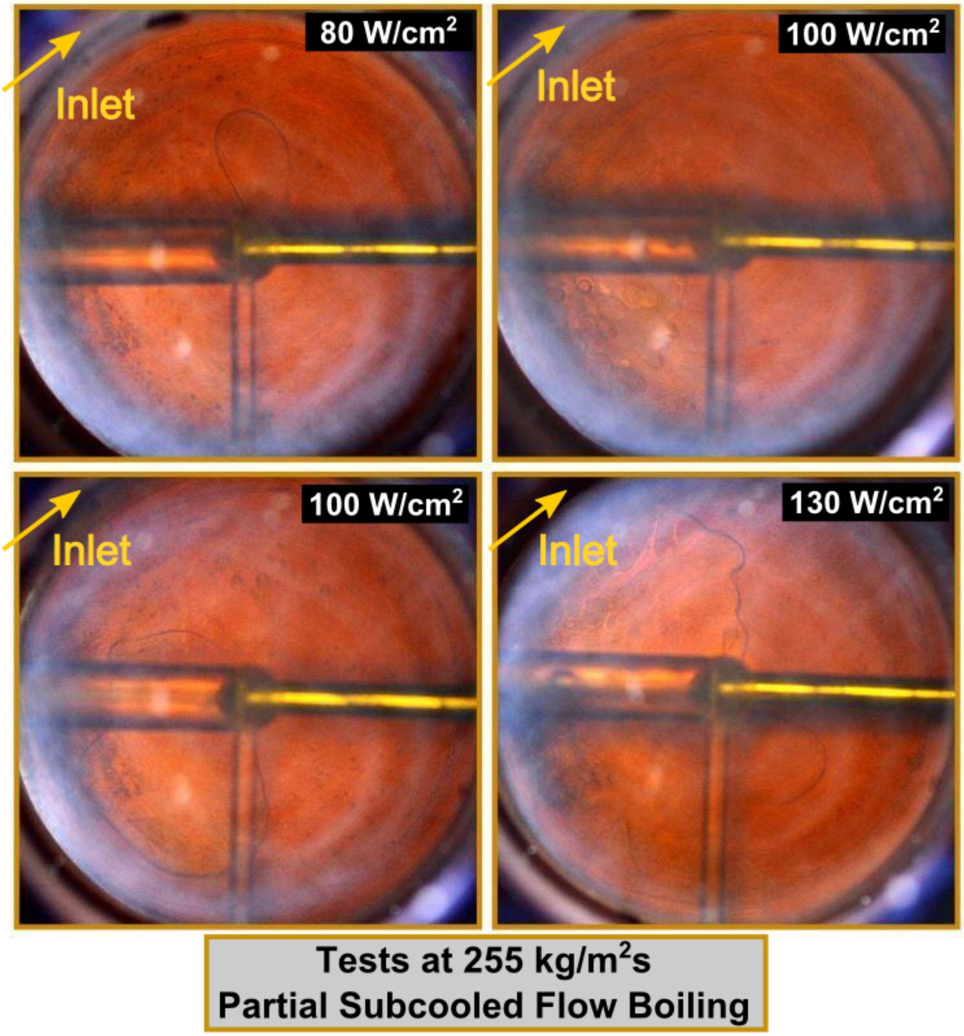

Figure 6.17: Partial Subcooled flow boiling images at mean mass flux $G_m = 255$ kg/m^{2}s

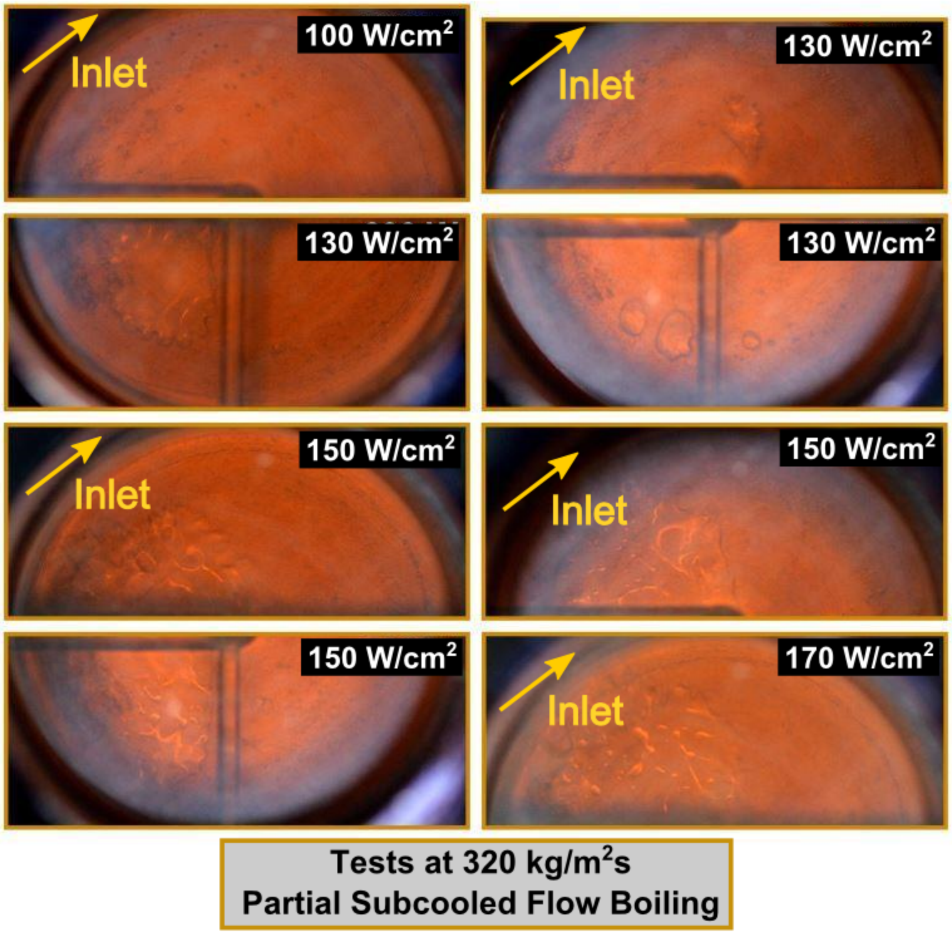

Figure 6.18: Partial Subcooled flow boiling images at mean mass flux $G_m = 320$ kg/m^{2}s

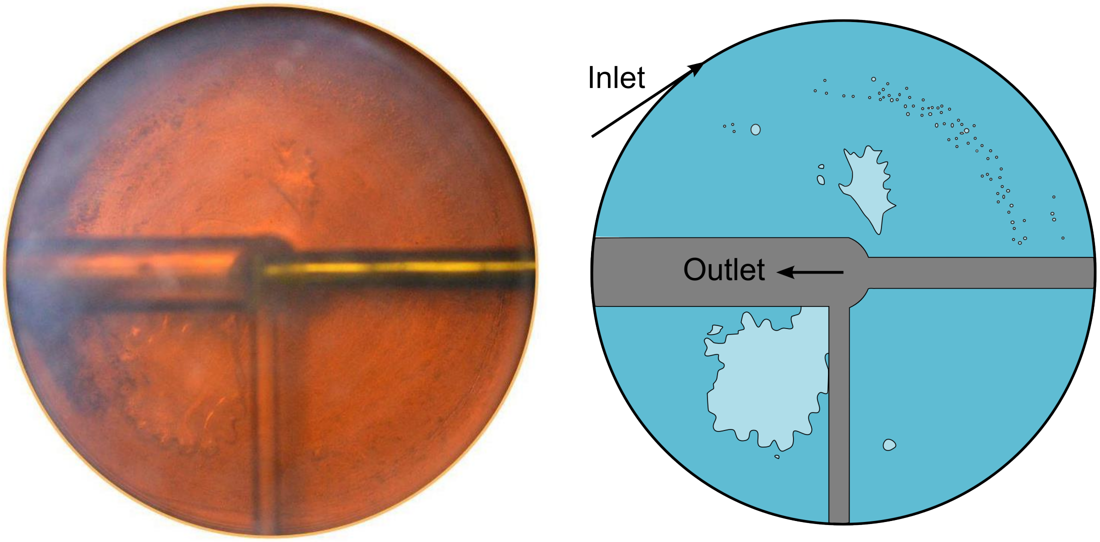

(a) Image of test

(b) Corresponding illustration of vapor in the channel

Figure 6.19: Partial subcooled flow boiling images and outlines of visible vapor at mean mass flux $G_m = 320$ kg/m^{2}s and 130 W/cm^2 (darker blue is liquid, lighter blue is vapor)

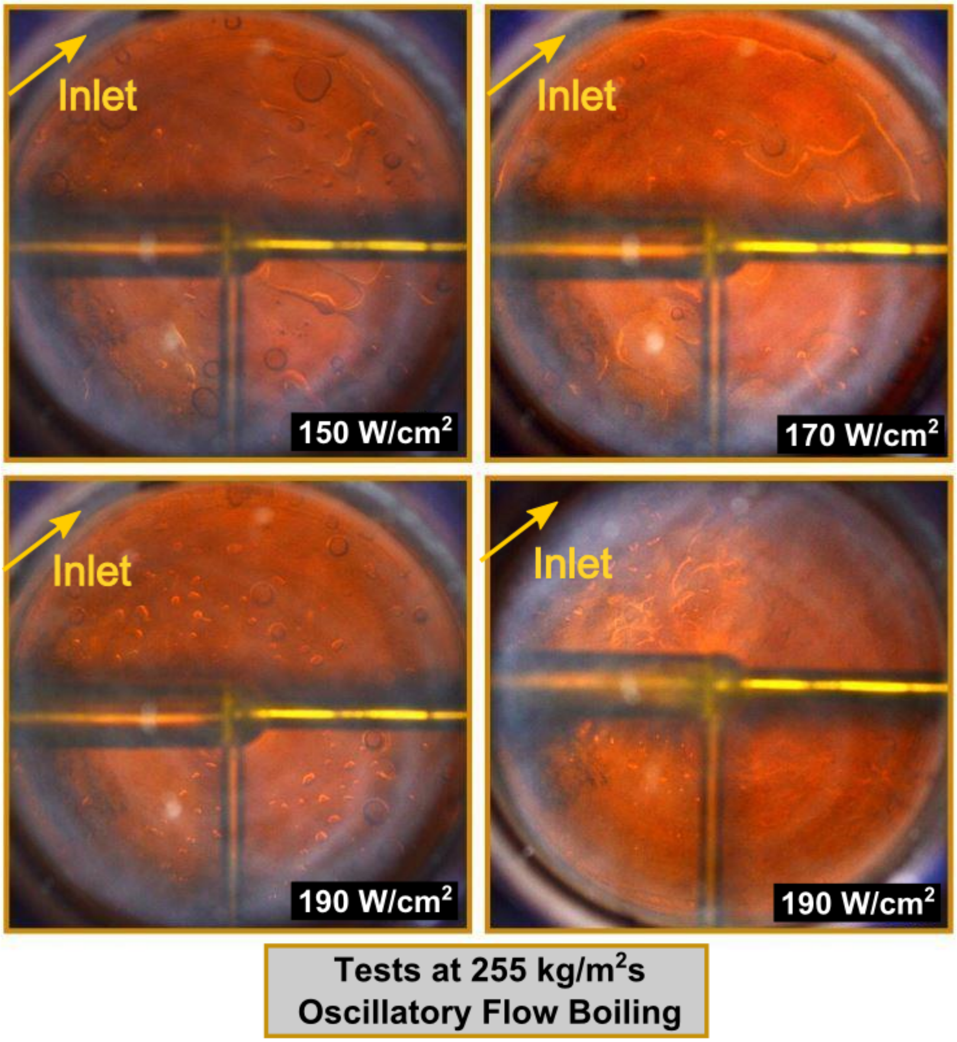

Figure 6.20: Oscillatory flow boiling images at mean mass flux $G_m = 255$ kg/m^{2}s

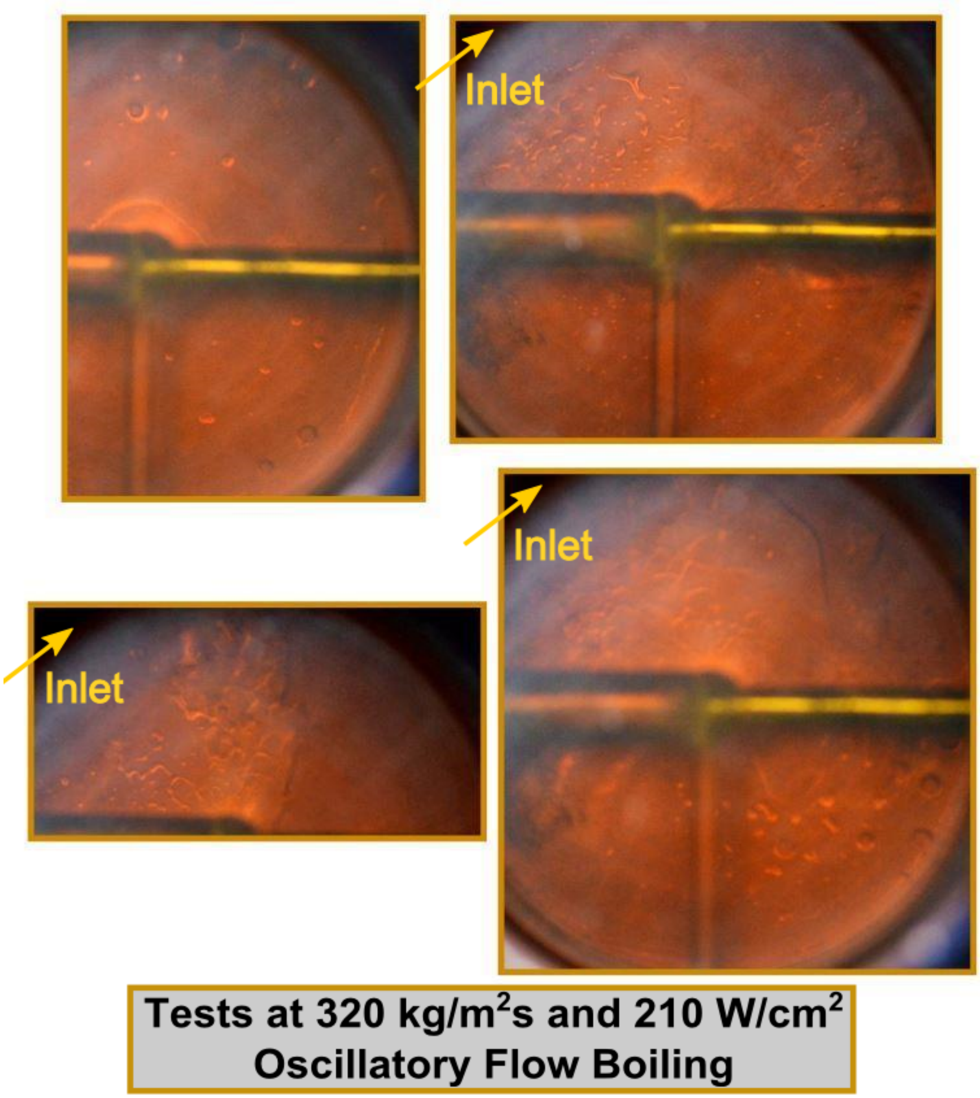

Figure 6.21: Oscillatory flow boiling images at mean mass flux $G_m = 320$ kg/m^{2}s

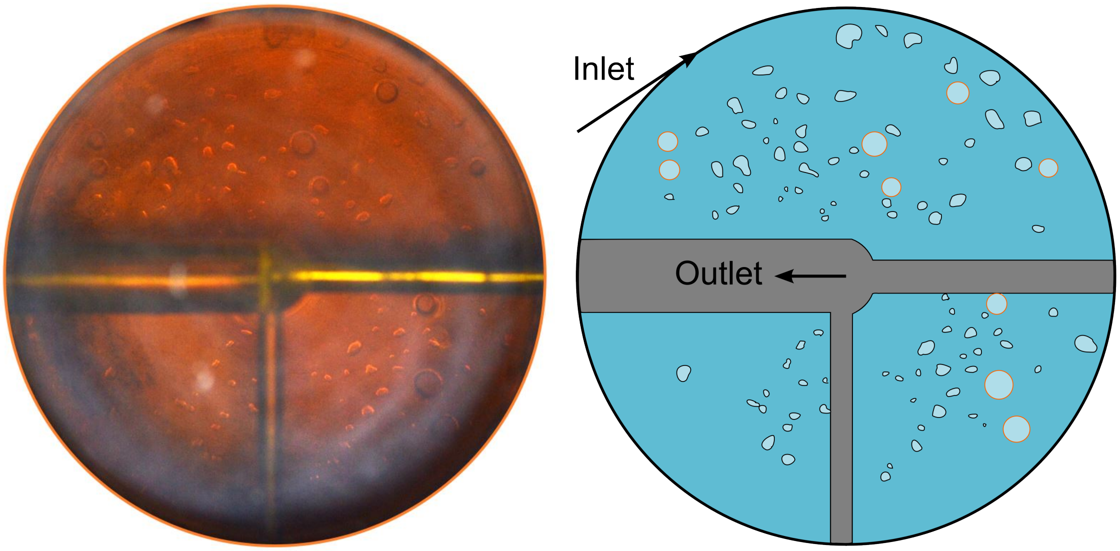

(a) Image of test

(b) Corresponding illustration of vapor in the channel

Figure 6.22: Oscillatory flow boiling images and outlines of visible vapor at mean mass flux $G_m = 255$ kg/m^{2}s and 190 W/cm^2 (darker blue is liquid, lighter blue is vapor)

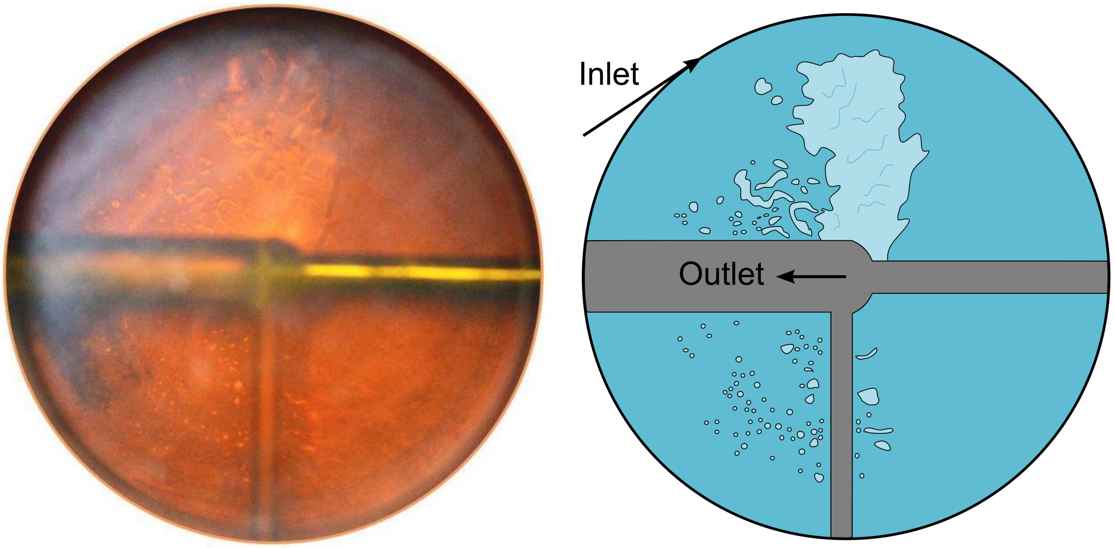

(a) Image of test

(b) Corresponding illustration of vapor in the channel

Figure 6.23: Oscillatory flow boiling images and outlines of visible vapor at mean mass flux $G_m = 320$ kg/m^{2}s and 210 W/cm^2 (darker blue is liquid, lighter blue is vapor)

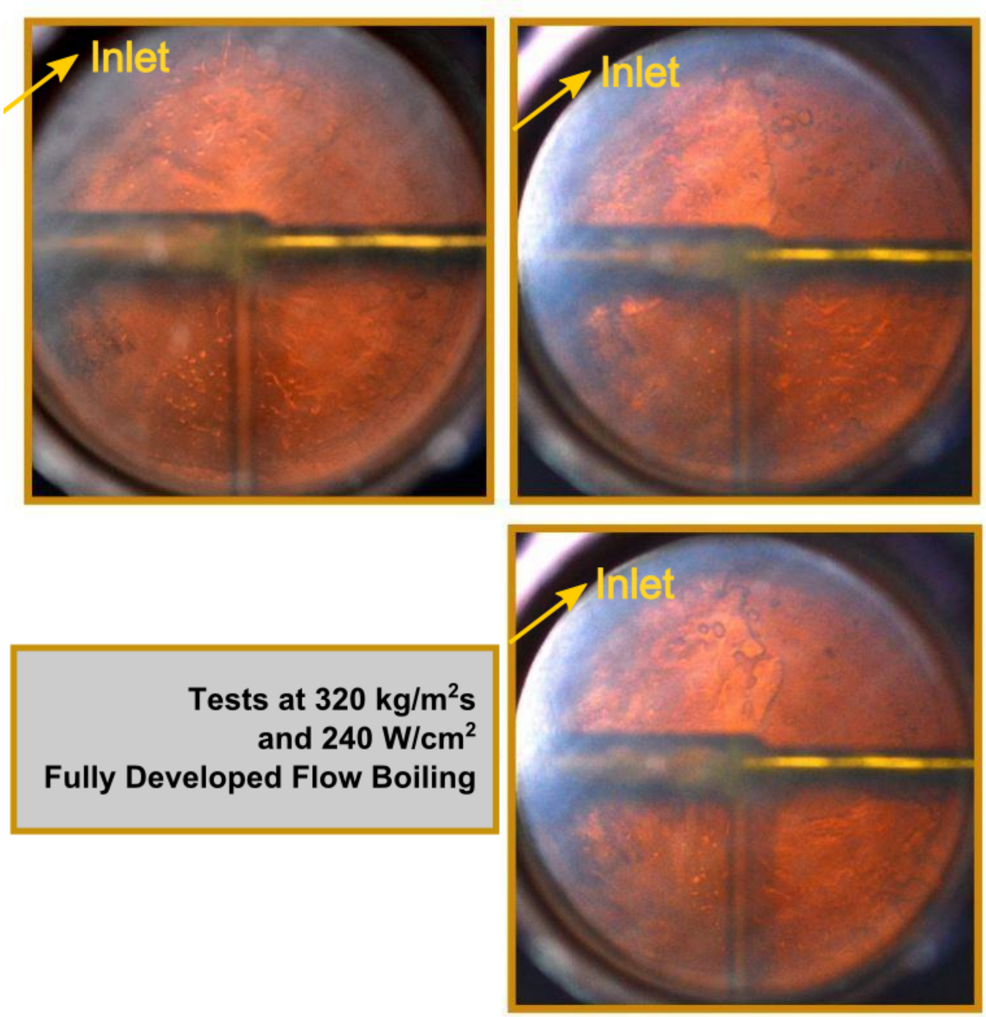

Figure 6.24: Fully developed flow boiling images at mean mass flux $G_m = 320$ kg/m^{2}s

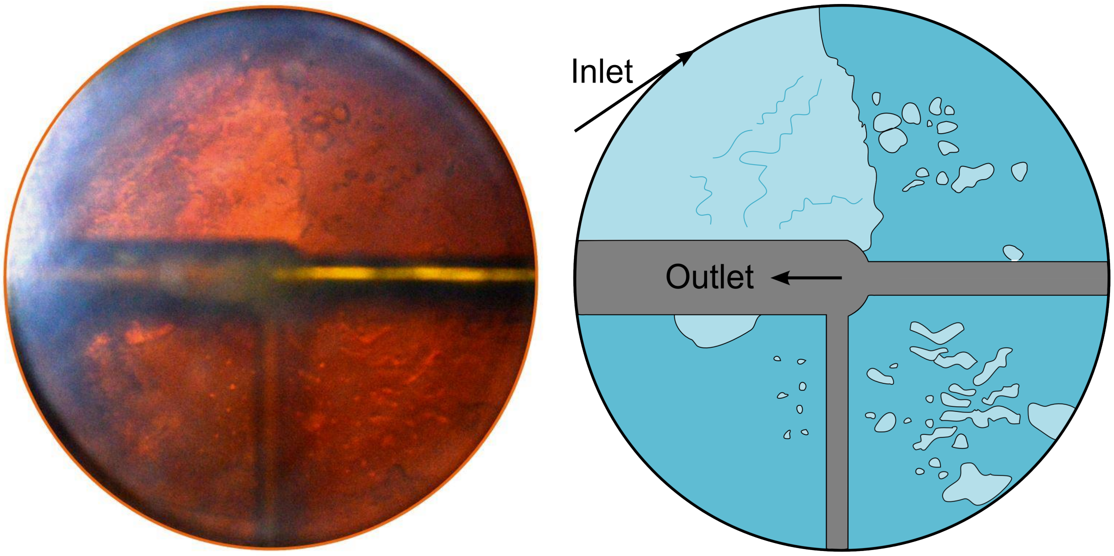

(a) Image of test

(b) Corresponding illustration of vapor in the channel

Figure 6.25: Fully developed flow boiling images and outlines of visible vapor at mean mass flux $G_m = 320$ kg/m^{2}s and 240 W/cm^2 (darker blue is liquid, lighter blue is vapor)

6.7 Oscillation Studies

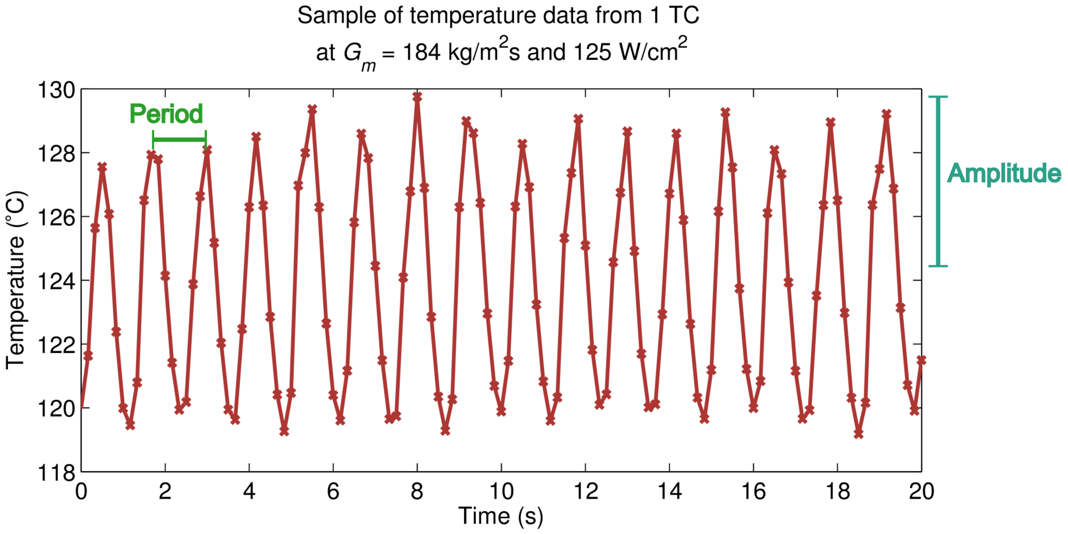

Figure 6.26: Sample of 20 seconds of data recorded from a single thermocouple closest to the cooled surface at $G_m = 184$ and 125 W/cm^2, indicating the amplitude and period of the data

For the tests described above, oscillatory flow was identified as heat rates where the largest oscillation in the temperature at steady state was greater than 5°C. The temperature and pressure data for these tests showed fairly distinct sinusoidal-like behavior. In order to find more information on the oscillatory behavior of the system, tests were done while recording temperature data from the topmost thermocouples at a higher data acquisition rate, recording at 6 Hz rather then the typical 2 Hz. This was done for mean mass flux rates of 184, 255, and 320 kg/m^{2}s where oscillatory behavior more significantly effected the flow. Figure 6.26 shows an example of temperature data for these tests, indicating a distinct period and amplitude sustained in the data at steady state. For both acquisition rates, a discrete Fourier transform was used to assess the dominant frequencies in the oscillations for both. The data at 2 Hz was limited to finding dominant frequencies only if they were below 1 Hz. Figure 6.27 shows an example of three data sets from data at $G_m = 184$ and three heat flux levels which demonstrated oscillatory behavior. This figure shows data from the four top thermocouples recorded at 6 Hz. For this flow rate, the peak frequency increased as heat rate increased, indicating more rapid oscillations as vapor levels increased, however this was not general over all the flow rates. For the tests at 6 Hz showing maximum temperature fluctuations over 5°C, peak frequencies ranged from about 0.5 to 1.2 Hz. The range of dominant frequencies is shown in Fig. 6.28. Figure 6.29 shows the range for tests acquired at 2 Hz, indicating similar ranges as in Fig. 6.28 for the lowest three flow rates and values as low as 0.2 Hz for the highest flow rates. The largest amplitudes of the temperature

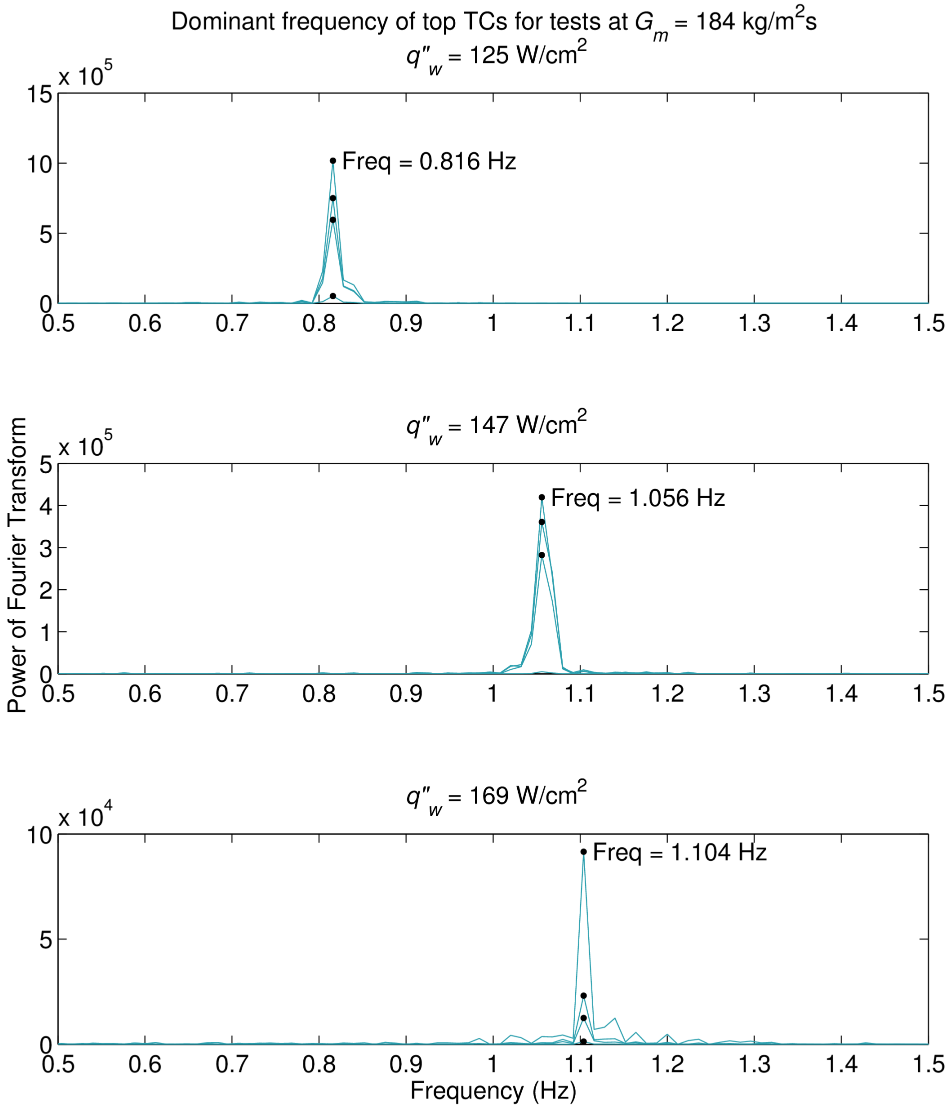

Figure 6.27: Peak frequencies of three tests at $G_m = 184$ kg/m^{2}s and varying heat fluxes indicated in the figure. Data was taken from all four thermocouples closest to the surface.

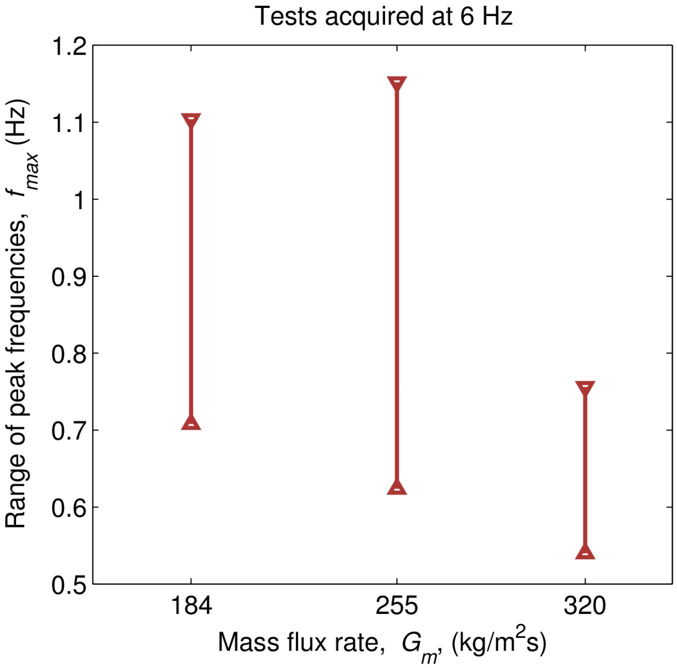

Figure 6.28: Range of peak frequencies for all combination of heat rates and flow rates for tests recorded at 6 Hz. Data was taken from all four thermocouples closest to the surface.

oscillations were in the range of 12-16°C for the tests recorded at 6 Hz for three flow rates and up to 30°C for tests recorded at 2 Hz. The magnitude of the oscillations tended to vary, however, the maximum amplitude of the oscillations typically occurred at lower values of the heat flux rates, with the amplitude dropping off as the heat rate increased and bubbles more rapidly expanded into the channel.

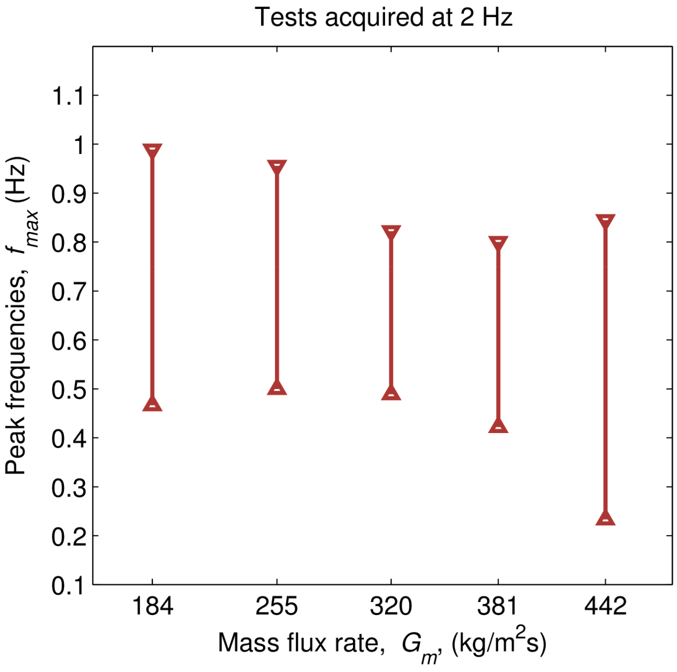

Figure 6.29: Range of peak frequencies for all combination of heat rates and flow rates with room temperature inlet fluid for tests recorded at 2 Hz. Data was taken from all four thermocouples closest to the surface.

6.8 Discussion

A Comparison of the maximum heat transfer coefficients of four values in the literature for two phase flow in microchannels using water is shown in Table 6.4. Heat transfer mechanisms including the development of annular flow evaporation, high forced convective heat transfer, and large buoyant and drag forces on vapor regions can result in the enhancement of heat transfer coefficients in the channel. Thus resulting in the higher values when compared to plain flow in microchannels (indicative of the lower values in Table6.4. The higher local coefficients in studies correspond to enhanced surfaces with reentrant cavities (Kuo and Peles [68]), and higher local values at the onset of nucleate boiling in a relatively small microchannel (Steinke and Kandlikar [69]). One interesting data set is of the study by Qu and Mudawar [70], which is almost directly comparable to the current experimental device values, both having mean mass flux rates of 255 kg/m^{2}s and inlet temperatures of around 60°C. The peak heat transfer coefficients for the spiraling radial inflow device at these values revealed an increase from 3.8 to 5.4 W/cm^{2}K or a 42% increase in heat transfer coefficient.

In a review of high heat flux cooling technology by Agostini et al. [2], lists the ratio of pumping power to heat transfer rate for tests using two phase flow in microchannels. Only a few channels exhibited heat fluxes over 100 W/cm^2. For channels with maximum heat rates over 100 and up to 250 W/cm^2, the pumping power to heat rate ratio W/Q was between 0.33 - 4.8x10^{-5}. For the radial inflow experimental device, pumping power to heat rate ratios, W/Q, as low as 2.9x10^{-5} or 0.0029% are seen at the highest heat rates of about 300 W/cm^2. For heat rates around 100 W/cm^2 values as low as 0.7x10^{-5} are seen. These values are comparable with the previous studies listed in Agostini, yet with higher flux levels, indicating the potential for the use of this device in high flux cooling applications.

Table 6.4: Comparison of the peak heat transfer coefficients for studies on flow boiling of water in microchannels

Author	d_h (μm)	G_m (kg/m^{2}s)	h_{max}(W/cm^{2}K)
Liu and Garimella (2007) [71]	588	224-357	4 (average)
Qu and Mudawar (2003) [70]	350	202	4.5 (local)
Kuo and Peles (2007) [68]	223	303	14 (local)
Steinke and Kandlikar (2004) [69]	207	157-1782	19 (local)
This Study	**600**	**505**	**6.5 (average)**

Chapter 7

Concluding Remarks

A unique type of heat sink device which exhibits enhanced heat transfer characteristics with both single phase and two phase flow has been modeled, manufactured, tested and characterized . The device is simple to manufacture and can easily achieve high heat fluxes with relatively low, uniform surface temperatures.

For single phase flow, the device tested reached an average heat flux of 113 W/cm^2 at a surface temperature of 77°C and of 158 W/cm^2 at a surface temperature of 101°C. The surface temperature gradients were, on average, only 18% of the bulk fluid temperature increase across the channel, while the surface heat flux across the device varied, on average, by 19% relative to the heat flux at the center. The presence of secondary and unsteady flow, as well as thermally developing regions in the flow, enhance heat transfer beyond values for laminar parallel plates with a constant heat flux. Mean Nusselt numbers as high as $\mathrm{Nu_m} = 24$ substantiate the claim of enhancement due to the flow instabilities and unsteady transition regions as seen in the visualization studies. One unique feature of this use of the device is the ability for the flow to transition into turbulent flow regimes downstream due to the acceleration of flow in the center portion of the device, where the fluid tends to be warmer and there is a larger need for enhanced heat transfer coefficients.

The single phase analytical model provides relatively good correlation to the experimental streaklines for the flow, indicating the bulk flow follows the general trend derived in the analytical model. However, the experimental pressure drop is an average of 76% higher than the model. This is likely caused by the presence of secondary and unsteady flow not accounted for in the model. Goodness factors for the device are comparable to to developing flow in parallel plates, and higher than fully developed flows. This indicates that higher pressure drops in the system are more than compensated by the enhancement of heat transfer that is occurring.

Further, simple improvements to the device could be achieved using single phase flow. Changing the design to incorporate multiple inlets would likely help mitigate asymmetries in temperature and heat flux since the average gradient spans the whole channel rather than just from edge to center. Increasing the flow rate would lead to increased Nusselt values if extrapolated from Fig. 5.6, and thus lower surface temperatures for a given heat flux. However, this would result in higher pumping penalties which can be extrapolated from Fig. 5.1. Similarly, it is predicted that decreasing the gap size would increase the heat transfer coefficient, if operating at the same Reynolds number. This would allow for lower surface temperatures at a given heat flux, although with higher pumping penalties likely increasing as the functional form of Eq. (3.44) suggests. Surface roughness at smaller gap sizes could also lead to more significant enhancement.

For two phase boiling flow, high heat transfer performance is demonstrated and the characteristics of boiling heat transfer in the microchannel are identified. The mechanisms of boiling heat transfer in this type of microchannel spiraling inflow device had not been described previously and proves to be distinct from conventional nucleate boiling or flow boiling in tubes as is evidenced by flow visualization studies. Bubbles that occur on the surface tend to quickly expand in all directions and get dragged along with the flow, resulting in slug-like vapor regions that do not hold a specified shape. As this vapor region gets entrained in the flow over the surface, a thin wetted region can remain on the surface, resulting in evaporation from a thin liquid film on the surface. This has implications on the mechanism of dryout. Rather than a result of vapor crowding, dryout may occur in the thin film beneath a vapor region subject to film evaporation.

The mechanisms by which boiling in the heat sink enhances heat transfer are three-fold. First, the large forces on bubbles due to drag and buoyant forces will tend to draw vapor towards the outlet of the cooling device. This also allows for release of bubbles into the flow from all regions of the surface, preventing the development of hot spots. Second, when large vapor slugs form in the channel, although they constrict the channel, they will still tend to travel over a thin film on the wetted surface, leading to evaporation into the bubble. In addition to dragging other bubbles with the slug, towards the outlet, the evaporative effect on the thin film surface leads to high heat transfer coefficients. Finally, the single phase convective heat transfer coefficients are large due to unsteady, secondary flow motions, contributing significantly to the heat transfer, especially in the partial subcooled flow boiling regime.

Enhancement of heat transfer allows for heat flux levels beyond model values for critical heat flux, up to 240% of the value for the Zuber pool boiling model for critical heat flux and 30% more than the Qu and Mudawar model for saturated flow in a microchannel. Surface average heat flux rates up to 300 W/cm^2 were seen at the highest mass flow rates. At this point, the system exhibited an average surface temperature of 134°C and a pumping power of 0.01% of the total heat rate dissipated. Heat transfer coefficients were also seen up to 6.5 W/cm^{2}K during fully developed boiling in the channel, revealing promising cooling performance for electronics cooling or concentrated photovoltaic cooling applications.

Three flow regimes have been identified indicating preferred conditions during partial subcooled and fully developed flow boiling, and undesirable conditions in the oscillatory flow boiling regime. Design considerations which can help reduce the level of oscillations without large pressure penalties are needed. The use of combinations of working fluid and surfaces that are more wetting may result in the reduction of oscillations and increased critical heat flux levels. The pressure drop characteristics during partial subcooled flow boiling were particularly promising, requiring a relatively small increase in pressure drop for large increases in heat transfer coefficients due to nucleation at the surface (for $G_m = 618$ kg/m^{2}s, a 36% increase in pressure drop corresponded to a 127% increase in heat transfer coefficient). Overall, this type of device shows reliable performance and potential for use in high heat flux cooling applications.

Bibliography

[1] I. Mudawar, “Two-phase microchannel heat sinks: theory, applications, and limitations,” *Journal of Electronic Packaging*, vol. 133, no. 4, p. 041 002, 2011.

[2] B. Agostini, M. Fabbri, J. E. Park, L. Wojtan, J. R. Thome, and B. Michel, “State of the art of high heat flux cooling technologies,” *Heat Transfer Engineering*, vol. 28, no. 4, pp. 258–281, 2007.

[3] M. Ebadian and C. Lin, “A review of high-heat-flux heat removal technologies,” *Journal of heat transfer*, vol. 133, no. 11, p. 110 801, 2011.

[4] S. G. Kandlikar, “High flux heat removal with microchannelsa roadmap of challenges and opportunities,” *Heat Transfer Engineering*, vol. 26, no. 8, pp. 5–14, 2005.

[5] S. G. Kandlikar, S. Colin, Y. Peles, S. Garimella, R. F. Pease, J. J. Brandner, and D. B. Tuckerman, “Heat transfer in microchannels2012 status and research needs,” *Journal of Heat Transfer*, vol. 135, no. 9, p. 091 001, 2013.

[6] J.-M. Koo, S. Im, L. Jiang, and K. E. Goodson, “Integrated microchannel cooling for three-dimensional electronic circuit architectures,” *Journal of heat transfer*, vol. 127, no. 1, pp. 49–58, 2005.

[7] F. Dimroth, T. N. Tibbits, P. Beutel, C. Karcher, E. Oliva, G. Siefer, M. Schachtner, A. Wekkeli, M. Steiner, M. Wiesenfarth, *et al.*, “Development of high efficiency wafer bonded 4-junction solar cells for concentrator photovoltaic applications,” in *Photovoltaic Specialist Conference (PVSC), 2014 IEEE 40th*, IEEE, 2014, pp. 0006–0010.

[8] S Kurtz, “Opportunities and challenges for development of a mature concentrating photovoltaic power industry (revision),” National Renewable Energy Laboratory (NREL), Golden, CO., Tech. Rep., 2012.

[9] M. A. Steiner, J. F. Geisz, D. J. Friedman, W. J. Olavarria, A. Duda, and T. E. Moriarty, “Temperature-dependent measurements of an inverted metamorphic multijunction (imm) solar cell,” in *Photovoltaic Specialists Conference (PVSC), 2011 37th IEEE*, IEEE, 2011, pp. 2527–2532.

[10] A. Royne, C. J. Dey, and D. R. Mills, “Cooling of photovoltaic cells under concentrated illumination: a critical review,” *Solar energy materials and solar cells*, vol. 86, no. 4, pp. 451–483, 2005.

[11] V. Tyagi, S. Kaushik, and S. Tyagi, "Advancement in solar photovoltaic/thermal (pv/t) hybrid collector technology," *Renewable and Sustainable Energy Reviews*, vol. 16, no. 3, pp. 1383–1398, 2012.

[12] D. B. Tuckerman and R. Pease, "High-performance heat sinking for vlsi," *Electron Device Letters, IEEE*, vol. 2, no. 5, pp. 126–129, 1981.

[13] S. Ndao, Y. Peles, and M. K. Jensen, "Multi-objective thermal design optimization and comparative analysis of electronics cooling technologies," *International Journal of Heat and Mass Transfer*, vol. 52, no. 19-20, pp. 4317 –4326, 2009, ISSN: 0017-9310.

[14] S. Kandlikar and A. Bapat, "Evaluation of jet impingement, spray and microchannel chip cooling options for high heat flux removal," *Heat Transfer Engineering*, vol. 28, no. 11, pp. 911–923, 2007.

[15] Z. Wu and B. Sundén, "On further enhancement of single-phase and flow boiling heat transfer in micro/minichannels," *Renewable and Sustainable Energy Reviews*, vol. 40, pp. 11–27, 2014.

[16] S.-M. Kim and I. Mudawar, "Review of databases and predictive methods for heat transfer in condensing and boiling mini/micro-channel flows," *International Journal of Heat and Mass Transfer*, vol. 77, pp. 627–652, 2014.

[17] T. Ho, S. S. Mao, and R. Greif, "The impact of cooling on cell temperature and the practical solar concentration limits for photovoltaics," *International Journal of Energy Research*, vol. 35, no. 14, pp. 1250–1257, 2011.

[18] G. Hetsroni, A. Mosyak, Z. Segal, and G. Ziskind, "A uniform temperature heat sink for cooling of electronic devices," *International Journal of Heat and Mass Transfer*, vol. 45, no. 16, pp. 3275 –3286, 2002, ISSN: 0017-9310. DOI: `10.1016/S0017-9310(02)00048-0`.

[19] M. El-Masri and J. Louis, "On the design of high-temperature gas turbine blade water-cooling channels," *Journal of Engineering for Gas Turbines and Power*, vol. 100, no. 4, pp. 586–591, 1978.

[20] M. V. Sardeshpande and V. V. Ranade, "Two-phase flow boiling in small channels: a brief review," *Sadhana*, vol. 38, no. 6, pp. 1083–1126, 2013.

[21] C. B. Tibirica and G. Ribatski, "Flow boiling in micro-scale channels–synthesized literature review," *International Journal of Refrigeration*, vol. 36, no. 2, pp. 301–324, 2013.

[22] S. G. Kandlikar, "Scale effects on flow boiling heat transfer in microchannels: a fundamental perspective," *International Journal of Thermal Sciences*, vol. 49, no. 7, pp. 1073–1085, 2010.

[23] T. Harirchian and S. V. Garimella, "Boiling heat transfer and flow regimes in microchannelsa comprehensive understanding," *Journal of Electronic Packaging*, vol. 133, no. 1, p. 011 001, 2011.

[24] J. Yeom, M. A. Shannon, G Yogesh, T Osamu, and Z Hans, "Micro-coolers," *Comprehensive Microsystems*, vol. 3, pp. 499–550, 2008.

[25] S. Heffington and A Glezer, "Two-phase thermal management using a small-scale, heat transfer cell based on vibration-induced droplet atomization," in *Thermal and Thermomechanical Phenomena in Electronic Systems, 2004. ITHERM'04. The Ninth Intersociety Conference on*, IEEE, vol. 2, 2004, pp. 90–94.

[26] A. Akbarzadeh and T. Wadowski, "Heat pipe-based cooling systems for photovoltaic cells under concentrated solar radiation," *Applied Thermal Engineering*, vol. 16, no. 1, pp. 81 –87, 1996, ISSN: 1359-4311.

[27] K. M. Armijo, "Heat pipe performance enhancement with binary mixture fluids that exhibit strong concentration marangoni effects," English, PhD thesis, 2011, p. 101.

[28] W. G. Anderson, S. Tamanna, D. B. Sarraf, P. M. Dussinger, and R. W. Hoffman Jr, "Heat pipe cooling of concentrating photovoltaic (cpv) systems," *6th IECEC, July*, pp. 28–30, 2008.

[29] L. Micheli, N. Sarmah, X. Luo, K. Reddy, and T. K. Mallick, "Opportunities and challenges in micro-and nano-technologies for concentrating photovoltaic cooling: a review," *Renewable and Sustainable Energy Reviews*, vol. 20, pp. 595–610, 2013.

[30] C. Sobhan, R. Rag, and G. Peterson, "A review and comparative study of the investigations on micro heat pipes," *International Journal of Energy Research*, vol. 31, no. 6-7, pp. 664–688, 2007.

[31] R Sureshkumar, S. T. Mohideen, and N Nethaji, "Heat transfer characteristics of nanofluids in heat pipes: a review," *Renewable and Sustainable Energy Reviews*, vol. 20, pp. 397–410, 2013.

[32] J. H. McGinn, "Observations on the radial flow of water between fixed parallel plates," *Applied Scientific Research, Section A*, vol. 5, no. 4, pp. 255–264, 1955.

[33] K. Boyd and W Rice, "Laminar inward flow of an incompressible fluid between rotating disks, with full peripheral admission," *Journal of Applied Mechanics*, vol. 35, no. 2, pp. 229–237, 1968.

[34] A Singh, B. Vyas, and U. Powle, "Investigations on inward flow between two stationary parallel disks," *International journal of heat and fluid flow*, vol. 20, no. 4, pp. 395–401, 1999.

[35] S. Petitot, A. Lyazid, and R. Devienne, "Experimental study of the velocity field in a vortex-flow heat exchanger with isothermal conditions," *Experiments in fluids*, vol. 34, no. 3, pp. 418–429, 2003.

[36] S Mochizuki and W.-J. Yang, "Local heat-transfer performance and mechanisms in radial flow between parallel disks," *Journal of thermophysics and heat transfer*, vol. 1, no. 2, pp. 112–116, 1987.

[37] S Mochizuki, W.-J. Yang, Y Yagi, and M Ueno, "Heat transfer mechanisms and performance in multiple parallel disk assemblies," *Journal of heat transfer*, vol. 105, no. 3, pp. 598–604, 1983.

[38] N. Suryanarayana, T Scofield, and R. Kleiss, "Heat transfer to a fluid in radial, outward flow between two coaxial stationary or corotating disks," *Journal of heat transfer*, vol. 105, no. 3, pp. 519–526, 1983.

[39] G. Roy, S. J. Palm, and C. T. Nguyen, "Heat transfer and fluid flow of nanofluids in laminar radial flow cooling systems," *Journal of Thermal Science*, vol. 14, no. 4, pp. 362–367, 2005.

[40] I. Gherasim, G. Roy, C. T. Nguyen, and D. Vo-Ngoc, "Experimental investigation of nanofluids in confined laminar radial flows," *International Journal of Thermal Sciences*, vol. 48, no. 8, pp. 1486–1493, 2009.

[41] ——, "Heat transfer enhancement and pumping power in confined radial flows using nanoparticle suspensions (nanofluids)," *International Journal of Thermal Sciences*, vol. 50, no. 3, pp. 369–377, 2011.

[42] M. Djaoui, A. Dyment, and R. Debuchy, "Heat transfer in a rotor–stator system with a radial inflow," *European Journal of Mechanics-B/Fluids*, vol. 20, no. 3, pp. 371–398, 2001.

[43] R. Devienne and G. Cognet, "Velocity field and heat transfer in a vortex flow exchanger," *Heat and Mass Transfer*, vol. 25, no. 3, pp. 185–191, 1990.

[44] C. Forsberg, D. Moses, E. Lewis, R Gibson, R Pearson, W. Reich, G. Murphy, R. Staunton, and W. Kohn, "Proposed and existing passive and inherent safety-related structures, systems, and components (building blocks) for advanced light-water reactors," Oak Ridge National Lab., TN (USA), Tech. Rep., 1989.

[45] A. A. Kulkarni, V. V. Ranade, R Rajeev, and S. Koganti, "Pressure drop across vortex diodes: experiments and design guidelines," *Chemical Engineering Science*, vol. 64, no. 6, pp. 1285–1292, 2009.

[46] A. Kulkarni, V. Ranade, R Rajeev, and S. Koganti, "Cfd simulation of flow in vortex diodes," *AIChE journal*, vol. 54, no. 5, pp. 1139–1152, 2008.

[47] A Motamed-Amini and I Owen, "The expansion of wet steam through a compressible confined vortex in a fluidic vortex diode," *International journal of multiphase flow*, vol. 13, no. 6, pp. 845–856, 1987.

[48] G. Priestman, "A study of vortex throttles part 1: experimental," *Proceedings of the Institution of Mechanical Engineers, Part C: Journal of Mechanical Engineering Science*, vol. 201, no. 5, pp. 331–336, 1987.

[49] ——, "A study of vortex throttles part 2: viscid flow analysis," *Proceedings of the Institution of Mechanical Engineers, Part C: Journal of Mechanical Engineering Science*, vol. 201, no. 5, pp. 337–343, 1987.

[50] M. Anduze, S. Colin, R. Caen, H. Camon, V. Conedera, and T. Do Conto, "Analysis and testing of a fluidic vortex microdiode," *Journal of Micromechanics and Microengineering*, vol. 11, no. 2, p. 108, 2001.

[51] G. L. Yoder Jr, Y. Elkassabgi, R. Cunningham, *et al.*, "Vortex diode analysis and testing for fluoride salt-cooled high-temperature reactors," *ORNL/TM-2011/425, ORNL, Oak Ridge, TN*, 2011.

[52] J. Leland and L. Chow, "Channel height and curvature effects on flow boiling from an electronic chip," *Journal of thermophysics and heat transfer*, vol. 9, no. 2, pp. 292–301, 1995.

[53] J. E. Galloway and I. Mudawar, "Critical heat flux enhancement by means of liquid subcooling and centrifugal force induced by flow curvature," *International journal of heat and mass transfer*, vol. 35, no. 5, pp. 1247–1260, 1992.

[54] J. C. Sturgis and I. Mudawar, "Critical heat flux in a long, curved channel subjected to concave heating," *International journal of heat and mass transfer*, vol. 42, no. 20, pp. 3831–3848, 1999.

[55] J. Sturgis and I. Mudawar, "Assessment of chf enhancement mechanisms in a curved, rectangular channel subjected to concave heating," *Transactions- ASME Journal of Heat Transfer*, vol. 121, pp. 394–404, 1999.

[56] V. D. Romanin and V. P. Carey, "An integral perturbation model of flow and momentum transport in rotating microchannels with smooth or microstructured wall surfaces," *Physics of Fluids*, vol. 23, no. 8, p. 082 003, 2011.

[57] D. Bohne, S. Fischer, and E. Obermeier, "Thermal, conductivity, density, viscosity, and prandtl-numbers of ethylene glycol-water mixtures," *Berichte der Bunsengesellschaft für physikalische Chemie*, vol. 88, no. 8, pp. 739–742, 1984.

[58] W. M. Rohsenow, "Heat transfer with evaporation," in *Proceedings of Heat TransferA Symposium Held at the University of Michigan During the Summer of 1952*, 1953, pp. 101–150.

[59] V. Carey, *Liquid Vapor Phase Change Phenomena: An Introduction to the Thermophysics of Vaporization and Condensation Processes in Heat Transfer Equipment, Second Edition.* Taylor & Francis, 2007, ISBN: 9781591690351.

[60] J. B. Taylor, A. L. Carrano, and S. G. Kandlikar, "Characterization of the effect of surface roughness and texture on fluid flowpast, present, and future," *International journal of thermal sciences*, vol. 45, no. 10, pp. 962–968, 2006.

[61] H. S. Heaton, W. C. Reynolds, and W. M. Kays, "Heat transfer in annular passages. simultaneous development of velocity and temperature fields in laminar flow," *International Journal of Heat and Mass Transfer*, vol. 7, no. 7, pp. 763–781, 1964.

[62] R. Webb, *Principles of enhanced heat transfer*, ser. Wiley-Interscience publication. John Wiley & Sons, 1994, ISBN: 9780471577782.

[63] R. Shah and A. London, *Laminar flow forced convection in ducts: a source book for compact heat exchanger analytical data*, ser. Advances in heat transfer: Supplement. Academic Press, 1978, ISBN: 9780120200511.

[64] A. Bergles and S. Kandlikar, "On the nature of critical heat flux in microchannels," *Journal of Heat Transfer*, vol. 127, no. 1, pp. 101–107, 2005.

[65] N. Zuber, "Hydrodynamic aspects of boiling heat transfer (thesis)," California. Univ., Los Angeles; and Ramo-Wooldridge Corp., Los Angeles, Tech. Rep., 1959.

[66] G. Celata, M Cumo, and A Mariani, "Assessment of correlations and models for the prediction of chf in water subcooled flow boiling," *International journal of heat and mass transfer*, vol. 37, no. 2, pp. 237–255, 1994.

[67] W. Qu and I. Mudawar, "Measurement and correlation of critical heat flux in two-phase micro-channel heat sinks," *International Journal of Heat and Mass Transfer*, vol. 47, no. 10, pp. 2045–2059, 2004.

[68] C.-J. Kuo and Y Peles, "Local measurement of flow boiling in structured surface microchannels," *International Journal of Heat and Mass Transfer*, vol. 50, no. 23, pp. 4513–4526, 2007.

[69] M. E. Steinke and S. G. Kandlikar, "An experimental investigation of flow boiling characteristics of water in parallel microchannels," *Journal of Heat Transfer*, vol. 126, no. 4, pp. 518–526, 2004.

[70] W. Qu and I. Mudawar, "Flow boiling heat transfer in two-phase micro-channel heat sinks—-i. experimental investigation and assessment of correlation methods," *International Journal of Heat and Mass Transfer*, vol. 46, no. 15, pp. 2755–2771, 2003.

[71] D. Liu and S. V. Garimella, "Flow boiling heat transfer in microchannels," *Journal of Heat Transfer*, vol. 129, no. 10, pp. 1321–1332, 2007.

[72] F. White, *Fluid Mechanics*, ser. McGraw-Hill series in mechanical engineering. McGraw-Hill, 2008.

[73] W. Kays, M. Crawford, and B. Weigand, *Convective heat and mass transfer*. McGraw-Hill New York, 1993.

Appendix A

Nomenclature

A	surface area
a_c	centripetal acceleration
b	gap height
Bo	boiling number
$\mathrm{Bo_c}$	Bond number based on centripetal acceleration
Ca	Capillary number
c_p	specific heat capacity
CF	concentration factor
d_h	hydraulic diameter
e	error of measurement
f	Fanning friction factor, or frequency of oscillations
f_{max}	dominant frequency associated with oscillations (max value in Fourier transform)
FDFB	fully developed flow boiling
G	mass flux rate
g	gravitational constant, 9.8 $\mathrm{m/s^2}$
h	convective heat transfer coefficient
h_{lv}	latent heat of vaporization (enthalpy of formation for vapor)
i	specific enthalpy
j	Colburn factor
Ja	Jakob number
k	thermal conductivity
$\dot{m}$	mass flux
Nu	Nusselt number
OFB	oscillatory flow boiling
P	pressure
P^*	dimensionless pressure
Pe	Peclet number
Pr	Prandtl number
PSFB	partial subcooled flow boiling

q''_w	wall heat flux
$\dot{Q}$	total heat rate
r	radial direction or location
R	dimensionless radial location r/r_o
Re	total Reynolds number
$\mathrm{Re_m}$	modified Reynolds number, $\mathrm{Re_r}\epsilon$
$\mathrm{Re_r}$	radial Reynolds number
s	length along flow path
s^*	dimensionless flow path length
t	time
T	temperature
v	velocity
V	dimensionless velocity
$\bar{v}$	mean velocity in the channel at r
W	ratio of initial tangential to radial velocity
$\dot{\mathcal{W}}$	pumping power
We	Weber number
x	fluid quality
z	axial direction
Z	dimensionless axial direction

Greek letters

α	dimensionless gap slope
β	dimensionless gap size
ε	initial aspect ratio of gap size to outer radius
η	PV cell efficiency
θ	tangential direction
Θ_w	dimensionless wall temperature
Θ_{sub}	dimensionless subcooling level
μ	dynamic viscosity of working fluid
ν	kinematic viscosity of working fluid
ρ	density
σ	surface tension
ϕ	dimensionless velocity formulation

Subscripts

b	bulk flow property
cu	property of the Cu-145 alloy
e	property at the channel exit (same as i)
i	property at the inner radius, r_i
l	property of the working fluid in liquid state

m	mean device property
max	maximum property value reached experimentally
nb	nucleate boiling contribution
o	property at the outer radius, r_o, (channel inlet)
onb	onset of nucleate boiling
r	in the radial direction
rt	at room temperature
sat	fluid property at saturation
sp	single phase contribution
T	solution for a constant wall temperature condition
v	property of the working fluid in the vapor state
w	property at the wall
z	in the axial direction
θ	in the tangential direction

Appendix B

Full Derivations of Analytical Solutions

B.1 Derivation of Velocity and Pressure Distributions for Linearly Varying Gap Size

In order to solve for the velocity and pressure distributions in the heat sink, the continuity and momentum equations must be solved. The following presents the full derivation of the velocities in the r, θ,and z directions as well as the total average pressure drop across the channel. The following assumptions are made:

- The flow is steady, incompressible, and has constant properties.
- The flow is laminar. The use of microchannels results in small Reynolds numbers.
- The flow is axisymmetric, therefore, all θ derivatives of flow quantities are zero.
- No entrance or exit effects are considered.
- The flow length, r_o, is much larger than the initial gap size, b_o, so that $b_o/r_o << 1$

Step 1: Postulate velocity profiles

The following parabolic solutions are postulated for the radial and tangential velocities for a gap of varying size, $b(r)$:

$$v_r = \bar{v}_r(r)\phi(z,b) \tag{B.1}$$

$$v_\theta = \bar{v}_\theta(r)\phi(z,b) \tag{B.2}$$

where

$$\phi(z,b) = \frac{3}{2}\left[1 - \left(\frac{2z}{b}\right)^2\right] \tag{B.3}$$

and $\bar{v}_r$ and $\bar{v}_\theta$ are mean velocities defined as

$$\bar{v}_r(r) = \frac{1}{b}\int_{-b/2}^{b/2} v_r dz \tag{B.4}$$

$$\bar{v}_\theta(r) = \frac{1}{b}\int_{-b/2}^{b/2} v_\theta dz \tag{B.5}$$

Assuming $b(r)$ is linear, it can be written as

$$b(r) = \frac{b_o - b_i}{r_o - r_i}(r - r_o) + b_o \tag{B.6}$$

This can be written in nondimensional form using

$$R = r/r_o \tag{B.7}$$

$$\beta = b/b_o \tag{B.8}$$

Defining $\alpha = (1-\beta_i)/(1-R_i)$ such that β can be written as

$$\beta = \alpha R - \alpha + 1 \tag{B.9}$$

Step 2: Use mass conservation to solve for v_r

Knowing the mass flux is constant through any cross-sectional disk

$$\dot{m} = 2\pi r b \bar{v}_r \rho = \text{constant} \tag{B.10}$$

$\bar{v}_r$ written with respect to $\bar{v}_{ro} = \bar{v}_r(r = r_o)$. Note the velocity is negative since the flow is inward.

$$\bar{v}_r = -\frac{\bar{v}_{ro} r_o b_o}{rb} \tag{B.11}$$

Nondimensionalizing with respect to $-\bar{v}_{ro}$ gives

$$\bar{V}_r(R) = \frac{\bar{v}_r}{-\bar{v}_{ro}} = -\frac{1}{\beta R} \tag{B.12}$$

$$V_r(Z,R) = \frac{v_r}{-\bar{v}_{ro}} = -\frac{\phi}{\beta R} \tag{B.13}$$

Step 3: Use continuity to solve for v_z

The solution to the z-direction velocity, v_z can be found from solving the continuity equation:

$$\nabla \cdot \mathbf{v} = 0 \tag{B.14}$$

Equation (B.14) written in cylindrical coordinates, and with the assumptions from above reduces to

$$\frac{1}{r}\frac{\partial r v_r}{\partial r} + \frac{\partial v_z}{\partial z} \tag{B.15}$$

Using the following dimensionless parameters

$$Z = \frac{z}{b_o} \tag{B.16}$$

$$\varepsilon = \frac{b_o}{r_o} \tag{B.17}$$

$$V_z = \frac{v_z}{-\bar{v}_{ro}} \tag{B.18}$$

Eq. (B.15) can be nondimensionalized as

$$\frac{1}{R}\frac{\partial (R V_r)}{\partial R} + \frac{1}{\varepsilon}\frac{\partial V_z}{\partial Z} = 0 \tag{B.19}$$

Differentiating the first term gives

$$\frac{3}{2R}\left(\frac{12\alpha Z^2}{\beta^4} - \frac{\alpha}{\beta^2}\right) - \frac{1}{\varepsilon}\frac{\partial V_z}{\partial Z} = 0 \tag{B.20}$$

Integrating to solve for V_z

$$V_z = \int \frac{3\varepsilon}{2R}\left(\frac{12\alpha Z^2}{\beta^4} - \frac{\alpha}{\beta^2}\right) dZ \tag{B.21}$$

Becomes

$$V_z = -\frac{\alpha\varepsilon Z}{\beta^2 R}\frac{3}{2}\left[1 - \left(\frac{2Z}{\beta}\right)^2\right] + C(R) \tag{B.22}$$

Where $C(R)$ is a constant as a function of R. Simplifying further gives

$$V_z = -\frac{\alpha\varepsilon Z}{\beta^2 R}\phi + C(R) \tag{B.23}$$

Using the boundary condition of symmetry:

$$V_z(Z = 0) = 0 \tag{B.24}$$

gives $C(r) = 0$. Then can rewrite V_z as

$$V_z(Z, R) = -\frac{\alpha\varepsilon Z\phi}{\beta^2 R} \tag{B.25}$$

or in terms of V_r

$$V_z(Z, R) = \frac{\alpha\varepsilon Z V_r}{\beta} \tag{B.26}$$

Note ε is $<< 1$, whereas all other nondimensional parameters are of order 1, so this relation shows V_z is much smalller than V_r.

Step 4: Use θ-dir momentum equation to solve for v_θ

From Navier-Stokes, using the assumptions above the θ-direction momentum balance can be written as

$$v_r \frac{\partial v_\theta}{\partial r} + v_z \frac{\partial v_\theta}{\partial z} + \frac{v_r v_\theta}{r} = \nu \left[\frac{1}{r} \frac{\partial}{\partial r} \left(r \frac{\partial v_\theta}{\partial r} \right) + \frac{\partial^2 v_\theta}{\partial z^2} - \frac{v_\theta}{r^2} \right] \tag{B.27}$$

Defining

$$V_\theta = \frac{v_\theta}{|\bar{v}_{\theta,o}|} \tag{B.28}$$

$$W = \frac{|\bar{v}_{\theta,o}|}{-\bar{v}_{ro}} \tag{B.29}$$

$$\mathrm{Re_{r,o}} = \frac{-\bar{v}_{ro} 2 b_o}{\nu} \tag{B.30}$$

$$\mathrm{Re_m} = \mathrm{Re_{r,o}} \varepsilon \tag{B.31}$$

where $\bar{v}_{\theta,o} = \bar{v}_\theta(r = r_o)$. Nondimensionalizing Eq. (B.27) and substituting for V_z

$$V_r \frac{\partial V_\theta}{\partial R} + \frac{\alpha Z}{\beta} V_r \frac{\partial V_\theta}{\partial Z} + \frac{V_r V_\theta}{R} = \frac{2\varepsilon}{\mathrm{Re_{r,o}}} \left[\frac{1}{R} \frac{\partial}{\partial R} \left(R \frac{\partial V_\theta}{\partial R} \right) + \frac{1}{\varepsilon^2} \frac{\partial^2 V_\theta}{\partial Z^2} - \frac{V_\theta}{R^2} \right] \tag{B.32}$$

For the current design, $\mathrm{Re_{r,o}}$ will likely fall in the range of (10-1000), and ε will likely fall into the range of (0.01 - 0.1). Thus, the second term on the right hand side (RHS) of Eq. (B.32) is of order $1/(\varepsilon \mathrm{Re_{r,o}}) = O(1/10 - 100)$, and the first and third terms on the RHS of Eq. (B.32) are of order $\varepsilon/\mathrm{Re_{r,o}} = O(10^{-5} - 0.1)$. The terms on the left hand side (LHS) of Eq. (B.32) are all of O(α) or O(1). Thus, keeping all terms on the LHS, the first and third terms of the RHS can be neglected and the second term must be kept. This results in

$$V_r \frac{\partial V_\theta}{\partial R} + \frac{\alpha Z}{\beta} V_r \frac{\partial V_\theta}{\partial Z} + \frac{V_r V_\theta}{R} = \frac{2}{\varepsilon \mathrm{Re_{r,o}}} \frac{\partial^2 V_\theta}{\partial Z^2} \tag{B.33}$$

Substituting for V_r and V_θ and factoring out gives

$$\phi^2 \bar{V}_r \frac{\partial \bar{V}_\theta}{\partial R} + \phi \bar{V}_r \bar{V}_\theta \frac{\partial \phi}{\partial R} + \frac{\alpha Z \phi}{\beta} \bar{V}_r \bar{V}_\theta \frac{\partial \phi}{\partial Z} + \frac{\phi^2 \bar{V}_r \bar{V}_\theta}{R} = \frac{2\bar{V}_\theta}{\varepsilon \mathrm{Re_{r,o}}} \frac{\partial^2 \phi}{\partial Z^2} \tag{B.34}$$

Noting second and third terms cancel out, i.e.

$$\phi \bar{V}_r \bar{V}_\theta \left[\frac{\partial \phi}{\partial R} + \frac{\alpha Z}{\beta} \frac{\partial \phi}{\partial Z} \right] = 0 \tag{B.35}$$

Then the governing equation reduces to

$$\phi^2 \bar{V}_r \frac{\partial \bar{V}_\theta}{\partial R} + \frac{\phi^2 \bar{V}_r \bar{V}_\theta}{R} = \frac{2\bar{V}_\theta}{\varepsilon \mathrm{Re_{r,o}}} \frac{\partial^2 \phi}{\partial Z^2} \tag{B.36}$$

Using:

$$\frac{1}{\beta}\int_{-\beta/2}^{\beta/2}\phi^2 dZ = \frac{6}{5} \tag{B.37}$$

$$\frac{1}{\beta}\int_{-\beta/2}^{\beta/2}\frac{\partial^2\phi}{\partial Z^2}dZ = \frac{1}{\beta}\left.\frac{\partial\phi}{\partial Z}\right|_{-\beta/2}^{\beta/2} = -\frac{12}{\beta^2} \tag{B.38}$$

Integrating both sides from $-\beta/2$ to $\beta/2$ over dZ and dividing by β gives

$$\frac{6}{5}\left(\bar{V}_r\frac{\partial\bar{V}_\theta}{\partial R} + \frac{\bar{V}_r\bar{V}_\theta}{R}\right) = -\frac{24\bar{V}_\theta}{\mathrm{Re}_{\mathrm{r,o}}\varepsilon\beta^2} \tag{B.39}$$

Rearranging to solve for $\bar{V}_\theta$ and substituting in from Eq.(B.12)

$$\frac{\partial\bar{V}_\theta}{\partial R} = \left(\frac{20R}{\mathrm{Re}_{\mathrm{r,o}}\varepsilon\beta} - \frac{1}{R}\right)\bar{V}_\theta \tag{B.40}$$

Substituting in from Eq.(B.9) and integrating over R

$$\ln(\bar{V}_\theta) = -\ln(R) + \frac{20}{\mathrm{Re}_{\mathrm{r,o}}\varepsilon}\int\frac{R}{\alpha R + 1 - \alpha}dR \tag{B.41}$$

Which becomes

$$\ln(\bar{V}_\theta) = -\ln(R) + \frac{20}{\mathrm{Re}_{\mathrm{r,o}}\varepsilon}\left[\frac{R}{\alpha} + \ln(\alpha R + 1 - \alpha)\frac{\alpha - 1}{\alpha^2}\right] + C \tag{B.42}$$

where C is an unknown constant. Solving for $\bar{V}_\theta$

$$\bar{V}_\theta = \frac{C_0}{R}\exp\left[\frac{20R}{\mathrm{Re}_{\mathrm{r,o}}\varepsilon\alpha}\right]\beta^{\frac{20(\alpha-1)}{\mathrm{Re}_{\mathrm{r,o}}\varepsilon\alpha^2}} \tag{B.43}$$

where C_0 is an unknown constant. Using the boundary condition that $\bar{V}_\theta(R = 1) = 1$ gives

$$C_0 = \exp\left[-\frac{20}{\mathrm{Re}_{\mathrm{r,o}}\varepsilon\alpha}\right] \tag{B.44}$$

So the final form of $\bar{V}_\theta$ can be written as

$$\bar{V}_\theta(R) = \frac{1}{R}\exp\left[\frac{20(R-1)}{\mathrm{Re}_{\mathrm{r,o}}\varepsilon\alpha}\right]\beta^{\frac{20(\alpha-1)}{\mathrm{Re}_{\mathrm{r,o}}\varepsilon\alpha^2}} \tag{B.45}$$

Step 5: Use r-dir momentum equation to solve for pressure distribution

From Navier-Stokes, using the assumptions above the r-direction momentum balance can be written as

$$v_r \frac{\partial v_r}{\partial r} + v_z \frac{\partial v_r}{\partial z} - \frac{v_\theta^2}{r} = -\frac{1}{\rho}\left(\frac{\partial P}{\partial r}\right) + \nu\left[\frac{1}{r}\frac{\partial}{\partial r}\left(r\frac{\partial v_r}{\partial r}\right) + \frac{\partial^2 v_r}{\partial z^2} - \frac{v_r}{r^2}\right] \tag{B.46}$$

Nondimensionalize using the velocity in the θ direction which is likely the dominant velocity

$$P^* = \frac{P}{\rho v_{\theta,o}^2} \tag{B.47}$$

gives

$$\begin{split} \frac{V_r}{W^2}\frac{\partial V_r}{\partial R} + \frac{V_z}{\varepsilon W^2}\frac{\partial V_r}{\partial Z} - \frac{V_\theta^2}{R} = \\ -\frac{\partial P^*}{\partial R} + \frac{2\varepsilon}{W^2 \mathrm{Re_{r,o}}}\left[\frac{1}{R}\frac{\partial}{\partial R}\left(R\frac{\partial V_r}{\partial R}\right) + \frac{1}{\varepsilon^2}\frac{\partial^2 V_r}{\partial Z^2} - \frac{V_r}{R^2}\right] \end{split} \tag{B.48}$$

Using similar arguments from the previous section on the orders of Re and ε and multiplying through by W^2. The third term on the right hand side (RHS) of Eq. (B.48) is of order $1/(\varepsilon \mathrm{Re_{r,o}}) = O(1/10 - 100)$, and the second and fourth terms on the RHS of Eq. (B.48) are of order $\varepsilon/\mathrm{Re_{r,o}} = O(10^{-5} - 0.1)$. The terms on the LHS of Eq. (B.48) are all of O(α), O(W^2) or O(1). Thus, keeping all terms on the LHS, the second and fourth terms of the RHS can be neglected and the third term must be kept. This results in

$$\frac{V_r}{W^2}\frac{\partial V_r}{\partial R} + \frac{\alpha Z V_r}{\beta W^2}\frac{\partial V_r}{\partial Z} - \frac{V_\theta^2}{R} = -\frac{\partial P^*}{\partial R} + \frac{2\varepsilon}{W^2 \mathrm{Re_{r,o}}}\frac{1}{\varepsilon^2}\frac{\partial^2 V_r}{\partial Z^2} \tag{B.49}$$

Rewriting in terms of ϕ

$$\frac{\phi^2 \bar{V}_r}{W^2}\frac{\partial \bar{V}_r}{\partial R} + \frac{\phi \bar{V}_r^2}{W^2}\frac{\partial \phi}{\partial R} + \frac{\alpha Z \phi \bar{V}_r^2}{\beta W^2}\frac{\partial \phi}{\partial Z} - \frac{\phi^2 \bar{V}_\theta^2}{R} = -\frac{\partial P^*}{\partial R} + \frac{2\bar{V}_r}{W^2 \mathrm{Re_{r,o}}\varepsilon}\frac{\partial^2 \phi}{\partial Z^2} \tag{B.50}$$

Noting from Eq. (B.35), second and third terms on the LHS cancel. Using the values from Eqs. (B.37-B.38), integrating both sides from $-\beta/2$ to $\beta/2$ over dZ and dividing by β yields:

$$\frac{6}{5}\left(\frac{\bar{V}_r}{W^2}\frac{\partial \bar{V}_r}{\partial R} - \frac{\bar{V}_\theta^2}{R}\right) = -\frac{1}{\beta}\int_{-\beta/2}^{\beta/2}\frac{\partial P^*}{\partial R}dZ - \frac{24\bar{V}_r}{W^2 \mathrm{Re_{r,o}}\varepsilon\beta^2} \tag{B.51}$$

Defining an average pressure over the surface

$$\bar{P}^* = \frac{1}{\beta}\int_{-\beta/2}^{\beta/2} P^* dZ \tag{B.52}$$

Using Leibniz rule and symmetry the first term on the RHS of Eq. (B.51) becomes

$$\begin{aligned} -\frac{1}{\beta}\int_{-\beta/2}^{\beta/2}\frac{\partial P^*}{\partial R}dZ &= -\frac{1}{\beta}\left[\frac{\partial}{\partial R}\int_{-\beta/2}^{\beta/2}P^* dZ - \frac{\alpha}{2}P^*(\frac{\beta}{2},R) - \frac{\alpha}{2}P^*(-\frac{\beta}{2},R)\right] \\ &= -\frac{1}{\beta}\left[\frac{\partial}{\partial R}(\bar{P}^*\beta) - \alpha P^*(\frac{\beta}{2},R)\right] \end{aligned} \tag{B.53}$$

Noting that pressure does not vary much with z location in the heat sink, the z-direction momentum equation can show this to be true, thus

$$\frac{\partial P^*}{\partial Z} \sim \mathrm{O}[\varepsilon]$$

Then, the Taylor expansion of P^* shows

$$\begin{aligned} P^*(\beta/2,R) &\approx P^*(0,R) + \frac{\beta}{2}\left.\frac{\partial P^*}{\partial Z}\right|_{Z=0} \\ &\approx P^*(0,R) \\ &\approx \bar{P}^*(R) \end{aligned} \tag{B.54}$$

Substituting into Eq. (B.53) gives

$$-\frac{1}{\beta}\int_{-\beta/2}^{\beta/2}\frac{\partial P^*}{\partial R}dZ = -\frac{\partial \bar{P}^*}{\partial R} - \frac{\alpha\bar{P}^*}{\beta} + \frac{\alpha\bar{P}^*}{\beta} \tag{B.55}$$

and noting the last two terms cancel, Eq. (B.51) becomes

$$\frac{6}{5}\left(\frac{\bar{V}_r}{W^2}\frac{\partial \bar{V}_r}{\partial R} - \frac{\bar{V}_\theta^2}{R}\right) = -\frac{\partial \bar{P}^*}{\partial R} - \frac{24\bar{V}_r}{W^2\mathrm{Re}_{\mathrm{r,o}}\varepsilon\beta^2} \tag{B.56}$$

Integrating over R to solve for $\bar{P}^*(R)$

$$\bar{P}^*(1) - \bar{P}^*(R) = \int_R^1 \left[\frac{6}{5}\left(-\frac{\bar{V}_r}{W^2}\frac{\partial \bar{V}_r}{\partial \varsigma} + \frac{\bar{V}_\theta^2}{\varsigma}\right) - \frac{24\bar{V}_r}{W^2\mathrm{Re}_{\mathrm{r,o}}\varepsilon\beta^2}\right] d\varsigma \tag{B.57}$$

where ς is a dummy variable of integration. The total pressure drop across the entire channel can be found by integrating from R_i to 1. So that the final total pressure drop is given by $\Delta\bar{P}^*_{tot} = \bar{P}^*(1) - \bar{P}^*(R_i)$ or

$$\Delta\bar{P}^*_{tot} = \int_{R_i}^1 \left[\frac{6}{5}\left(-\frac{\bar{V}_r}{W^2}\frac{\partial \bar{V}_r}{\partial R} + \frac{\bar{V}_\theta^2}{R}\right) - \frac{24\bar{V}_r}{W^2\mathrm{Re}_{\mathrm{r,o}}\varepsilon\beta^2}\right] dR \tag{B.58}$$

B.2 Derivation of Velocity and Pressure Distributions for Constant Gap Size

In order to solve for the velocity and pressure distributions in the heat sink, the continuity and momentum equations must be solved. The following presents the full derivation of the velocities in the r, θ directions as well as the total average pressure drop across the channel. The following assumptions are made:

- The flow is steady, incompressible, and has constant fluid properties.
- The flow is laminar. The use of microchannels results in small Reynolds numbers.
- The flow is axisymmetric, therefore, all θ derivatives of flow quantities are zero.
- No entrance or exit effects are considered.
- The flow length, r_o, is much larger than the gap size, b, so that $b/r_o << 1$
- Because the gap size is not varying, $v_z = 0$

Step 1: Postulate velocity profiles

The following parabolic solutions are postulated for the radial and tangential velocities

$$v_r = \bar{v}_r(r)\phi(z) \tag{B.59}$$

$$v_\theta = \bar{v}_\theta(r)\phi(z) \tag{B.60}$$

where

$$\phi(z) = \frac{3}{2}\left[1 - \left(\frac{2z}{b}\right)^2\right] \tag{B.61}$$

and $\bar{v}_r$ and $\bar{v}_\theta$ are mean velocities defined as

$$\bar{v}_r(r) = \frac{1}{b}\int_{-b/2}^{b/2} v_r dz \tag{B.62}$$

$$\bar{v}_\theta(r) = \frac{1}{b}\int_{-b/2}^{b/2} v_\theta dz \tag{B.63}$$

Step 2: Use mass conservation to solve for v_r

Knowing the mass flux is constant through any crossectional disk

$$\dot{m} = 2\pi r b \bar{v}_r \rho = \text{constant} \tag{B.64}$$

$\bar{v}_r$ can be found with respect to $\bar{v}_{ro} = \bar{v}_r(r = r_o)$. Note the velocity is negative since the flow is inward.

$$\bar{v}_r = -\frac{\bar{v}_{ro} r_o}{r} \tag{B.65}$$

Denoting

$$R = r/r_o \tag{B.66}$$

Nondimensionalizing with respect to $-\bar{v}_{ro}$ gives

$$\bar{V}_r(R) = \frac{\bar{v}_r}{-\bar{v}_{ro}} = -\frac{1}{R} \tag{B.67}$$

$$V_r(Z, R) = \frac{v_r}{-\bar{v}_{ro}} = -\frac{\phi}{R} \tag{B.68}$$

Step 3: Use θ-dir momentum equation to solve for v_θ

From Navier-Stokes, using the assumptions above the θ-direction momentum balance can be written as

$$v_r \frac{\partial v_\theta}{\partial r} + \frac{v_r v_\theta}{r} = \nu \left[\frac{1}{r} \frac{\partial}{\partial r} \left(r \frac{\partial v_\theta}{\partial r} \right) + \frac{\partial^2 v_\theta}{\partial z^2} - \frac{v_\theta}{r^2} \right] \tag{B.69}$$

Defining

$$V_\theta = \frac{v_\theta}{|\bar{v}_{\theta,o}|} \tag{B.70}$$

$$W = \frac{|\bar{v}_{\theta,o}|}{-\bar{v}_{ro}} \tag{B.71}$$

$$\mathrm{Re}_{\mathrm{r,o}} = \frac{-\bar{v}_{ro} 2b}{\nu} \tag{B.72}$$

where $\bar{v}_{\theta,o} = \bar{v}_\theta(r = r_o)$. Nondimensionalizing Eq. (B.69)

$$V_r \frac{\partial V_\theta}{\partial R} + \frac{V_r V_\theta}{R} = \frac{2\varepsilon}{\mathrm{Re}_{\mathrm{r,o}}} \left[\frac{1}{R} \frac{\partial}{\partial R} \left(R \frac{\partial V_\theta}{\partial R} \right) + \frac{1}{\varepsilon^2} \frac{\partial^2 V_\theta}{\partial Z^2} - \frac{V_\theta}{R^2} \right] \tag{B.73}$$

For the current design, $\mathrm{Re}_{\mathrm{r,o}}$ will likely fall in the range of (10-1000), and ε will likely fall into the range of (0.01 - 0.1). Thus, the second term on the right hand side (RHS) of Eq. (B.73) is of order $1/(\varepsilon \mathrm{Re}_{\mathrm{r,o}}) = O(1/10 - 100)$, and the first and third terms on the RHS of Eq. (B.73) are of order $\varepsilon/\mathrm{Re}_{\mathrm{r,o}} = O(10^{-5} - 0.1)$. The terms on the left hand side (LHS) of Eq. (B.73) are all of O(1). Thus, keeping all terms on the LHS, the first and third terms of the RHS can be neglected and the second term must be kept. This results in

$$V_r \frac{\partial V_\theta}{\partial R} + \frac{V_r V_\theta}{R} = \frac{2}{\varepsilon \mathrm{Re}_{\mathrm{r,o}}} \frac{\partial^2 V_\theta}{\partial Z^2} \tag{B.74}$$

Substituting for V_r and V_θ and factoring out gives

$$\phi^2 \bar{V}_r \frac{\partial \bar{V}_\theta}{\partial R} + \frac{\phi^2 \bar{V}_r \bar{V}_\theta}{R} = \frac{2\bar{V}_\theta}{\varepsilon \mathrm{Re}_{\mathrm{r,o}}} \frac{\partial^2 \phi}{\partial Z^2} \tag{B.75}$$

Using:

$$\int_{-1/2}^{1/2} \phi^2 dZ = \frac{6}{5} \tag{B.76}$$

$$\int_{-1/2}^{1/2} \frac{\partial^2 \phi}{\partial Z^2} dZ = \left. \frac{\partial \phi}{\partial Z} \right|_{-1/2}^{1/2} = -12 \tag{B.77}$$

Integrating both sides from $-1/2$ to $1/2$ over dZ gives

$$\frac{6}{5} \left(\bar{V}_r \frac{\partial \bar{V}_\theta}{\partial R} + \frac{\bar{V}_r \bar{V}_\theta}{R} \right) = -\frac{24\bar{V}_\theta}{\varepsilon \mathrm{Re}_{\mathrm{r,o}}} \tag{B.78}$$

Rearranging to solve for $\bar{V}_\theta$ and substituting in from Eq.(B.67)

$$\frac{\partial \bar{V}_\theta}{\partial R} = \left(\frac{20R}{\mathrm{Re}_{\mathrm{r,o}} \varepsilon} - \frac{1}{R} \right) \bar{V}_\theta \tag{B.79}$$

Integrating over R

$$\ln(\bar{V}_\theta) = -\ln(R) + \frac{10R^2}{\mathrm{Re}_{\mathrm{r,o}} \varepsilon} + C \tag{B.80}$$

where C is an unknown constant. Solving for $\bar{V}_\theta$

$$\bar{V}_\theta = \frac{C_0}{R} \exp\left[\frac{10R^2}{\mathrm{Re}_{\mathrm{r,o}} \varepsilon} \right] \tag{B.81}$$

where C_0 is an unknown constant. Using the boundary condition that $\bar{V}_\theta(R = 1) = 1$ gives

$$C_0 = \exp\left[-\frac{10}{\mathrm{Re}_{\mathrm{r,o}} \varepsilon} \right] \tag{B.82}$$

So the final form of $\bar{V}_\theta$ can be written as

$$\bar{V}_\theta(R) = \frac{1}{R} \exp\left[\frac{10(R^2 - 1)}{\mathrm{Re}_{\mathrm{r,o}} \varepsilon} \right] \tag{B.83}$$

Step 4: Use r-dir momentum equation to solve for pressure distribution

From Navier-Stokes, using the assumptions above the r-direction momentum balance can be written as

$$v_r \frac{\partial v_r}{\partial r} - \frac{v_\theta^2}{r} = -\frac{1}{\rho}\left(\frac{\partial P}{\partial r}\right) + \nu\left[\frac{1}{r}\frac{\partial}{\partial r}\left(r\frac{\partial v_r}{\partial r}\right) + \frac{\partial^2 v_r}{\partial z^2} - \frac{v_r}{r^2}\right] \tag{B.84}$$

Nondimensionalize using the velocity in the θ direction which is likely the dominant velocity

$$P^* = \frac{P}{\rho v_{\theta,o}^2} \tag{B.85}$$

gives

$$\frac{V_r}{W^2}\frac{\partial V_r}{\partial R} - \frac{V_\theta^2}{R} = -\frac{\partial P^*}{\partial R} + \frac{2\varepsilon}{W^2 \mathrm{Re}_{\mathrm{r,o}}}\left[\frac{1}{R}\frac{\partial}{\partial R}\left(R\frac{\partial V_r}{\partial R}\right) + \frac{1}{\varepsilon^2}\frac{\partial^2 V_r}{\partial Z^2} - \frac{V_r}{R^2}\right] \tag{B.86}$$

Using similar arguments from the previous section on the orders of Re and ε and multiplying through by W^2. The third term on the right hand side (RHS) of Eq. (B.86) is of order $1/(\varepsilon \mathrm{Re}_{\mathrm{r,o}}) = O(1/10 - 100)$, and the second and fourth terms on the RHS of Eq. (B.86) are of order $\varepsilon/\mathrm{Re}_{\mathrm{r,o}} = O(10^{-5} - 0.1)$. The terms on the LHS of Eq. (B.86) are all of O(W^2) or O(1). Thus, keeping all terms on the LHS, the second and fourth terms of the RHS can be neglected and the third term must be kept. This results in

$$\frac{V_r}{W^2}\frac{\partial V_r}{\partial R} - \frac{V_\theta^2}{R} = -\frac{\partial P^*}{\partial R} + \frac{2\varepsilon}{W^2 \mathrm{Re}_{\mathrm{r,o}}}\frac{1}{\varepsilon^2}\frac{\partial^2 V_r}{\partial Z^2} \tag{B.87}$$

Rewriting in terms of ϕ

$$\frac{\phi^2 \bar{V}_r}{W^2}\frac{\partial \bar{V}_r}{\partial R} - \frac{\phi^2 \bar{V}_\theta^2}{R} = -\frac{\partial P^*}{\partial R} + \frac{2\bar{V}_r}{W^2 \mathrm{Re}_{\mathrm{r,o}}\varepsilon}\frac{\partial^2 \phi}{\partial Z^2} \tag{B.88}$$

Using the values from Eqs. (B.76-B.77), integrating both sides from $-1/2$ to $1/2$ over dZ yields:

$$\frac{6}{5}\left(\frac{\bar{V}_r}{W^2}\frac{\partial \bar{V}_r}{\partial R} - \frac{\bar{V}_\theta^2}{R}\right) = -\int_{-1/2}^{1/2}\frac{\partial P^*}{\partial R}dZ - \frac{24\bar{V}_r}{W^2 \mathrm{Re}_{\mathrm{r,o}}\varepsilon} \tag{B.89}$$

Defining an average pressure over the surface

$$\bar{P}^* = \int_{-1/2}^{1/2} P^* dZ \tag{B.90}$$

Eq. (B.89) becomes

$$\frac{6}{5}\left(\frac{\bar{V}_r}{W^2}\frac{\partial \bar{V}_r}{\partial R} - \frac{\bar{V}_\theta^2}{R}\right) = -\frac{\partial \bar{P}^*}{\partial R} - \frac{24\bar{V}_r}{W^2 \mathrm{Re}_{\mathrm{r,o}}\varepsilon} \tag{B.91}$$

Integrating over R to solve for $\bar{P}^*(R)$

$$\bar{P}^*(1) - \bar{P}^*(R) = \int_R^1 \left[\frac{6}{5} \left(-\frac{\bar{V}_r}{W^2} \frac{\partial \bar{V}_r}{\partial \varsigma} + \frac{\bar{V}_\theta^2}{\varsigma} \right) - \frac{24 \bar{V}_r}{W^2 \mathrm{Re}_{\mathrm{r,o}} \varepsilon} \right] d\varsigma \tag{B.92}$$

where ς is a dummy variable of integration. The total pressure drop across the entire channel can be found by integrating from R_i to 1. So that the final total pressure drop is given by $\Delta \bar{P}^*_{tot} = \bar{P}^*(1) - \bar{P}^*(R_i)$ or

$$\Delta \bar{P}^*_{tot} = \int_{R_i}^1 \left[\frac{6}{5} \left(-\frac{\bar{V}_r}{W^2} \frac{\partial \bar{V}_r}{\partial R} + \frac{\bar{V}_\theta^2}{R} \right) - \frac{24 \bar{V}_r}{W^2 \mathrm{Re}_{\mathrm{r,o}} \varepsilon} \right] dR \tag{B.93}$$

Substituting for $\bar{V}_r$ and integrating the first and last terms gives

$$\Delta \bar{P}^*_{tot} = \frac{6}{5} \int_{R_i}^1 \frac{\bar{V}_\theta^2}{R} dR + \frac{3}{5W^2} \left(\frac{1}{R_i^2} - 1 \right) - \frac{24}{W^2 \mathrm{Re}_{\mathrm{r,o}} \varepsilon} \ln[R_i] \tag{B.94}$$

B.3 Derivation of Flow Temperature and Wall Temperature Distributions for a Constant Wall Heat Flux

In order to solve for the temperature distributions in the heat sink, an analytical solution to the energy equation was made. The following presents the full derivation of the flow temperature and wall temperature distributions in the channel. The following assumptions are made:

- One wall is insulated and the other wall has a constant heat flux, q''_w
- The flow is steady and incompressible with velocity distributions given above.
- The fluid has constant properties: viscosity, thermal conductivity, density and specific heat
- The flow is axisymmetric, therefore, all θ derivatives of flow quantities are zero.
- There is negligible viscous dissipation, Φ, and no source contributions, S
- The flow length, r_o, is much larger than the gap size, b, so that $b/r_o << 1$

The generalized energy conservation equations can be written as:

$$\rho \frac{Di}{Dt} - \nabla \cdot k \nabla T - \mu \Phi - \frac{DP}{Dt} - S = 0 \tag{B.95}$$

Using the assumptions above, (B.95) becomes:

$$\rho v_r c_p \frac{\partial T}{\partial r} - \frac{k}{r}\frac{\partial}{\partial r}\left(r\frac{\partial T}{\partial r}\right) - k\frac{\partial^2 T}{\partial z^2} = 0 \tag{B.96}$$

With boundary conditions:

$$-k\left.\frac{\partial T}{\partial z}\right|_{-b/2} = q''_w \tag{B.97}$$

$$-k\left.\frac{\partial T}{\partial z}\right|_{b/2} = 0 \tag{B.98}$$

Using the following nondimensional parameters in addition to the parameters defined in App. B.1

$$\Theta = \frac{T - T_o}{T_{b,i} - T_o} \tag{B.99}$$

$$\mathrm{Pr} = \frac{\mu c_p}{k} \tag{B.100}$$

$$\mathrm{Pe_m} = \mathrm{Re_m Pr} \tag{B.101}$$

where Pr is the Prandtl number, Pe_m is a modified Peclet number, and T_b is the bulk fluid temperature defined by

$$T_b = \frac{1}{b\bar{v}_r}\int_{-b/2}^{b/2} v_r T dz \tag{B.102}$$

Eq. (B.96) can be written as

$$V_r\frac{\partial \Theta}{\partial R} - \frac{2\varepsilon^2}{\mathrm{Pe_m} R}\frac{\partial}{\partial R}\left(R\frac{\partial \Theta}{\partial R}\right) - \frac{2}{\mathrm{Pe_m}}\frac{\partial^2 \Theta}{\partial Z^2} = 0 \tag{B.103}$$

The second term above, representing the radial conduction, is of order $\varepsilon^2/\mathrm{Pe_m} << 1$. This term can be neglected when compared to the first and last terms, the radial advection and the axial conduction, respectively. So the governing equation becomes:

$$V_r\frac{\partial \Theta}{\partial R} - \frac{2}{\mathrm{Pe_m}}\frac{\partial^2 \Theta}{\partial Z^2} = 0 \tag{B.104}$$

The wall boundary conditions can be written as

$$\left.\frac{\partial \Theta}{\partial Z}\right|_{\beta/2} = 0 \tag{B.105}$$

$$-\left.\frac{\partial \Theta}{\partial Z}\right|_{-\beta/2} = \frac{q''_w b_o}{k(T_{b,i} - T_o)} \tag{B.106}$$

By using conservation of energy over the entire surface the boundary condition from Eq. (B.106) can be written as

$$-\left.\frac{\partial \Theta}{\partial Z}\right|_{-\beta/2} = \frac{q''_w b_o}{k(T_{b,i} - T_o)} = \frac{\mathrm{Pe_m}}{1 - R_i^2} \tag{B.107}$$

Thus, integrating Eq. (B.104) over $-\beta/2$ to $\beta/2$ and dividing by β

$$\frac{\bar{V}_r}{\beta} \int_{-\beta/2}^{\beta/2} \phi \frac{\partial \Theta}{\partial R} dZ - \frac{2}{\beta \mathrm{Pe_m}} \int_{-\beta/2}^{\beta/2} \frac{\partial^2 \Theta}{\partial Z^2} dZ = 0 \tag{B.108}$$

Substituting the boundary conditions from Eq. (B.105) and (B.107), the last term can be written as:

$$-\frac{2}{\beta \mathrm{Pe_m}} \left[\left.\frac{\partial \Theta}{\partial Z}\right|_{\beta/2} - \left.\frac{\partial \Theta}{\partial Z}\right|_{-\beta/2} \right] = -\frac{2}{\beta \mathrm{Pe_m}} \left[0 + \frac{\mathrm{Pe_m}}{1 - R_i^2} \right] \tag{B.109}$$

and the integrated energy equation becomes:

$$\frac{\bar{V}_r}{\beta} \int_{-\beta/2}^{\beta/2} \phi \frac{\partial \Theta}{\partial R} dZ - \frac{2}{\beta(1 - R_i^2)} = 0 \tag{B.110}$$

which, by chain rule, becomes:

$$\frac{\bar{V}_r}{\beta} \left(\int_{-\beta/2}^{\beta/2} \left(\frac{\partial \phi \Theta}{\partial R} - \Theta \frac{\partial \phi}{\partial R} \right) dZ \right) - \frac{2}{\beta(1 - R_i^2)} = 0 \tag{B.111}$$

Using the fact that

$$\Theta_b = \frac{1}{\beta} \int_{-\beta/2}^{\beta/2} \phi \Theta dZ \tag{B.112}$$

and applying Leibniz Rule, the term in the integral of (B.111) becomes

$$\frac{\partial \beta \Theta_b}{\partial R} - \frac{1}{2} \frac{\partial \beta}{\partial R} \left.(\Theta \phi)\right|_{\beta/2} - \frac{1}{2} \frac{\partial \beta}{\partial R} \left.(\Theta \phi)\right|_{-\beta/2} - \int_{-\beta/2}^{\beta/2} \Theta \frac{\partial \phi}{\partial R} dZ \tag{B.113}$$

noting $\phi|_{\beta/2,-\beta/2} = 0$, and that $\frac{\partial \phi}{\partial R}$ is of O$[\alpha]$ and assuming the device is designed with a small gap slope, $\alpha << 1$ so that the terms of O$[\alpha]$ can be neglected, results in

$$\bar{V}_r \frac{\partial \Theta_b}{\partial R} - \frac{2}{\beta(1 - R_i^2)} = 0 \tag{B.114}$$

and substituting for the solution for $\bar{V}_r$ from Eq. (B.12) gives:

$$\frac{\partial \Theta_b}{\partial R} = -\frac{2R}{(1 - R_i^2)} \tag{B.115}$$

Solving for Θ_b and using the boundary condition that $\Theta_b(R=1)=0$, results in

$$\Theta_b(R) = \frac{1-R^2}{1-R_i^2} \tag{B.116}$$

This is the same solution that can be derived from an energy balance on the whole system:

$$q''_w \pi (r_o^2 - r^2) = \dot{m} c_p \left(T_b(r) - T_o\right) \tag{B.117}$$

To solve for the wall temperatures, it is assumed that the Nusselt number, Nu, for the flow is constant. Where

$$\mathrm{Nu} = \frac{h(2b)}{k} \tag{B.118}$$

and the temperature can be found from the constant wall heat flux

$$q''_w = h(T_w - T_b) \tag{B.119}$$

Defining a dimensionless wall temperature based on the heat flux, q''_w,

$$\Theta_w(R) = \frac{h(T_w(R) - T_o)}{q''_w} \tag{B.120}$$

allows computation of T_w in dimensionless form as

$$\Theta_w(R) = \frac{(1-R^2)\mathrm{Nu}}{2\mathrm{Pe_m}\beta} + 1 \tag{B.121}$$

If the gap size is constant, $\beta = 1$, and the solution becomes

$$\Theta_w(R) = \frac{(1-R^2)\mathrm{Nu}}{2\mathrm{Pe_m}} + 1 \tag{B.122}$$

B.4 Derivation of Flow Temperature and Wall Heat Flux Distributions for a Constant Wall Temperature

Using the same assumptions as above except assuming the bottom wall is now subject to a constant wall temperature condition, the energy equation can be solved by replacing the boundary condition in Eq. (B.106) with:

$$-k \left.\frac{\partial T}{\partial z}\right|_{-\beta/2} = h(T_w - T_b) \tag{B.123}$$

and in terms of nondimensional parameters:

$$\left.\frac{\partial \Theta}{\partial Z}\right|_{-\beta/2} = \frac{\mathrm{Nu}}{2\beta}\Theta_{b,T} \tag{B.124}$$

using a normalized bulk temperature:

$$\Theta_{b,T}(R) = \frac{T_b(R) - T_w}{T_o - T_w} \tag{B.125}$$

Starting with the same governing equation (B.104) and making the same assumptions as in the previous section the governing equation can then be written as:

$$\bar{V_r}\frac{\partial \Theta_{b,T}}{\partial R} + \frac{2}{\beta \mathrm{Pe_m}}\left.\frac{\partial \Theta_T}{\partial Z}\right|_{-\beta/2} = 0 \tag{B.126}$$

and substituting the second boundary condition from Eq. (B.124) and substituting for the definition of $\bar{V_r} = -1/(\beta R)$:

$$\frac{\partial \Theta_{b,T}}{\partial R} + \frac{\mathrm{Nu}R}{\mathrm{Pe_m}\beta}\Theta_{b,T} \tag{B.127}$$

This is a first order ODE that can be solved by direct integration and using the boundary condition $\Theta_{b,T}|_{(R=1)} = 1$, resulting in:

$$\Theta_{b,T}(R) = \beta^{\frac{(\alpha-1)\mathrm{Nu}}{\alpha^2\mathrm{Pe_m}}}\exp\left[\frac{\mathrm{Nu}}{\mathrm{Pe_m}\alpha}(R-1)\right] \tag{B.128}$$

If the gap size is constant the solution is

$$\Theta_{b,T}(R) = \exp\left[\frac{\mathrm{Nu}}{2\mathrm{Pe_m}}(R^2-1)\right] \tag{B.129}$$

The total heat flux along the wall can be found by solving for

$$q''_w(R) = h(T_w - T_{b,T}) \tag{B.130}$$

or

$$q''_w(R) = h\Theta_{b,T}(T_w - T_o) \tag{B.131}$$

Appendix C

Device Fabrication Schematic

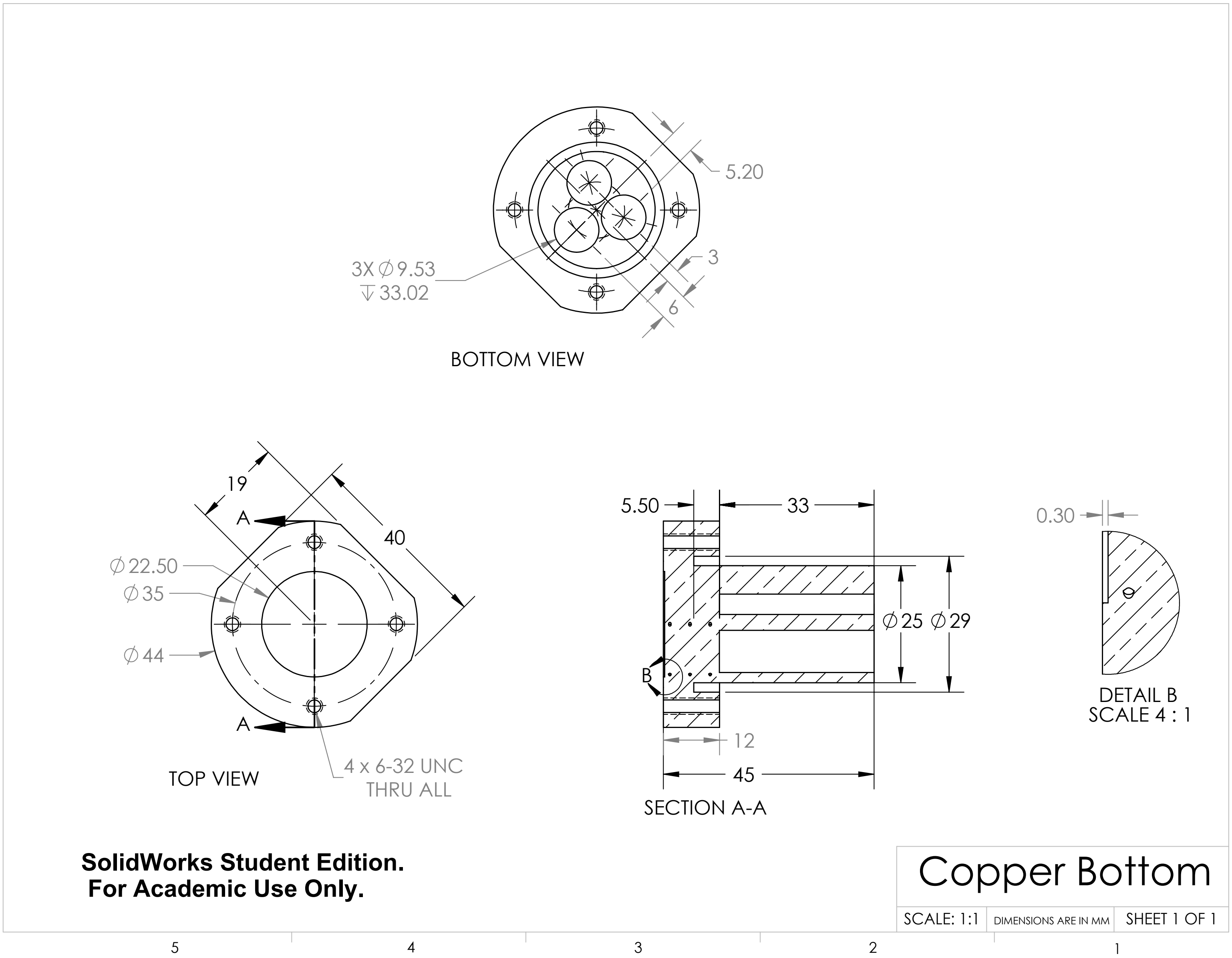
5.20
3X ⌀ 9.53
↧ 33.02
3
6
BOTTOM VIEW
19
A
40
⌀ 22.50
⌀ 35
⌀ 44
A
4 x 6-32 UNC
THRU ALL
TOP VIEW
5.50
33
⌀ 25
⌀ 29
B
12
45
SECTION A-A
0.30
DETAIL B
SCALE 4 : 1
Copper Bottom
SCALE: 1:1
DIMENSIONS ARE IN MM
SHEET 1 OF 1
5
4
3
2
1

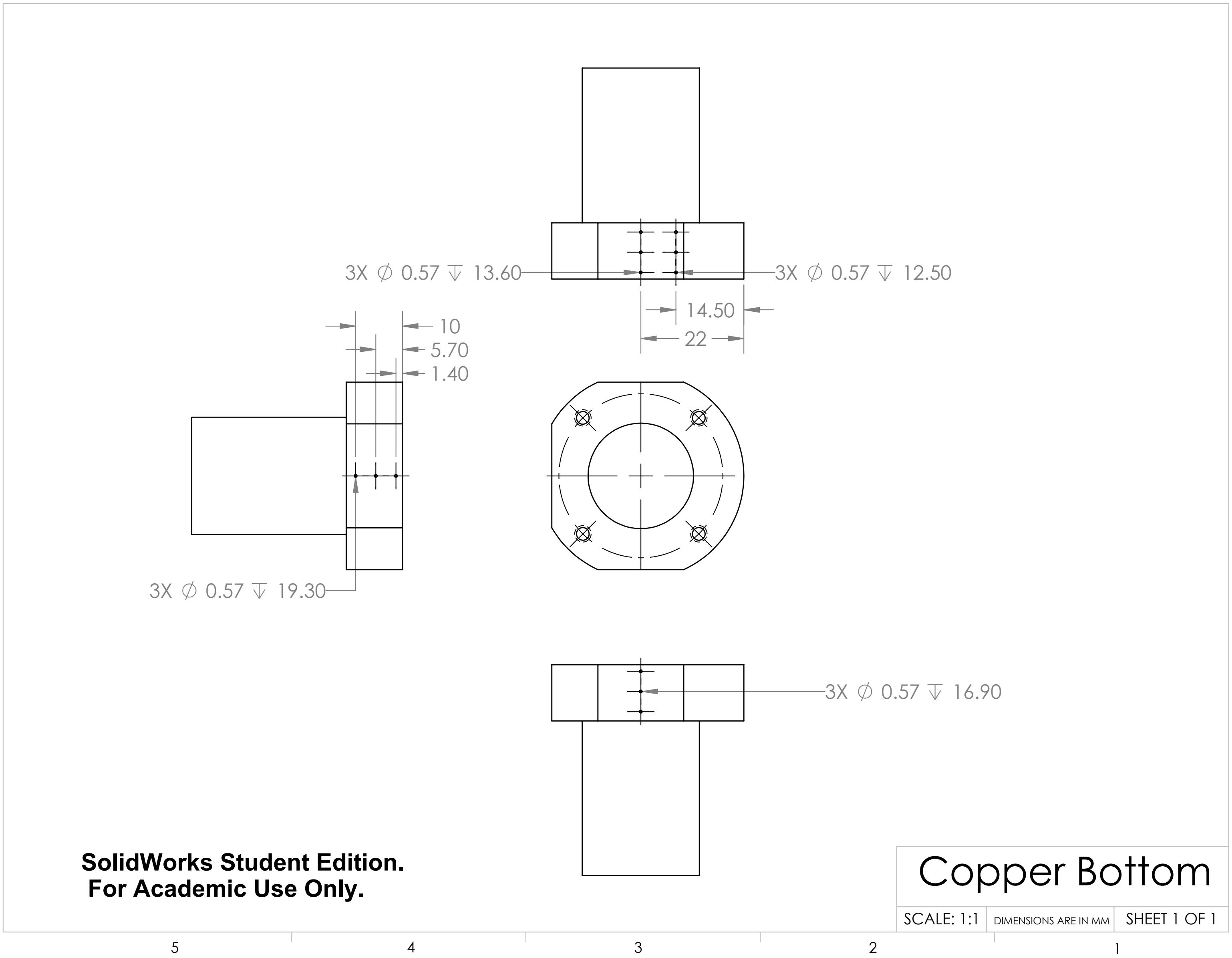
3X ∅ 0.57 ↧ 13.60
3X ∅ 0.57 ↧ 12.50
14.50
22
10
5.70
1.40
3X ∅ 0.57 ↧ 19.30
3X ∅ 0.57 ↧ 16.90
SolidWorks Student Edition.
For Academic Use Only.
Copper Bottom
SCALE: 1:1
DIMENSIONS ARE IN MM
SHEET 1 OF 1
5
4
3
2
1

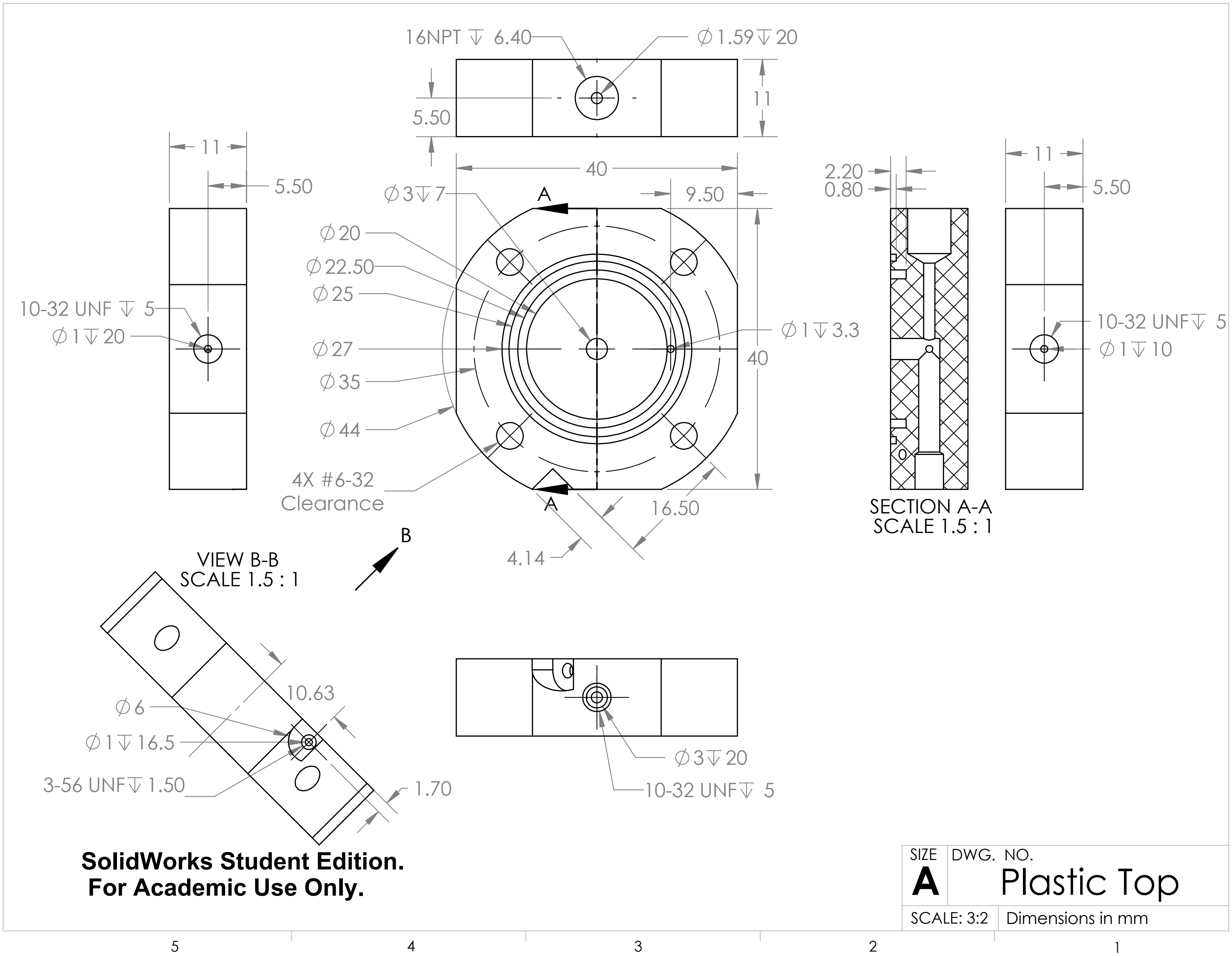
16NPT ↧ 6.40
∅1.59↧20
5.50
11
11
5.50
40
∅3↧7
A
9.50
∅20
∅22.50
∅25
10-32 UNF ↧ 5
∅1↧20
∅27
∅35
∅44
4X #6-32
Clearance
A
∅1↧3.3
40
16.50
4.14
2.20
0.80
11
5.50
10-32 UNF↧ 5
∅1↧10
SECTION A-A
SCALE 1.5 : 1
B
VIEW B-B
SCALE 1.5 : 1
10.63
∅6
∅1↧16.5
3-56 UNF↧1.50
1.70
∅3↧20
10-32 UNF↧ 5
SolidWorks Student Edition.
For Academic Use Only.
SIZE
A
DWG. NO.
Plastic Top
SCALE: 3:2
Dimensions in mm
5
4
3
2
1

Appendix D

Uncertainty Analysis

In order to calculate the error associated with each experimental measurement used in this study, the accuracy of the instrumentation shown in Table 4.3 was used to calculate a total uncertainty. For each measurement the general formula for error propagation was used:

$$e_{f(x_1,x_2,...)} = \sqrt{\sum_{i=1}^{n} (\frac{df}{dx_i} e_{x_i})^2} \tag{D.1}$$

Where e_f indicates the absolute error associated with variable f which is a function of $x_1, x_2, ...x_n$.

When calculating the error in temperature, the error associated with the NI-DAQ is also included. The value of error in the DAQ measuerment, $e_{DAQ} \approx 0.4°C$, is used based on documentation of temperature measurement uncertainties associated with DAQ readings. These errors, thus, add in quadrature

$$e_T = \sqrt{e_{TC}^2 + e_{DAQ}^2} \tag{D.2}$$

where e_{TC} is the thermocouple measurement error given in Table 4.3, i.e. greater of 0.5°C or 0.4%(from 0°C). The total error for a temperature differential is:

$$e_{\Delta T} = \sqrt{2} e_T \tag{D.3}$$

For the pressure drop, the error is estimated as

$$e_{\Delta P} = \sqrt{2} e_P \tag{D.4}$$

where e_P is the pressure measurement error given in Table 4.3, i.e. 0.86 kPa. For volumetric flow rate measurements, the error is based on the value given in Table 4.3 (i.e. $e_{\dot{V}} = 1.2$ ml/min).

For heat rate into single phase flow, the error associated with the heat into the water is calculated as

$$e_Q = \sqrt{\left(\rho \dot{V} c_p e_{\Delta T}\right)^2 + (\rho \Delta T c_p e_{\dot{V}})^2} \tag{D.5}$$

and the error in the heat flux is calculated as

$$e_{\bar{q}''} = e_Q / A_s \tag{D.6}$$

For two phase experiments the total error associated with heat flux rates through the system are given as

$$e_{\bar{q}''} = \frac{k}{\Delta x}\sqrt{e_{\Delta T}^2 + \left(\frac{\Delta T}{\Delta x} e_{\Delta x}\right)^2} \tag{D.7}$$

Where $e_{\Delta x} = 0.029$ cm is the accuracy of the thermocouple measurement location. For the Nusselt number calculations, the error was calculated from the error associated with finding the heat transfer coefficient as $h = \frac{\bar{q}''}{\Delta T}$:

$$e_{\mathrm{Nu}} = \frac{d_h}{k}\sqrt{\left(\frac{e_{\bar{q}''}}{\Delta T}\right)^2 + \left(\bar{q}''\frac{e_{\Delta T}}{\Delta T^2}\right)^2} \tag{D.8}$$

For any subsequent calculations, the same method of error propagation based on Eq. (D.1) is used.

For data in which the standard deviation of the experimental data was significantly larger than the instrumentation error, the uncertainty in the data was estimated as the standard deviation of the data set acquired.

Appendix E

Derivation of Pressure Drop Mechanisms in Experimental Device

The expected pressure drop in the experimental microchannel device is found from a summation of the analytical model within the microchannel with additional “minor” losses at the inlet and exit discussed here.

The first component is the pressure drop associated with the analytical solution, which incorporates dynamic pressure loss and friction losses in the microchannel:

$$\Delta P_{tot,MC} = \rho \int_{r_i}^{r_o} \left[\frac{6}{5} \left(-\bar{v}_r \frac{\partial \bar{v}_r}{\partial r} + \frac{\bar{v}_\theta^2}{r} \right) + \frac{12 \bar{v}_r \nu}{b^2} \right] dr \tag{E.1}$$

It is assumed that all of the energy contained in the tangential flow is lost at the exit (with no pressure recovery).

The pressure drop associated with inlet contraction and outlet expansion regions in the device are estimated using the theory for an ideal sudden contraction and expansion. For an ideal sudden expansion (from White [72]), the pressure drop from the energy lost in the expansion at the exit of the channel flow (i.e. at r_i) is:

$$\Delta P_{SE,loss} = \frac{\rho \bar{v}_{r,i}^2}{2} \left(1 - \frac{2b}{r_i} \right)^2 \tag{E.2}$$

The dynamic pressure gain in a sudden expansion, assuming slug flow at the outlet and parabolic flow in the channel is:

$$\Delta P_{SE,dyn} = \frac{\rho \bar{v}_{r,i}^2}{2} \left(\left(\frac{2b}{r_i} \right)^2 - \frac{6}{5} \right) \tag{E.3}$$

Thus, the total pressure drop in the expansion is:

$$\begin{aligned} \Delta P_{SE} &= \Delta P_{SE,loss} + \Delta P_{SE,dyn} && \text{(E.4)} \\ &= \rho \bar{v}_{r,i}^2 \left(\left(\frac{2b}{r_i} \right) \left(1 - \frac{2b}{r_i} \right) - 1/10 \right) && \text{(E.5)} \end{aligned}$$

For an ideal sudden contraction (from White [72]), the pressure drop associated with the energy lost in the contraction at the inlet of the microchannel (at r_o) is:

$$\Delta P_{SC,loss} = 0.42\frac{\rho\bar{v}_{r,o}^2}{2}\left(1 - \frac{b}{D}\right) \tag{E.6}$$

Where D is the hydraulic diameter of the inlet feeder channel. The dynamic pressure loss in a sudden contraction, assuming slug flow at either side:

$$\Delta P_{SC,dyn} = \frac{\rho\bar{v}_{r,o}^2}{2}\left(1 - \left(\frac{b}{D}\right)^2\right) \tag{E.7}$$

Thus, the total pressure drop in the contraction is:

$$\Delta P_{SC} = \Delta P_{SC,loss} + \Delta P_{SC,dyn} \tag{E.8}$$

$$= \rho\bar{v}_{r,o}^2\left(1.42 - \left(\frac{b}{D}\right)^2 - 0.42\left(\frac{b}{D}\right)\right) \tag{E.9}$$

The pressure drop due to friction in the exit is estimated using:

$$\Delta P_{e,f} = \frac{f_e\rho\nu U_e\Delta x}{2r_i^2} \tag{E.10}$$

Where U_e is the mean velocity through the outlet and Δx is the total length of the outlet to the pressure sensor. The friction factor here is a value for a laminar entry region adapted from Shah and London [63].

The pressure drop due to dynamic pressure gains and friction losses in the inlet region is found using an averaged friction loss in the inlet feeder channel measured from the inlet pressure port which is about 1/4 of the distance away from the inlet feeder channel resulting in about 3/8 of the total estimated pressure drop in the channel:

$$\Delta P_{inlet} = \frac{3}{8}\left(\Delta P_{in,f} + \Delta P_{in,dyn}\right) \tag{E.11}$$

The dynamic pressure loss in the entry channel is:

$$\Delta P_{in,dyn} = \frac{\rho U_{in}^2}{2} \tag{E.12}$$

where U_in is the velocity of the flow in the inlet feeder channel region.

The pressure drop due to friction in the inlet is estimated using:

$$\Delta P_{f,i} = \frac{2f_o\rho\nu U_i\Delta s}{D^2} \tag{E.13}$$

Where f_o is a piecewise friction factor for flow in a square channel including the regions of developing and fully developed flow in the system and Δs is the associated path lengths with each of these regions. Friction factors are found from correlations and data for flow from Shah and London [63] and Kays and Crawford [73].

Thus, the total expected pressure drop in the channel is:

$$\Delta P_{tot} = \Delta P_{tot,MC} + \Delta P_{SE} + \Delta P_{SC} + \Delta P_{e,f} + \Delta P_{inlet} \tag{E.14}$$

Appendix F

Data for All Boiling Tests

F.1 Boiling Curves

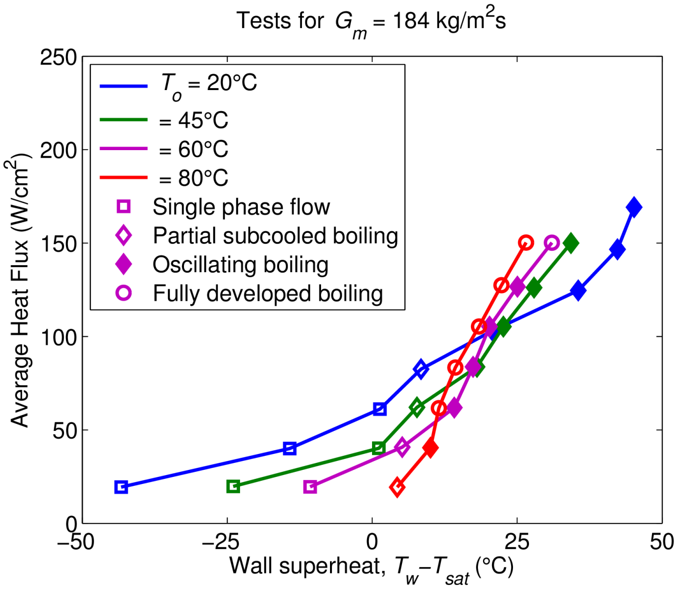

Figure F.1: Boiling curve at a mean mass flux $G_m = 184$ kg/m^{2}s for four different subcooling levels

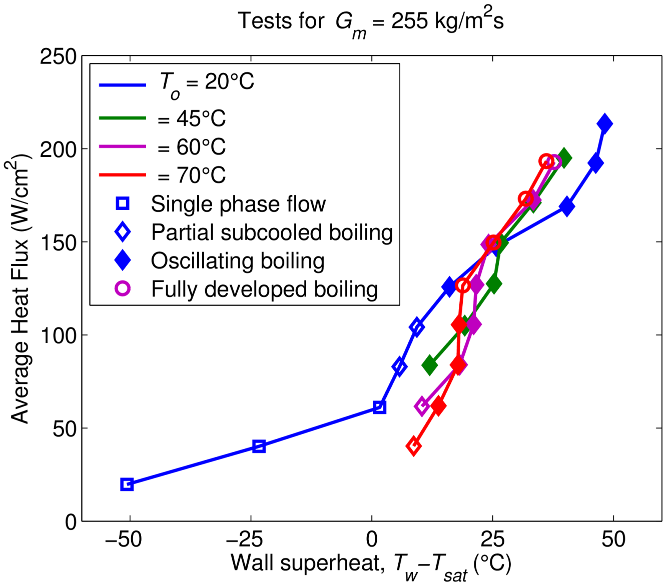

Figure F.2: Boiling curve at a a mean mass flux G = 255 kg/m^{2}s for four different subcooling levels

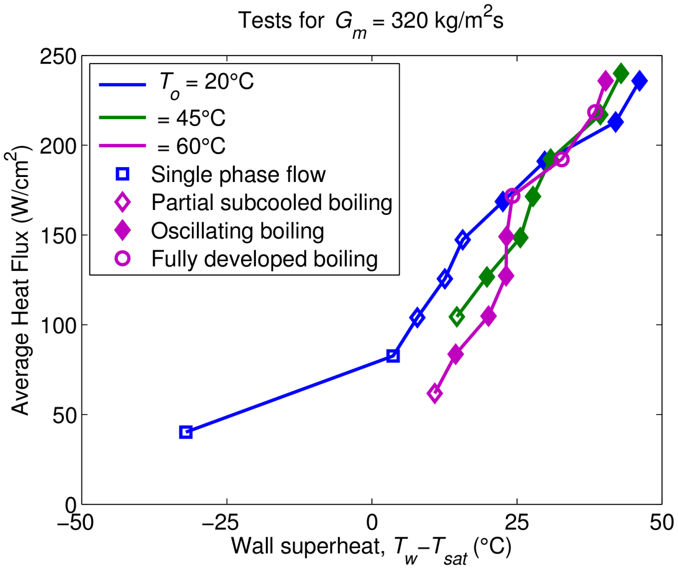

Figure F.3: Boiling curve at a mean mass flux $G_m = 320$ kg/m^{2}s for three different subcooling levels

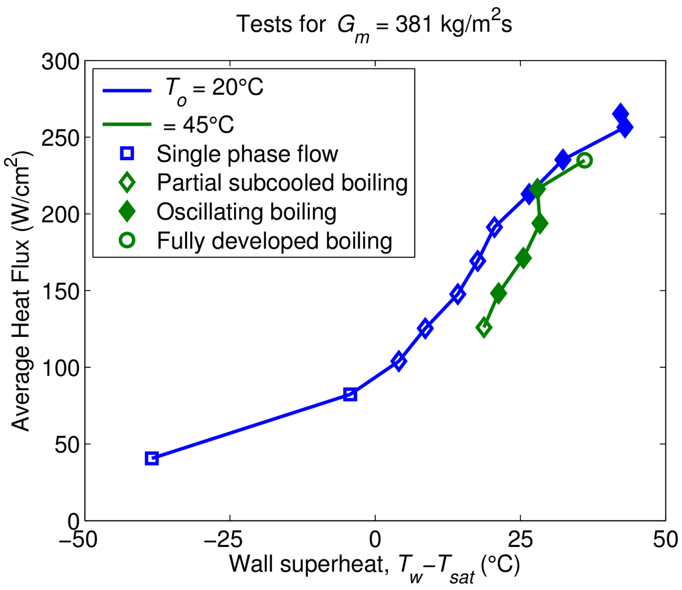

Figure F.4: Boiling curve at a mean mass flux $G_m = 381$ kg/m^{2}s for two different subcooling levels

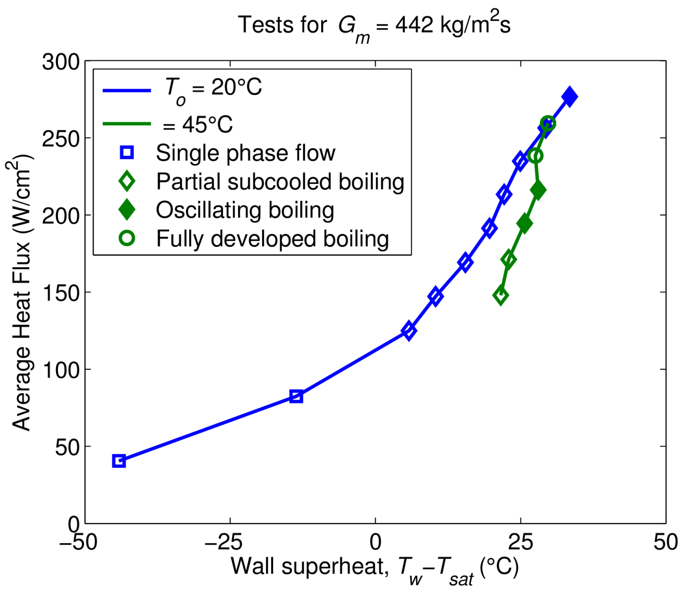

Figure F.5: Boiling curve at a mean mass flux $G_m = 442$ kg/m^{2}s for two different subcooling levels

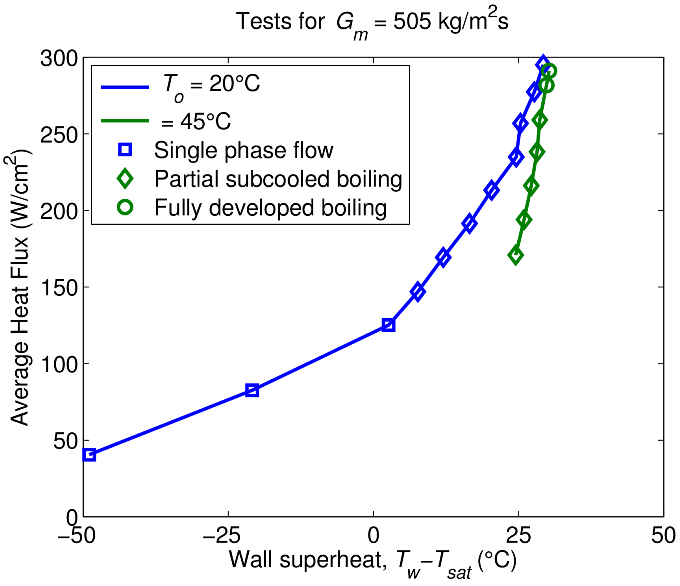

Figure F.6: Boiling curve at a mean mass flux $G_m = 505$ kg/m^{2}s for two different subcooling levels

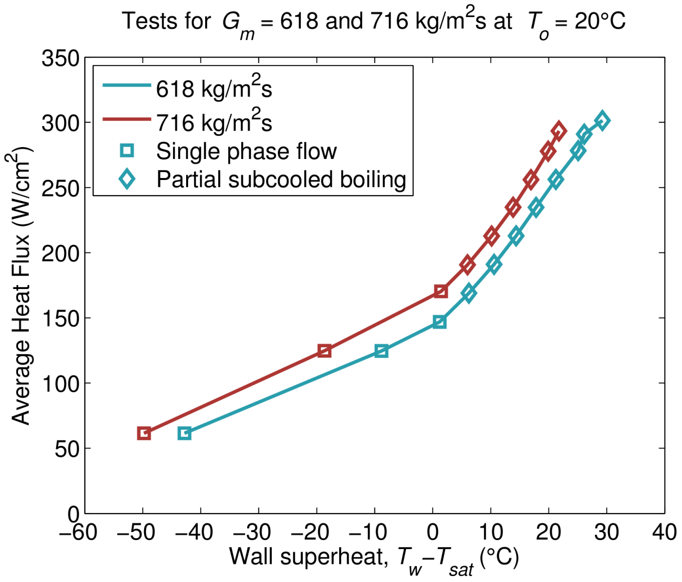

Figure F.7: Boiling curve at mean mass fluxes $G_m = 618$ and 716 kg/m^{2}s

F.2 Heat Transfer Coefficients

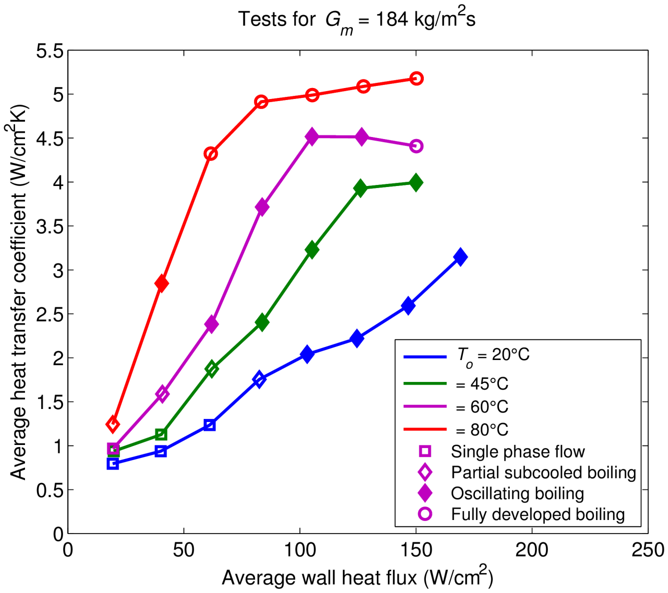

Figure F.8: Heat transfer coefficients for a mean mass flux $G_m = 184$ kg/m^{2}s for four different subcooling levels

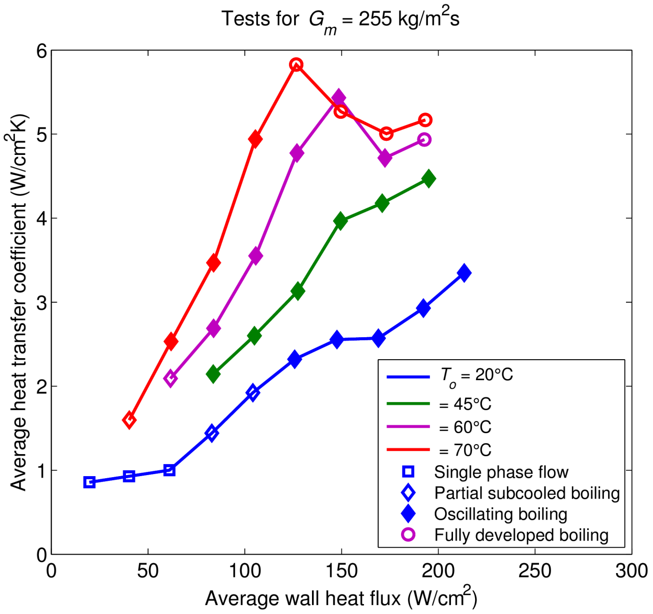

Figure F.9: Heat transfer coefficients for a mean mass flux $G_m = 255$ kg/m^{2}s for four different subcooling levels

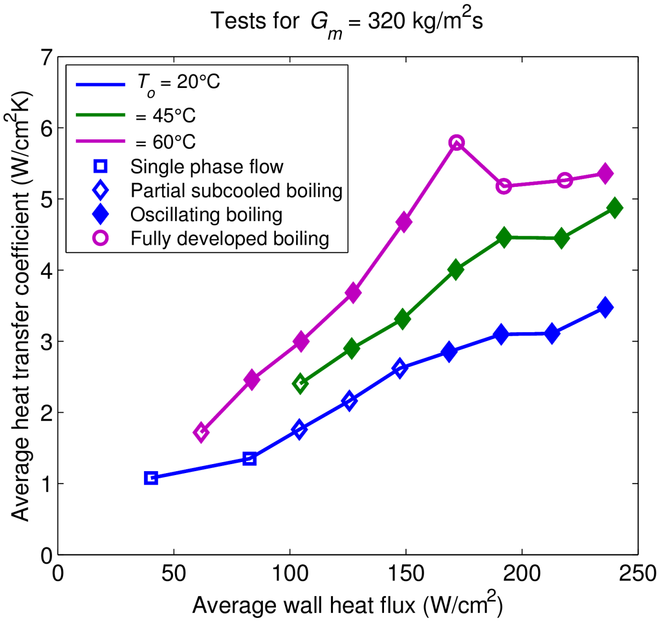

Figure F.10: Heat transfer coefficients for a mean mass flux $G_m = 320$ kg/m^{2}s for three different subcooling levels

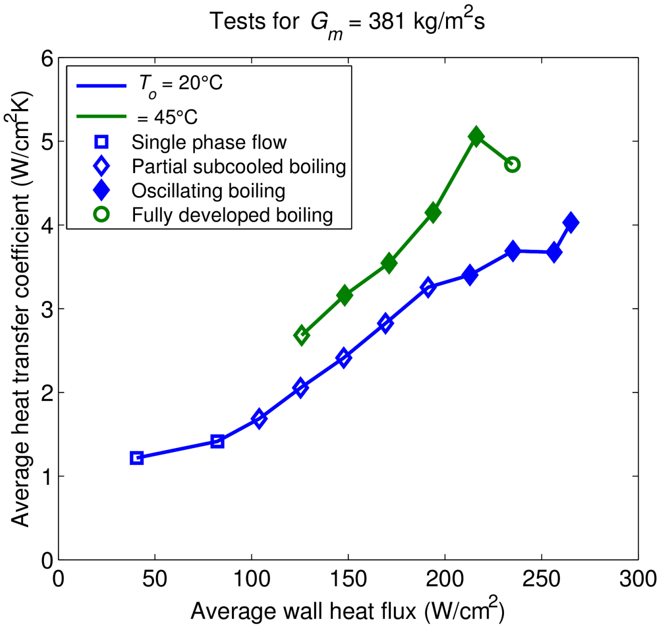

Figure F.11: Heat transfer coefficients for a mean mass flux $G_m = 381$ kg/m^{2}s for two different subcooling levels

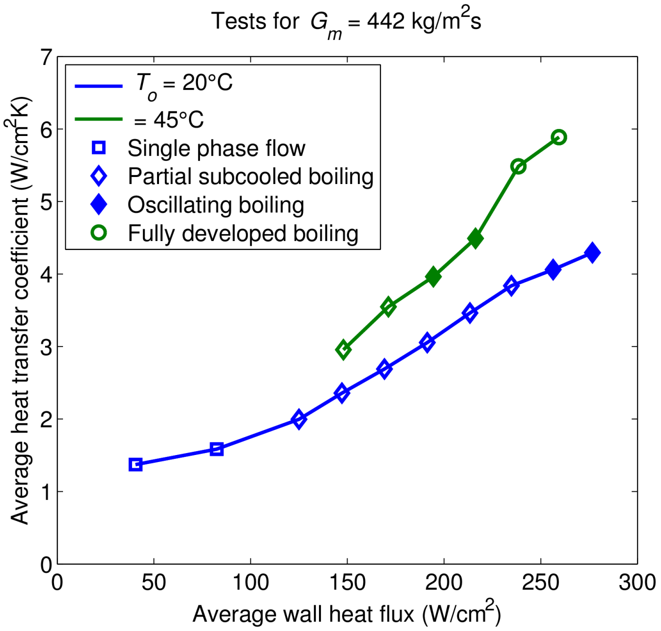

Figure F.12: Heat transfer coefficients for a mean mass flux $G_m = 442$ kg/m^{2}s for two different subcooling levels

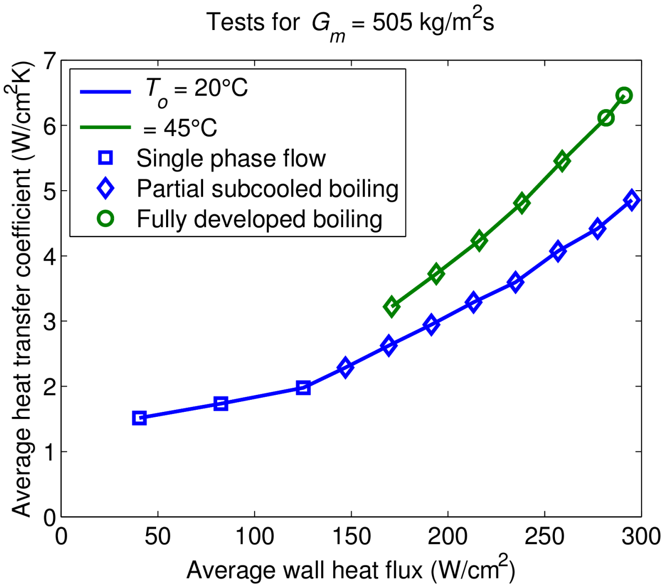

Figure F.13: Heat transfer coefficients for a mean mass flux $G_m = 505$ kg/m^{2}s for two different subcooling levels

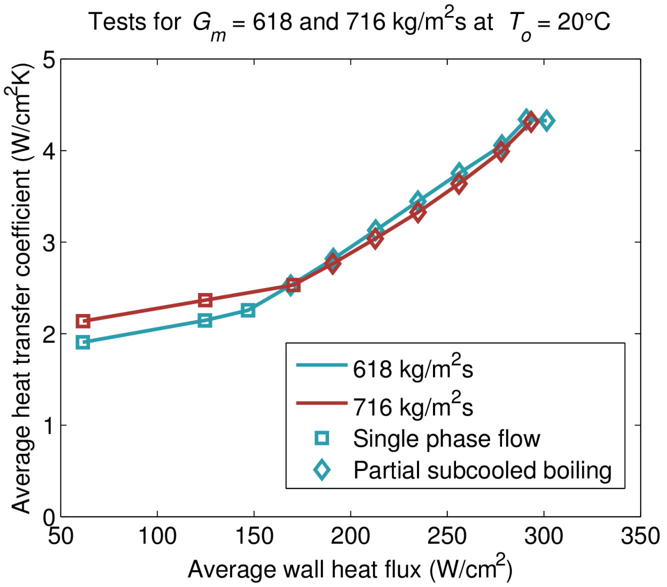

Figure F.14: Heat transfer coefficients for mean mass fluxes $G_m = 618$ and 716 kg/m^{2}s

F.3 Pressure Drop

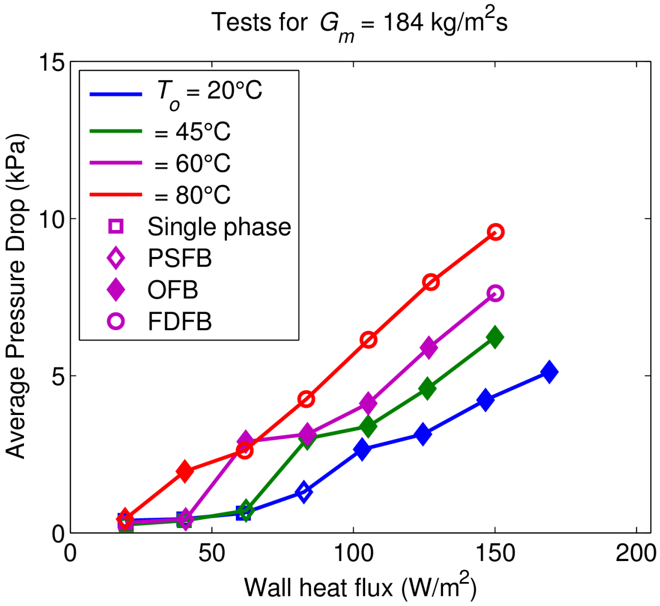

Figure F.15: Average pressure drop across the channel for a mean mass flux $G_m = 184$ kg/m^{2}s for four different subcooling levels

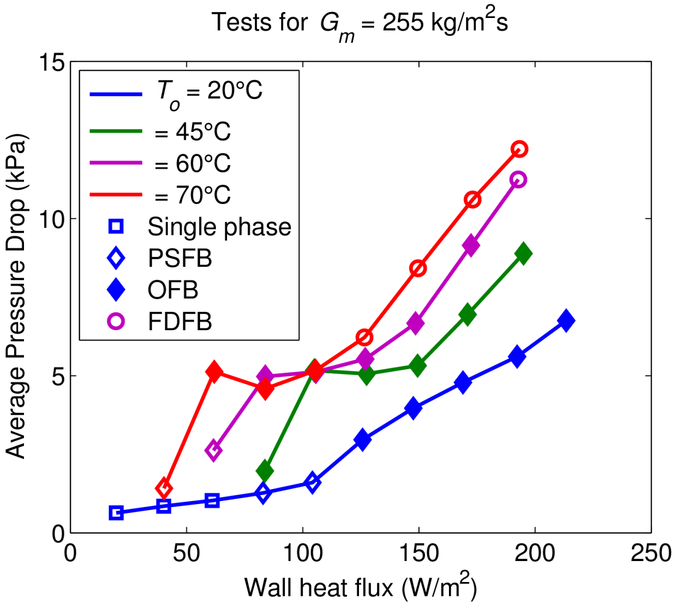

Figure F.16: Average pressure drop across the channel for a mean mass flux $G_m = 255$ kg/m^{2}s for four different subcooling levels

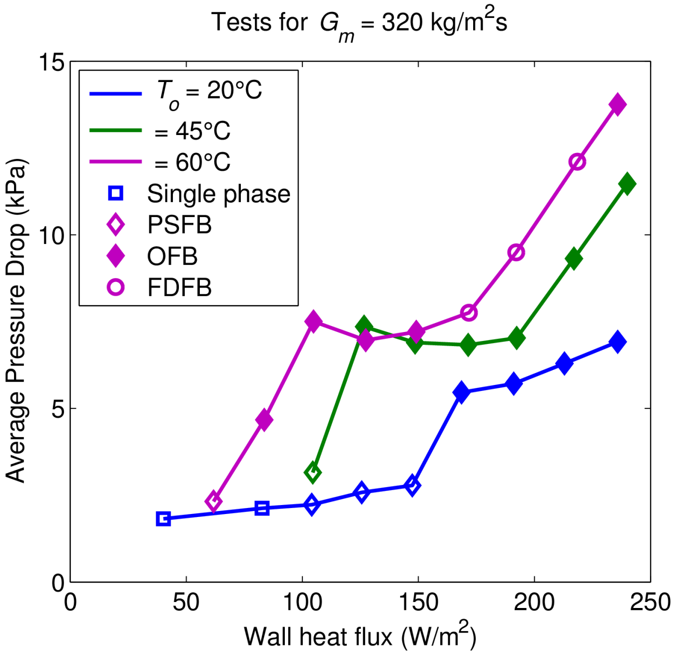

Figure F.17: Average pressure drop across the channel for a mean mass flux $G_m = 320$ kg/m^{2}s for three different subcooling levels

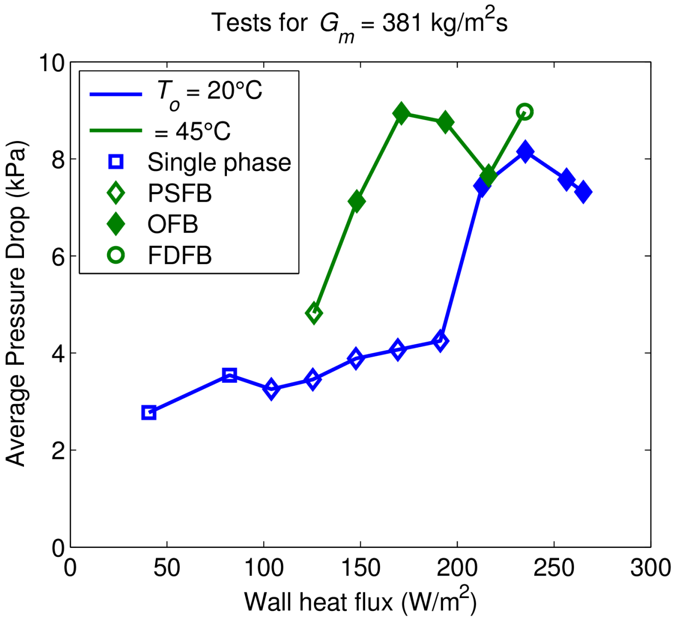

Figure F.18: Average pressure drop across the channel for a mean mass flux G_m = 381 kg/m^{2}s for two different subcooling levels

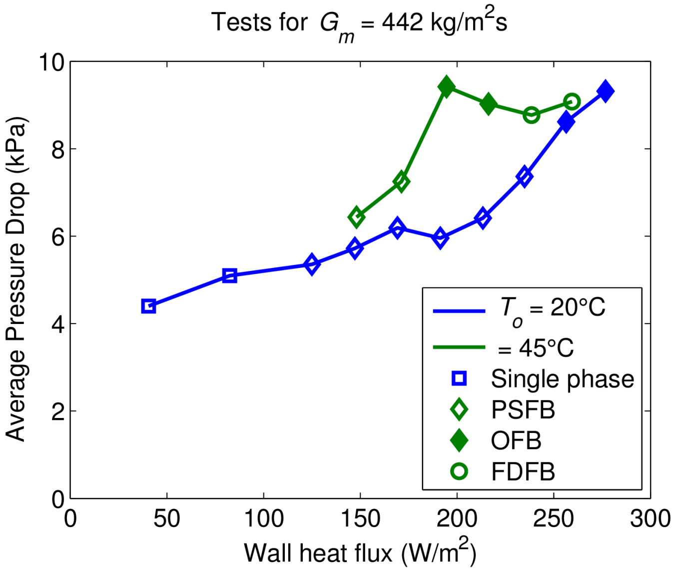

Figure F.19: Average pressure drop across the channel for a mean mass flux G_m = 442 kg/m^{2}s for two different subcooling levels

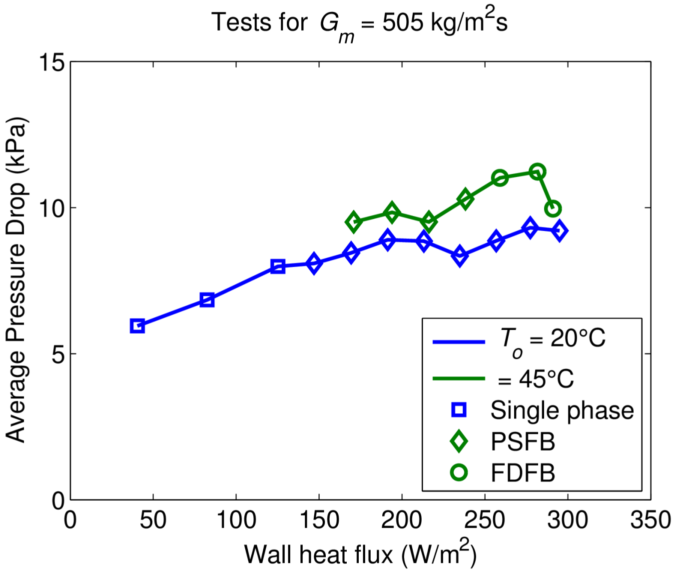

Figure F.20: Average pressure drop across the channel for a mean mass flux G_m = 505 kg/m^{2}s for two different subcooling levels

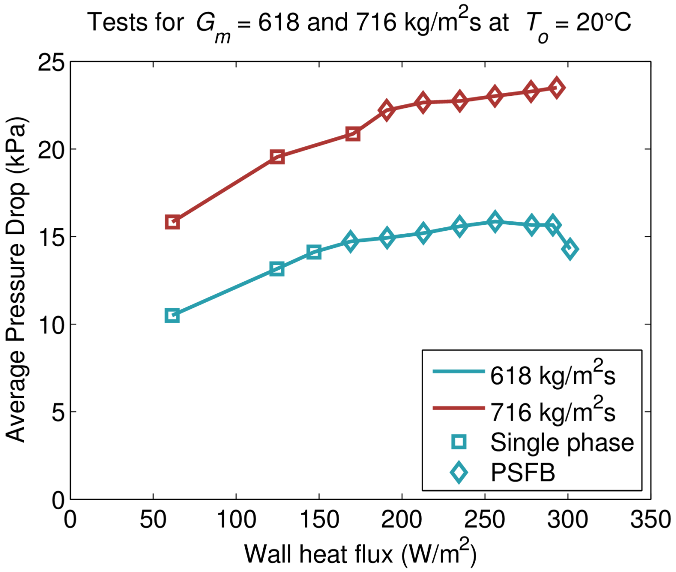

Figure F.21: Average pressure drop across the channel for mean mass fluxes G_m = 618 and 716 kg/m^{2}s